Son Of X-Shooter

SOXS

Optical Design

	NAME	SIGNATURE	DATE
PREPARED	M. Munari (INAF OACT) R. Zanmar Sanchez (INAF OACT)A. Brucalassi (MAS, Millennium Institute of Astrophysics & ESO, European Southern Observatory) J. A. Araiza-Durán (MAS, Millennium Institute of Astrophysics) S.Ben-Ami (Harvard-Smithsonian Center for Astrophysics) A.Rubin (Weizmann Institute for Science) M.Rappaport (Weizmann Institute for Science) O.Diner (Weizmann Institute for Science) O. Hershko (Weizmann Institute for Science) A.Gal-Yam (Weizmann Institute for Science) H. Kuncarayakti (Finnish Centre for Astronomy with ESO (FINCA) & University of Turku) J. Achrén (Incident Angle Oy) T. Kumar (University of Turku)		27/04/18
APPROVED	P. Schipani		27/04/18
RELEASED	S. Campana		27/04/18

CHANGE RECORD

ISSUE	DATE	SECTION/PARAGRAPH AFFECTED	REASON/INITIATION DOCUMENTS/REMARKS
1.0	2017/06/30	All	First Issue for PDR
1.1	2017/10/26	All	Post PDR Issue
1.2	2017/04/27	All	OFDR Issue

TABLE OF CONTENTS

1 PURPOSE AND SCOPE OF THE DOCUMENT 6

1.1 ABBREVIATIONS AND ACRONYMS 6

2 LIST OF APPLICABLE AND REFERENCE DOCUMENTS 7

2.1 APPLICABLE DOCUMENTS 7
2.2 REFERENCE DOCUMENTS 7

3 INTRODUCTION 9

4 COMMON PATH 10

4.1 INTRO 10
4.2 CP UV-VIS ARM 10
4.2.1 Nominal design 10
4.2.2 1st order parameters 11
4.2.3 Optical prescriptions 11
4.2.4 Footprints 14
4.2.5 Image quality 15
4.2.6 ADC 18
4.2.7 Sensitivity analysis 21
4.2.8 Tolerance analysis 22
4.2.9 CP UV-VIS Ghosts 23
4.3 CP NIR ARM 24
4.3.1 Nominal design 25
4.3.2 1st order parameters 25
4.3.3 Optical prescription 25
4.3.4 Footprints 26
4.3.5 Image quality 28
4.3.6 Sensitivity analysis 29
4.3.7 Tolerance analysis 30
4.3.8 CP NIR Ghosts 31
4.4 CP THERMAL BEHAVIOR 32
4.4.1 Slits Position 32
4.4.2 Best focus position 33
4.4.3 Image displacement on the slit 35
4.5 TIP-TILT MIRRORS 36

5 UV-VIS SPECTROGRAPH 37

5.1 OVERALL DESCRIPTION 37
5.2 OPTICAL LAYOUT 37
5.2.1 First order parameters 38
5.2.2 Optical prescription 38
5.2.2.1 Collimator 38
5.2.2.2 Feed 38
5.2.2.3 Gratings and Resolution 38
5.2.2.4 Camera 39
5.2.3 Detector system 49
5.3 OPTICAL QUALITY AND PERFORMANCES 50
5.3.1 Spectral Format and Overlap 52
5.4 THROUGHPUT 53
5.5 SENSITIVITY AND TOLERANCE ANALYSIS 56
5.5.1 Manufacturing and alignment tolerance analysis 56
5.5.2 Feed sensitivity and tolerance analysis 58

5.5.3 Thermal analysis *60*
5.5.4 Ghost analysis *60*
5.5.4.1 Spectral leakage and 2nd order diffraction 62

6 NIR SPECTROGRAPH 63

6.1 Overall Description 63
6.1.1 Optical layout and first orders parameters *63*
6.1.2 Index of refraction *64*
6.1.3 Optical prescriptions *64*
6.1.3.1 Folding Mirror (NIR-FM) 64
6.1.3.2 Collimator (NIR-CM and NIR-CL) 65
6.1.3.3 Prisms (NIR-P1, NIR-P2, NIR-P3) 67
6.1.3.4 Grating (NIR-G) 68
6.1.3.5 Spherical Fold Mirror (NIR-SM) 68
6.1.3.6 Camera 69
6.1.3.7 Complete optical data 73
6.1.4 Detector System *75*
6.2 Performances 76
6.2.1 Orders Data *76*
6.2.2 Spectral Format and inter-orders gap *77*
6.2.3 Scale and slit width *78*
6.2.4 Image quality and Spot Diagrams *79*
6.2.5 Energy concentration and Enslitted energy *82*
6.2.6 Resolution *83*
6.2.7 Throughput *83*
6.3 Sensitivity and Tolerance Analysis 86
6.4 Temperature behaviour 88
6.4.1 TCEs and Index of refraction *88*
6.4.2 From Twork to 20°C *89*
6.4.3 Stability at 150K *89*
6.5 Ghosts and Straylight 90
6.5.1 Camera Ghosts *91*
6.5.2 Single bounce *99*
6.5.3 Prism and Collimator Lens Ghosts *101*
6.5.4 Baffling *103*

7 ACQUISITION CAMERA 106

7.1 Overall description 106
7.2 Detector System 107
7.3 Optical Design 108
7.3.1 Image Quality *109*
7.4 Footprints 111
7.5 Tolerance analysis 112
7.6 Thermal analysis 113
7.7 Throughput 113
7.8 Sensitivity Prediction 115

8 CALIBRATION UNIT 116

8.1 Overall description 116
8.1.1 CU Optical design *120*
8.1.2 Tolerancing *122*

9 CONCLUSIONS 123

1 Purpose and Scope of the Document

The purpose of this document is to present the optical design of SOXS, split in its subsystems (Common path, UV-VIS and NIR spectrograph, Acquisition Camera and Calibration Box), giving elements characteristics and obtained performances.

1.1 Abbreviations and Acronyms

AC	Acquisition Camera
ADC	Atmospheric Dispersion Corrector
AOI	Angle of Incidence
BFS	Best Fitting Sphere
CA	Clear Aperture
CCD	Charge Coupled Device
CP	Common Path
CU	Calibration Unit
EFL	Effective Focal Length
FEA	Finite Elements Analysis
FSR	Free Spectral Range
MC	Montecarlo
NIR	Near Infra-Red
NTT	New Technology Telescope
OAP	Off-Axis Parabola
RFL	Reflected Focal Length
RMS	Root Mean Square
SDIA	Semi-Diameter
SOXS	Son of X-Shooter
TCE	Thermal Coefficient of Expansion
TE	Transverse Electric
TFP	Telescope Focal Plane
TM	Transverse Magnetic
UV-VIS	Ultra-Violet and Visible
VPH	Volume Phase Hologram

2 List of Applicable and Reference Documents

2.1 Applicable Documents

Ref.	Document title	Document ID
AD1	SOXS requirements matrix	SOXS-SPE-0001

2.2 Reference Documents

Ref.	Document title	Document ID
RD1	SOXS Mechanical Design	SOXS-TRE-0002
RD2	B. Delabre; H. Dekker; S. D'odorico and F. Merkle "Astronomical Spectrograph Design With Collimator Compensation Of Camera Chromatism (4C)", Proc. SPIE 1055, Raman Scattering, Luminescence and Spectroscopic Instrumentation in Technology, 340 (July 5, 1989)	
RD3	D. B. Leviton; B. J. Frey; "Temperature-dependent refractive index of Cleartran® ZnS to cryogenic temperatures", Proc. SPIE 8863, Cryogenic Optical Systems and Instruments, 2013	
RD4	D. B. Leviton; B. J. Frey; T. J. Madison; "Temperature-dependent refractive index of CaF2 and Infrasil 301", Proc. SPIE 6692, Cryogenic Optical Systems and Instruments XII, 669204, 2007	
RD5	D. B. Leviton; K. H. Miller; M. A. Quijada; F. U. Grupp; "Temperature-dependent refractive index measurements of CaF2, Suprasil 3001, and S-FTM16 for the Euclid near-infrared spectrometer and photometers", Proc. SPIE 9578, Current Developments in Lens Design and Optical Engineering XVI, 95780M, 2015	
RD6	Considerations about the thermal filter and the extension up to 2.0µm.	SOXS-TRE-0010
RD7	UV-VIS Detector System Design	SOXS-TRE-0005
RD8	NIR Detector System Design	SOXS-TRE-0006
RD09	Quartz Glass for Optics Data and Properties	https://www.heraeus.com/media/media/hqs/doc_hqs/products_and_solutions_8/optics/Data_and_Properties_Optics_fused_silica_EN.pdf

RD10	Daniel C. Harris, Meghan Baronowski, Ladd Henneman, Leonard V. LaCroix, Clyde Wilson, Shelby C. Kurzius, Bob Burns, Keith Kitagawa, Jozef Gembarovic, Steven M. Goodrich, Christian Staats, John J. Mecholsky, "Thermal, structural, and optical properties of Cleartran® multispectral zinc sulfide," Optical Engineering 47(11), 114001 (1 November 2008). https://doi.org/10.1117/1.3006123	
RD11	Material Properties: 6061-T6 Aluminum (UNS A96061)	https://trc.nist.gov/cryogenics/materials/6061%20Aluminum/6061_T6Aluminum_rev.htm
RD12	Calcium Fluoride CaF2 Physical and Chemical Properties	https://lightmachinery.com/media/1542/h0607_caf2_product_sheet.pdf
RD13	E. Oliva; B. Delabre; A. Tozzi; D. Ferruzzi; D. Lee; I. Parry; P. Rees. “Toward the final optical design MOONS, the Multi-Object Optical and Near infrared Spectrometer for the VLT”, Proc. SPIE 9908, Ground-based and Airborne Instrumentation for Astronomy VI, 2016	
RD14	Bradley E. Schaefer ,Astronomical Computing, Sky & Telescope, May 1998	

3 Introduction

SOXS (Son of X-Shooter) will be a spectrograph (R>3500, with a 1" slit) for the NTT (New Technology Telescope) covering the 350-2000nm band, based on a Common Path structure feeding two different arms.

Initially the design considered the 4C layout as baseline for both arms. Afterward the UV-VIS arm evolved, adopting a novel concept based on the use of custom-made ion-etched gratings and dichroics.

This document aims to report on the optical design of the entire system, organized in five sections describing the following subsystems:

- Common path (CP)
- UV-VIS Spectrograph (UV-VIS)
- NIR spectrograph (NIR)
- Acquisition Camera (AC)
- Calibration Unit (CU)

A functional diagram of the instrument is shown in Figure 1.

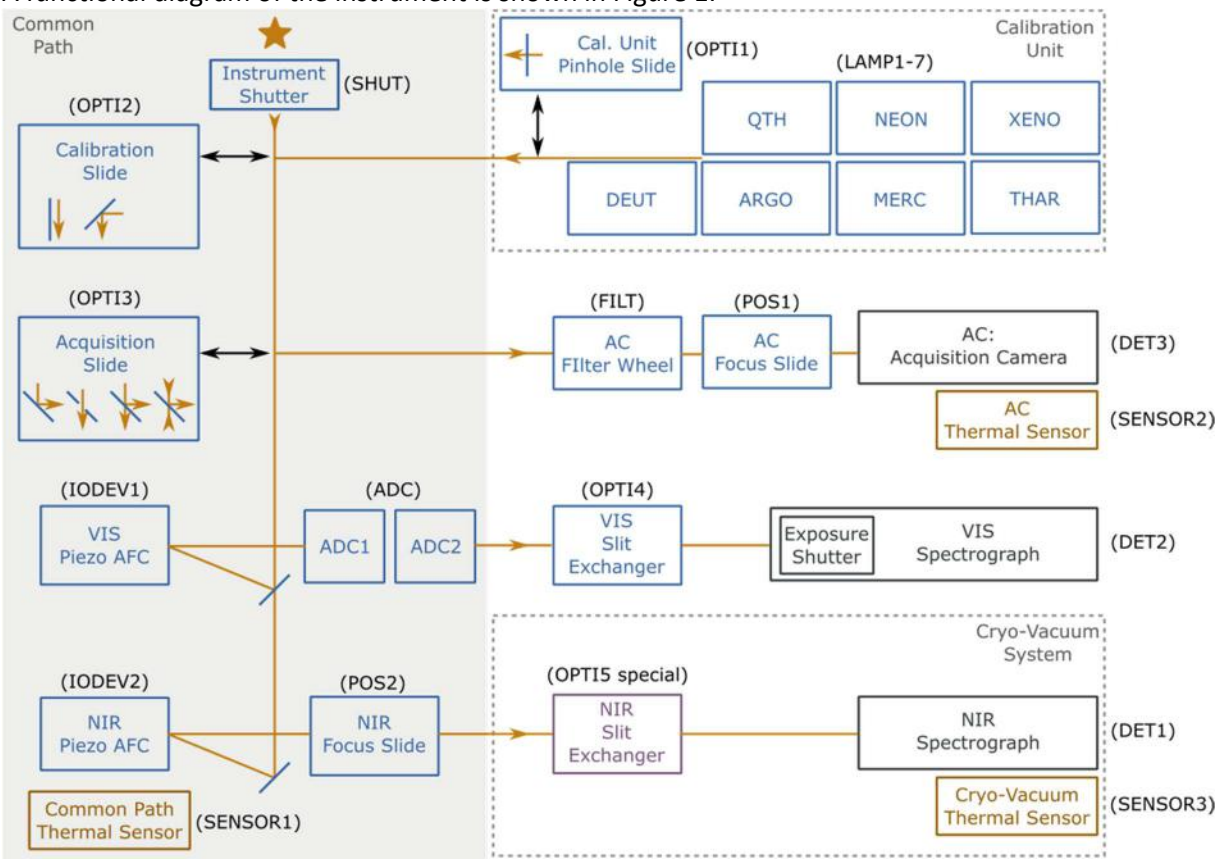

Figure 1: SOXS block diagram.

4 Common Path

4.1 Introduction

The Common Path is the subsystem that relays light from the NTT Focal Plane to the entrance of the two spectrographs (UV-VIS and NIR). In doing that, the CP selects the wavelength range for the spectrographs (using a dichroic) and changes the focal ratio. A sketch of the CP is presented in Figure 2. The overall dimensions are about 650x350mm.

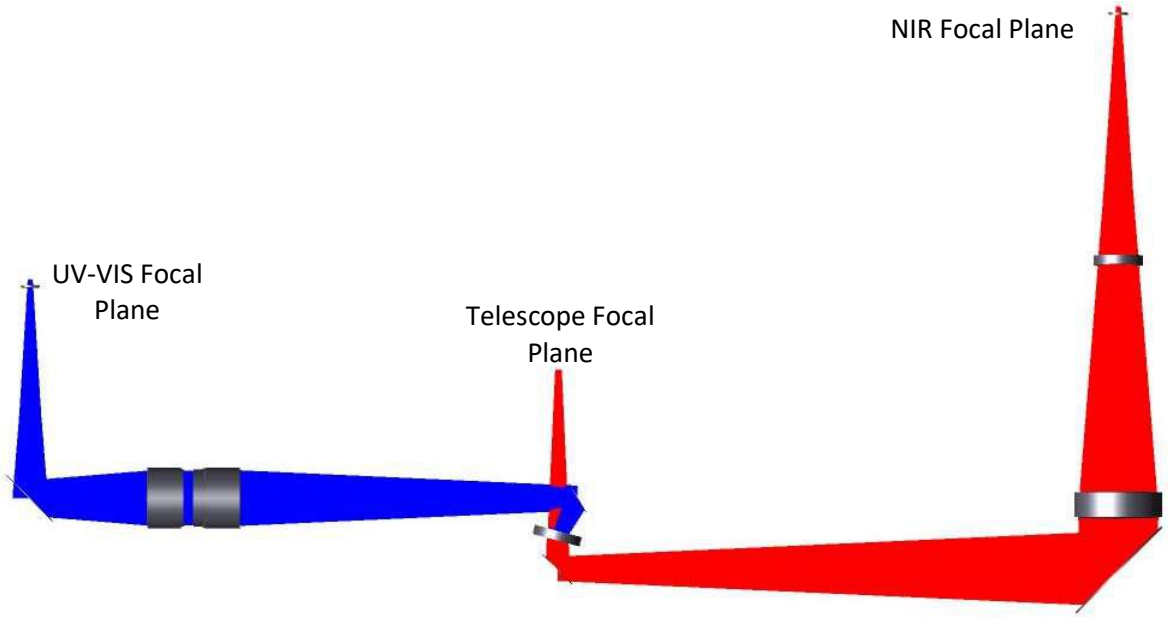

Figure 2: Common Path complete layout. On the left (blue), the UVVIS arm; on the right(red), the NIR arm.

4.2 CP UV-VIS Arm

4.2.1 Nominal design

The CP UV-VIS arm of the common path is depicted in Figure 3. The light coming from the Telescope Focal Plane (TFP) is reflected by the CP-Dichroic (CP_DCR) and a flat folding mirror (CP_FM_VIS) into the ADC assembly (CP_LVIS_01 and CP_LVIS_02). The ADC assembly is actually composed not only of two double prisms (correcting the atmospheric dispersion) but also of two doublets, glued on the prisms (see Figure 4). The two doublets (the first one having an aspherical surface) create a collimated beam for the ADC and transform the telescope F/11 beam into an F/6.5. The aspherical surface has a small deviation of less than 10 µm with respect to the BFS, see Figure 10.
After the ADC, the beam is reflected by the tip/tilt mirror (CP_TT_VIS). Finally, a field lens (CP_LVIS_03) matches the exit pupil on the UV-VIS spectrograph pupil.
The adopted glasses assure a good transmission (>80%) in the UV-VIS side of the spectrum. For the same reason, the dichroic is used in reflection for this wavelength range, in order to give the largest choice of materials for the substrate.

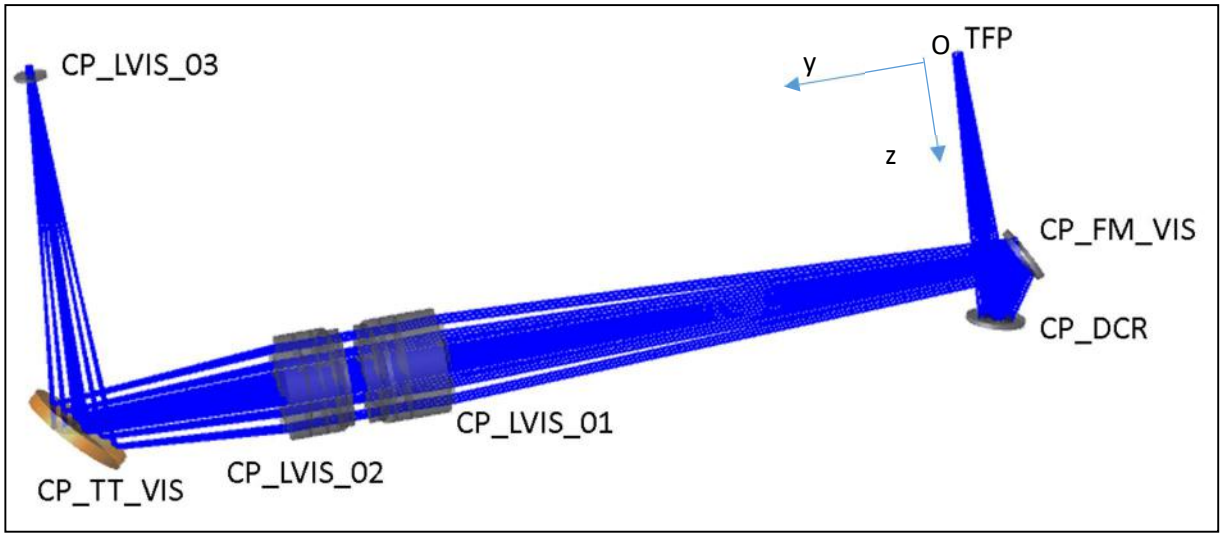

Figure 3: CP UV-VIS arm layout.

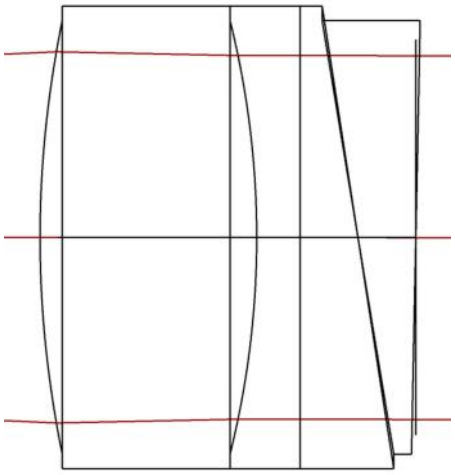

Figure 4: sketch of one of the ADC elements.

4.2.2 1st order parameters

In Table 1 first orders parameters of the CP UV-VIS arm are reported.

Input F/N	F/11
Field of view	12x12 arcsec
Output F/N	F/6.5
Image scale	110 µm / arcsec
Wavelength range	350-880 nm

Table 1: CP UV-VIS 1st order parameters.

4.2.3 Optical prescriptions

The data of the CP UV-VIS optical elements are reported in Table 2.

In Table 3 the coordinates of the elements are presented, where the origin of the coordinates system is the center of the Telescope Focal Plane (TFP), the z axis is parallel and equi-orientated to the beam leaving the TFP, the y axis is oriented toward the UV-VIS slit position (see Figure 3). The angle A is the

rotation of the element around the X axis (angle sign is not considered).

Element	Radius of Curvature (mm)	Thickness (mm)	Material	Free aperture (mm)
Telescope Focal Plane		85.00		
CP_DCR	Flat	-20.00	Mirror	16.00
CP_FM_VIS	Flat	176.29	Mirror	18.00
CP_LVIS_01 S1	72.306 Ev. Asph: 4th:-7.873e-7 6th:+7.110e-12	15.00	CAF2	32.40
CP_LVIS_01 S2	-61.880	3.00	BAL35Y	32.40
CP_LVIS_01 S3	Flat	4.00	BAL15Y	31.60
CP_LVIS_01 S4	Flat tilted -9.369°	4.00	S-FPL51Y	31.60
CP_LVIS_01 S5	Flat tilted 1.146	5.00		31.60
CP_LVIS_02 S1	Flat tilted 1.146	4.00	S-FPL51Y	31.60
CP_LVIS_02 S2	Flat tilted -9.369°	4.00	BAL15Y	31.60
CP_LVIS_02 S3	Flat	3.00	BSM51Y	31.60
CP_LVIS_02 S4	50.121	10.00	S-FPL51Y	32.00
CP_LVIS_02 S5	-63.723	60.00		32.00
CP_TT_VIS	Flat	-110.457	Mirror	32.00
CP_LVIS_03 S1	-31.500	-1.50	SILICA	10.00
CP_LVIS_03 S2		-3.032		10.00
UV-VIS entrance slit				

Table 2: CP UV-VIS optical prescriptions.

Element	X (mm)	Y (mm)	Z (mm)	A (deg)
Telescope Focal Plane	0	0	0	0
CP_DCR	0.00	0.00	85.00	15.00
CP_FM_VIS	0.00	10.00	67.68	60.00
CP_LVIS_01 S1	0.00	-166.29	67.68	90.00
CP_LVIS_01 S2	0.00	-181.29	67.68	90.00
CP_LVIS_01 S3	0.00	-184.29	67.68	90.00
CP_LVIS_01 S4	0.00	-188.29	67.68	90.00
CP_LVIS_01 S5	0.00	-192.29	67.68	90.00
CP_LVIS_02 S1	0.00	-197.29	67.68	90.00
CP_LVIS_02 S2	0.00	-201.29	67.68	90.00
CP_LVIS_02 S3	0.00	-205.29	67.68	90.00
CP_LVIS_02 S4	0.00	-208.29	67.68	90.00
CP_LVIS_02 S5	0.00	-218.29	67.68	90.00
CP_TT_VIS	0.00	-278.29	67.68	135.00
CP_LVIS_03 S1	0.00	-278.29	-42.78	180.00
CP_LVIS_03 S2	0.00	-278.29	-44.28	180.00
UV-VIS entrance slit	0.00	-278.29	-47.31	180.00

Table 3: CP UV-VIS elements vertices coordinates and orientation.

4.2.4 Footprints

In the following images, from Figure 5 to Figure 9, footprints on the CP UV-VIS elements are plotted. Different colors represent different positions in the field, e.g. the center and two extremes on the 1" slit.

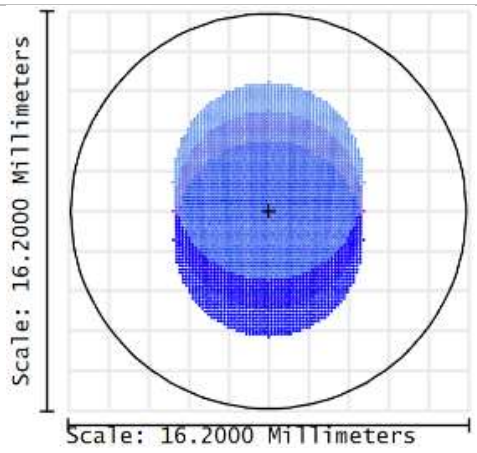

Figure 5: Footprint on CP_DCR first surface.

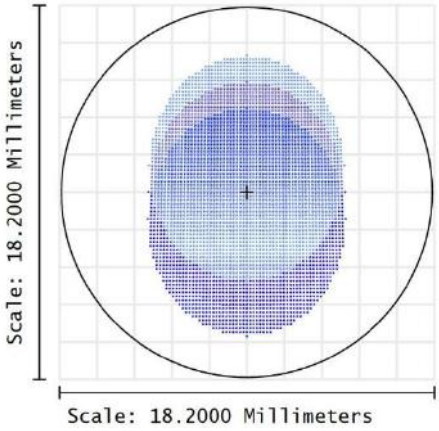

Figure 6: Footprint on CP_FM_VIS.

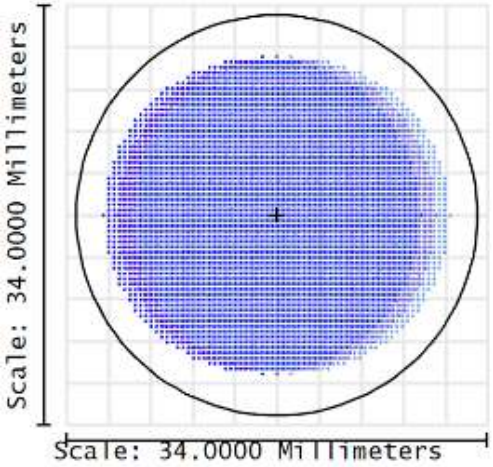

Figure 7: Footprint on CP_LVIS_01.

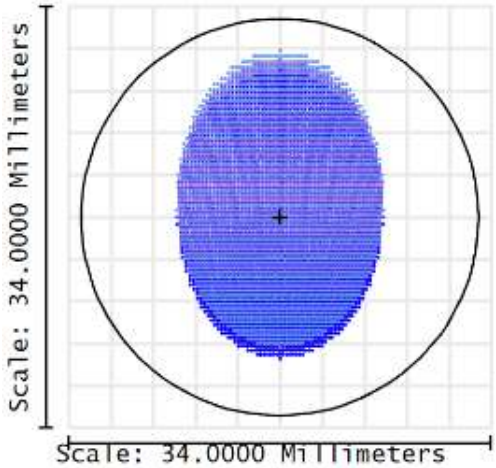

Figure 8: Footprint on CP_TT_VIS.

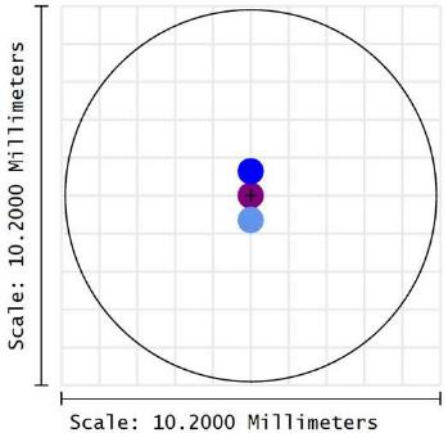

Figure 9: Footprint on CP_LVIS_03.

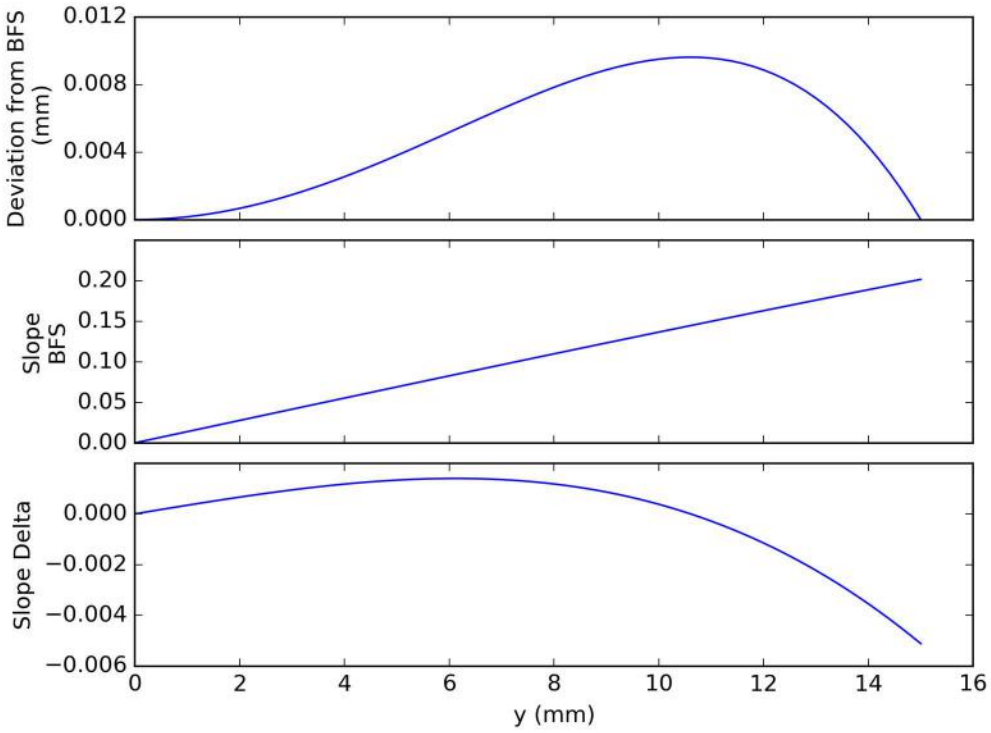

Figure 10: CP_LVIS_01 aspherical surface deviation.

4.2.5 Image quality

Figure 11, Figure 12 and Figure 13 show the spot diagrams for the CP UV-VIS arm at 3 different zenith angles: 0°, 30° and 60° respectively. The spots are enclosed in a square of 55 µm side corresponding to 0.5 arcsec. In each figure, the three spot diagrams are one for each position in the field: center, bottom and top of the 1 arcsec slit. Different colors represent different wavelengths. The included wavelength of 1.1 µm in the spot diagrams is a reference to the NIR arm and it is used to check the residual chromatic error (see Figure 18: ADC Residual chromatic error).

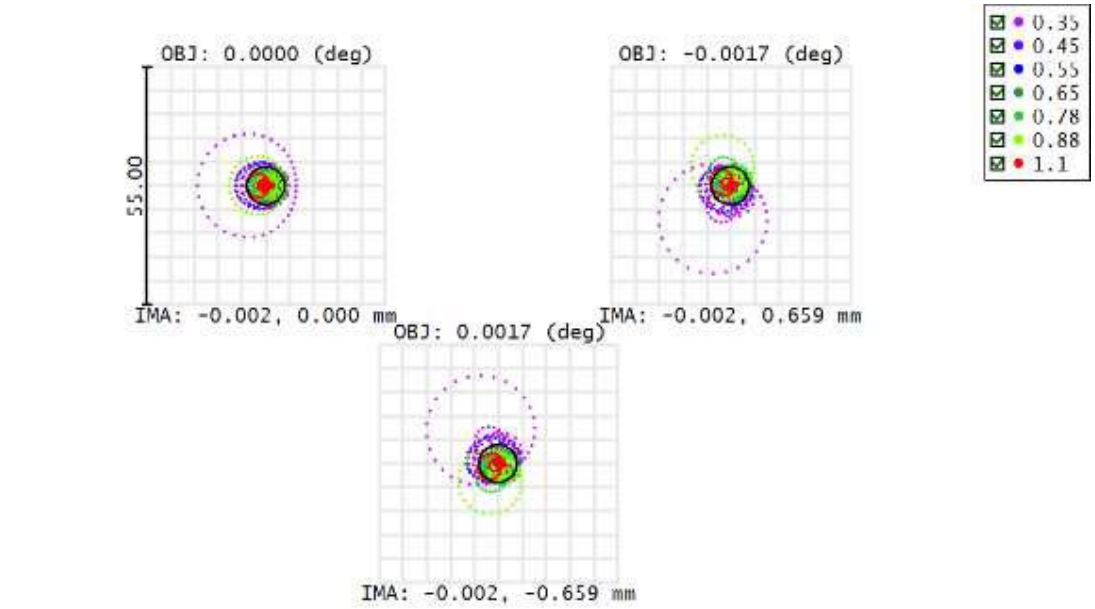

Surface IMA: focal plane

Spot Diagram

19/03/2018
Units are µm. Airy Radius: 4.364 µm. Legend items refer to Wavelengths
Field : 1 2 3
RMS radius : 4.271 4.807 4.807
GEO radius : 15.729 21.317 21.317
Scale bar : 55 Reference : Centroid

Figure 11: CP UV-VIS spot diagrams 0° zenith angle.

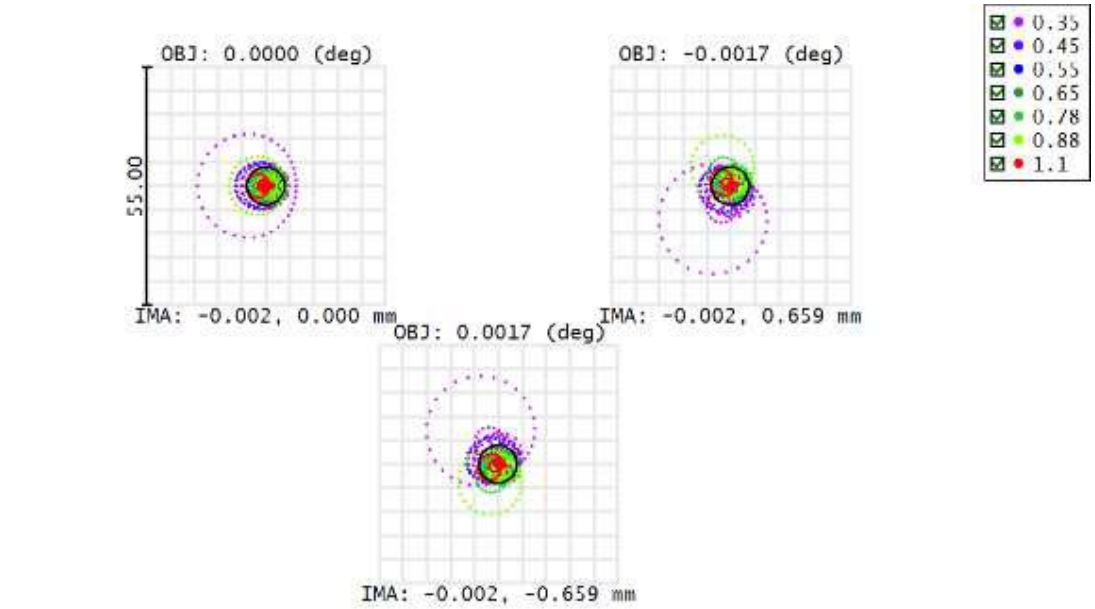

Surface IMA: focal plane

Spot Diagram

19/03/2018
Units are µm. Airy Radius: 4.364 µm. Legend items refer to Wavelengths
Field : 1 2 3
RMS radius : 4.367 5.109 4.676
GEO radius : 15.931 24.280 19.126
Scale bar : 55 Reference : Centroid

Figure 12: CP-VIS spot diagrams 30° zenith angle.

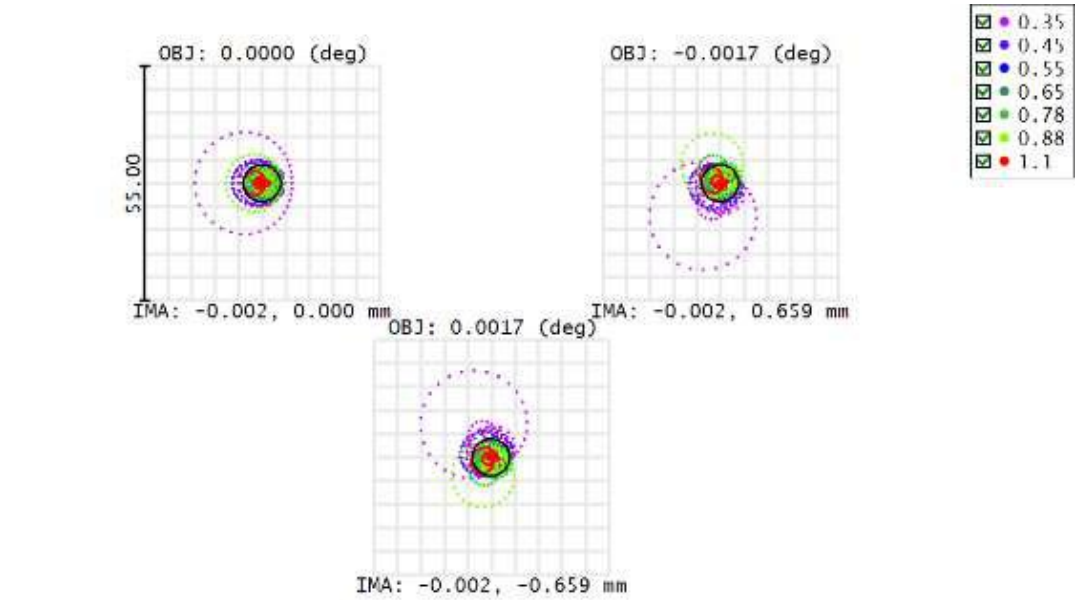

Surface IMA: focal plane

Spot Diagram

19/03/2018
Units are µm. Airy Radius: 4.364 µm. Legend items refer to Wavelengths

Field	1	2	3
RMS radius	5.021	6.111	4.862
GEO radius	21.697	32.454	15.422

Scale bar : 55 Reference : Centroid

Figure 13: CP UV-VIS spot diagrams 60° zenith angle.

In Figure 14 and Figure 15, the encircled energy for the CP UV-VIS arm is plotted, showing that for both zenith angles of 0° and 60°, 80% of the energy is contained in a circle of radius <1/10 of arcsec (11 µm).

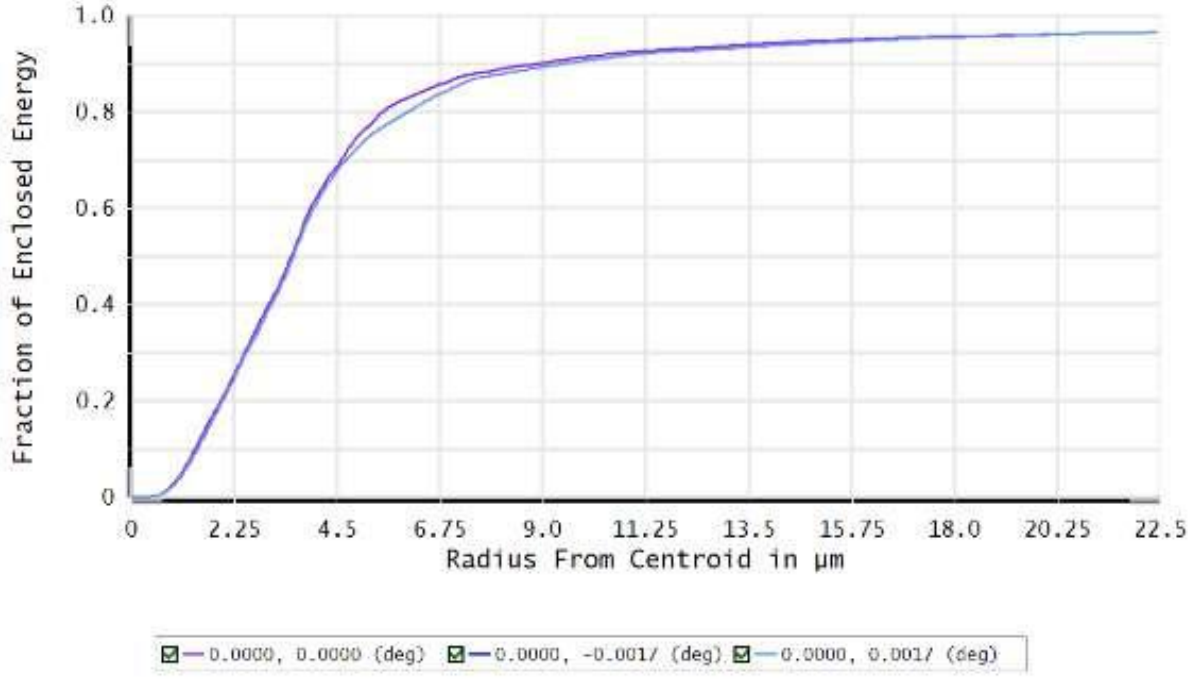

Figure 14: CP UV-VIS Encircled energy for 0° zenith angle.

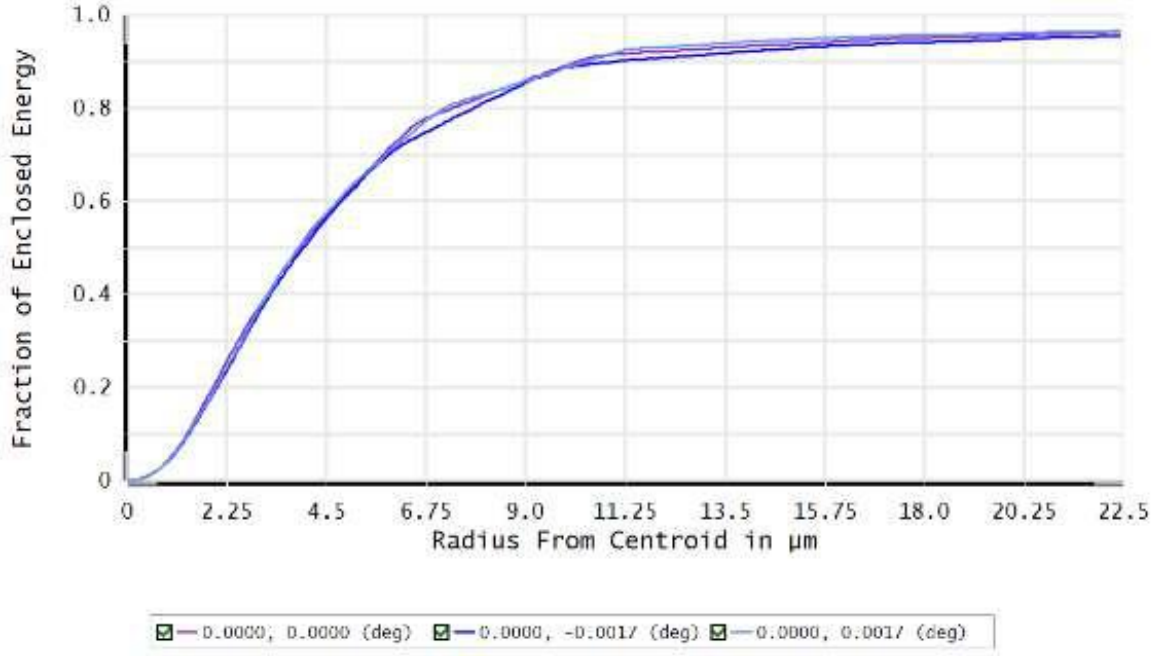

Figure 15: CP-VIS Encircled energy for 60° zenith angle.

4.2.6 ADC

The CP UV-VIS arm hosts an ADC (Atmospheric Dispersion Corrector).

Figure 16 shows that, while in the wavelength range of the NIR the atmospheric dispersion is only ~0.2arcsec at zenith angle Z=30° and ~0.5arcsec at Z=60°, in the UV-VIS the same conditions lead to dispersions of ~1.2 and ~3.6 arcsec (values calculated following Filippenko 1982, using T=10°, P=770mb, H=44%). Therefore the use of an ADC in the UV-VIS was deemed mandatory.

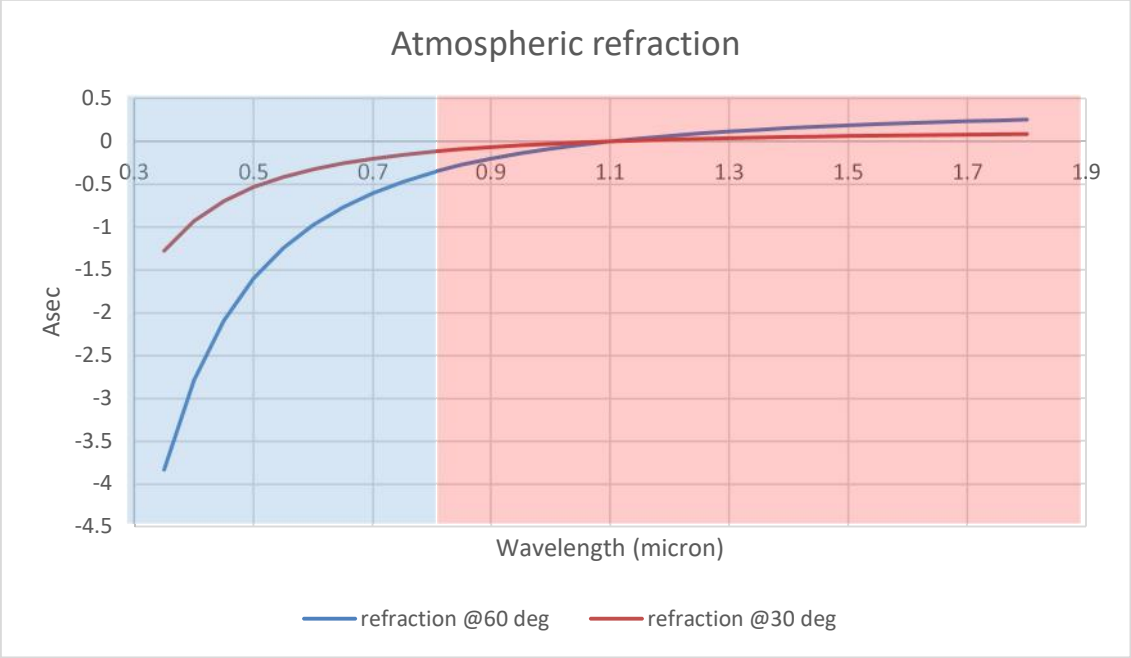

Figure 16: Atmospheric dispersion.

As described in section 4.2.1, the ADC is composed of pair of prisms (each pair composed of two

different glasses) counter-rotating to correct the dispersion.
The first prism rotation angle (and the corresponding counter-rotation of the second prism) depend on the zenith angle and the atmospheric conditions (see Figure 17). The prism rotation angle is modeled with this function:

prism_angle = acos((3.6e-1 -1.2e-3 x T + 4.4e-4 x P) x tan(zenith_angle))

where T is the temperature in Kelvin and P is the pressure in mbar. These models are presented as solid lines in Figure 17.

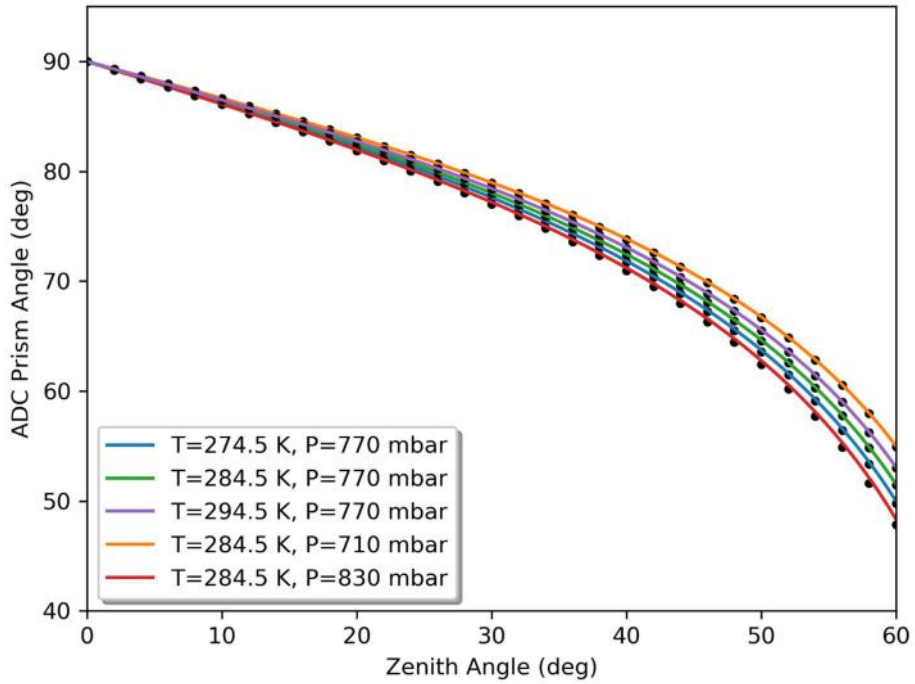

Figure 17: ADC prism angle. The points are prism angles found by optimization in ZEMAX. The solid lines are best fitting models.

To simplify the system and make it compact, the two doublets of the CP UV-VIS are glued directly on the prisms. This also increases the transmissivity of the system, allowing for the elimination of two glass-air interfaces.
Aa residual wavelength spread is present even using the ADC, but as shown in Figure 18 the spread of the monochromatic spots centroids is always smaller than 4 µm(<0.05arcsec), up to a wavelength of 900nm.

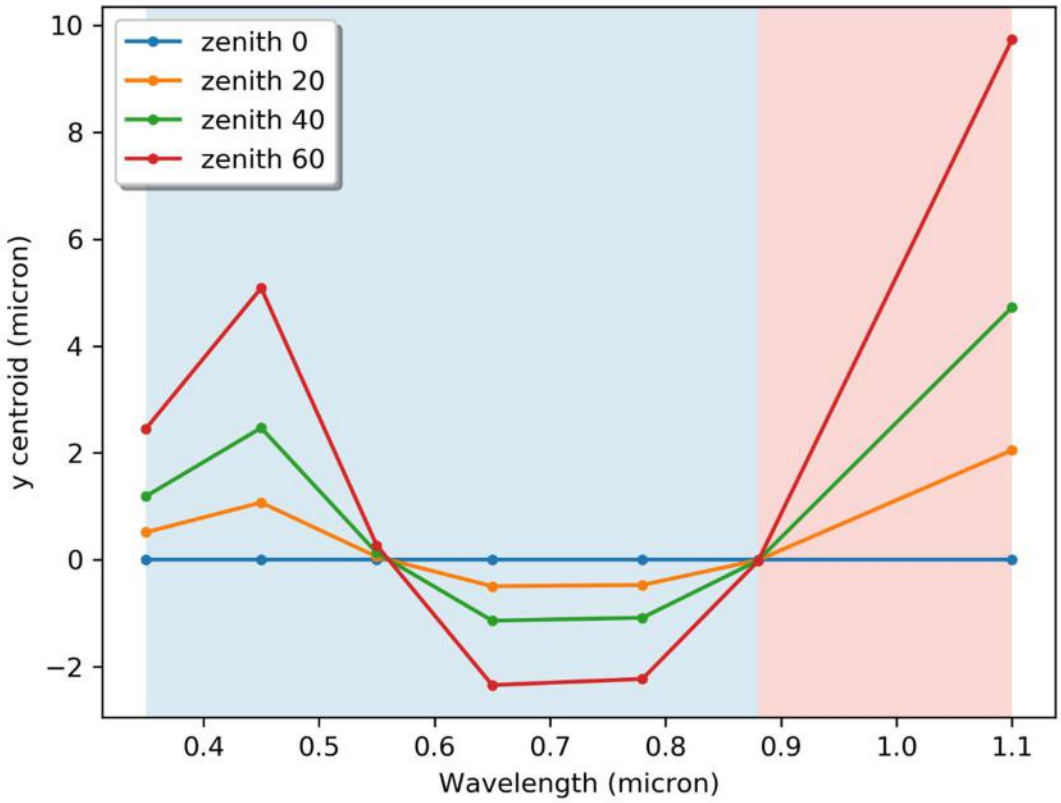

Figure 18: ADC Residual chromatic error.

The offset of the centroid of the spots in the wavelength range of the CP UV-VIS arm with respect to the centroid of the spot at 1100 nm was evaluated in order to check the co-alignment of the two spectrographs. 1100 nm is the design reference wavelength: in the NIR wavelength range, the dispersion range is more or less symmetric around 1100nm. As shown in Figure 19 the two centroids differ always by less than 9 µm(<0.1 arcsec).

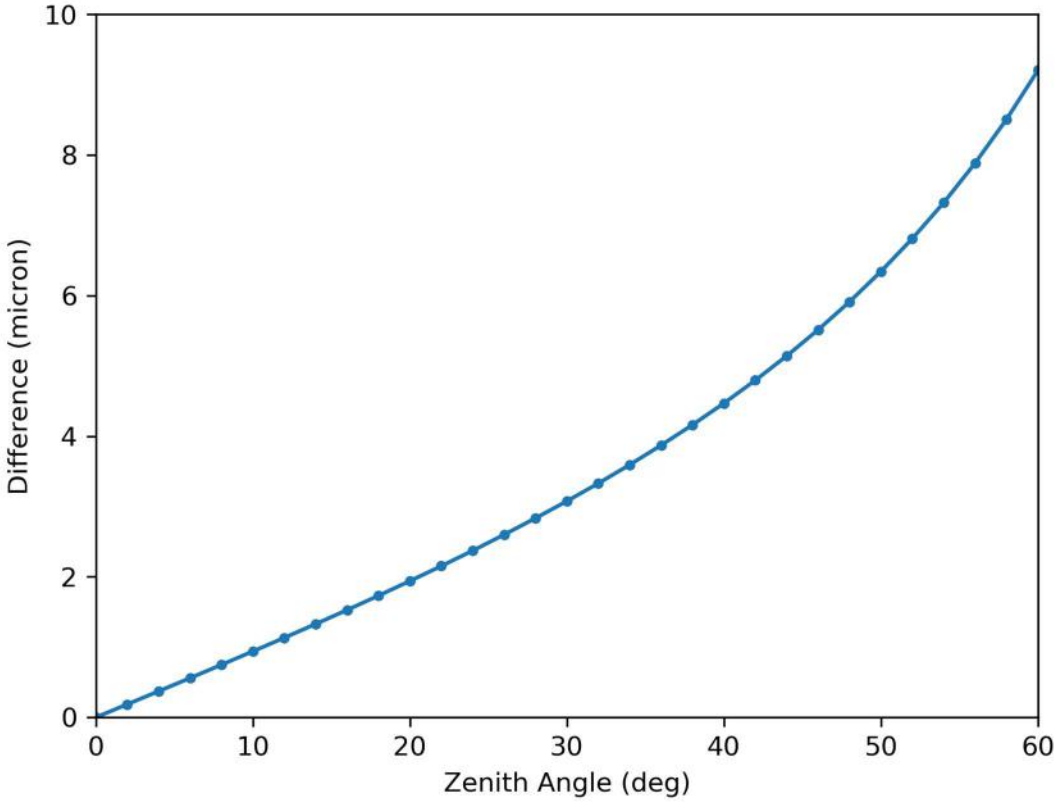

Figure 19: Offset of CP UV-VIS spot centroid w.r.t. 1100nm spot centroid.

4.2.7 Sensitivity analysis

A sensitivity analysis has been performed to evaluate the displacements of the image on the slit plane (dX_i, dY_i, dZ_i), due to displacements (dX_e, dY_e, dZ_e) and tilts (dAX_e, dAY_e, dAZ_e) of single elements of the CP UV-VIS.

The analysis has been done using local system coordinates for each element, i.e. for each element, a right hand coordinate system defined as follows: origin in the vertex of the element, Z axis along the normal to the surface element (and directed from the Telescope Focal Plane to the slit) and Y axis in the CP plane.

Compound elements (e.g. the two ADC elements) are considered as single elements and moved/tilted w.r.t. the first surface of the element. An example of a tilt is depicted in Figure 20.

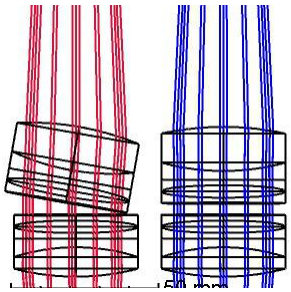

Figure 20: CP UV-VIS ADC1 element, tilted around the X axis passing through the first surface vertex (RED). The BLUE layout is the nominal design.

Results of the analysis are given in Table 4.

	µm/mm			µm/arcmin		
	dXi/dXe	dXi/dYe	dXi/dZe	dXi/dAXe	dXi/dAYe	dXi/dAZe
	dYi/dXe	dYi/dYe	dYi/dZe	dYi/dAXe	dYi/dAYe	dYi/dAZe
	dZi/dXe	dZi/dYe	dZi/dZe	dZi/dAXe	dZi/dAYe	dZi/dAZe
CP_DCR	0	0	0	0	-28	0
	0	0	-306	29	0	0
	0	0	674	0	-1	0
CP_FM_VIS	0	0	0	0	31	0
	0	0	-591	-36	0	0
	0	0	-602	0	1	0
CP_LVIS_01	0	-561	0	-1	0	0
	561	0	0	0	-1	0
	-81	-79	348	0	0	0
CP_LVIS_02	0	-970	0	6	0	0
	970	0	0	0	6	0
	56	62	-871	0	0	0
CP_TT_VIS	0	0	0	0	-44	0
	0	0	-1357	63	0	0
	0	0	1283	0	0	0
CP_LVIS_03	59	0	0	0	0	0
	0	59	0	0	0	0
	3	3	128	0	0	0

Table 4: CP UV-VIS image displacement due to CP UV-VIS elements displacements and Tilts.

4.2.8 Tolerance analysis

A preliminary tolerance analysis was done on the CP UV-VIS subsystem. The analysis adopted errors on positioning of complete elements (mirrors, two ADC elements, dichroic and field lens) and on manufacturing of single elements (thickness, curvature, wedge, surface quality, and glass quality). The spot RMS radius (nominal value: 3.7 µm) was adopted as merit figure, the focus position was the compensator.

Element	Dx[mm]	Dy[mm]	Dz[mm]	Tx deg	Ty deg
Dichroic	0.2	0.2	0.2	0.2	0.2
M1	0.2	0.2	0.2	0.2	0.2
ADC1	0.05	0.05	0.2	0.05	0.05
ADC2	0.05	0.05	0.2	0.05	0.05
M2	0.2	0.2	0.1	0.2	0.2
Field lens	0.2	0.2	0.2	0.2	0.2

Table 5: Elements positioning tolerances.

Elements manufacturing

- Glasses: Index of refraction +/- 1e-3; abbe 0.5% (except field lens, 1%)
- Surfaces quality 0.5 fringe (@633nm)
- Thickness 0.2mm

- Curvature 0.1%. Planarity 3 fringes (1 fringe for CP_TT_VIS).
- Elements surfaces mutual positioning

Element	Tx (deg)	Ty (deg)
CP_LVIS_01 S2	0.03	0.03
CP_LVIS_01 S3	0.1	0.1
CP_LVIS_01 S4	0.1	0.1
CP_LVIS_01 S5	0.03	0.03
CP_LVIS_02 S2	0.1	0.1
CP_LVIS_02 S3	0.1	0.1
CP_LVIS_02 S4	0.03	0.03
CP_LVIS_02 S5	0.03	0.03
CP_LVIS_03 S2	0.1	0.1

Table 6: Elements surfaces positioning errors.

Results of 100 Montecarlo realizations show statistical data in Table 7. MC analysis shows that at 90% of the realizations, RMS spot radius is less than one tenth of 1 arcsec (110 µm). The compensator displacement moved from -1.4 to 1.9 mm.

Percentage	Merit Function (mm)
90%<	0.0084
80%<	0.0078
50%<	0.0070
20%<	0.0061
10%<	0.0058

Table 7: CP UV-VIS 100 MC realizations statistics.

4.2.9 CP UV-VIS Ghosts

Ghosts, due to double parasite reflections on transmissive elements, are present on the slit plane of the CP UV-VIS.

Given the large distances among the elements, the main effects are due to double reflections inside a single element, namely the ADC (CP_LVIS_01 and CP_LVIS_02) and the field lens (CP_LVIS_03).

In Table 8, data of the ghosts with the highest irradiance are reported. The columns are:

- S1 and S2 are the two surfaces involved in the ghost;
- r1 and r2 are the adopted reflectivities (5% for the dichroic, 2% for the AR coating of lenses, 0.5% for the internal surfaces of composite elements);
- Xmax, Xmin, Ymax and Ymin are the max and min coordinates of the extremes of the ghost on the slit focal plane;
- P is the percentage of rays that are able to pass through the system and R the ratio of irradiance wrt the nominal image;
- A, the area of the ghost, calculated as (xmax-xmin) x (ymax-ymin), and rescaled to arcsec^2 with the scale (110 µm/arcsec).
- R, the Ratio is calculated assuming that the nominal image has an area of A_i=1 arcsec squared (i.e. assuming a seeing of 1 arcsec): $R = r1 * r2 * \frac{P}{100} * A_i/A$.

S1	S2	r1	r2	Xmax [mm]	Xmin [mm]	Ymax [mm]	Ymin [mm]	P%	R	A [arcsec^2]
CP_LVIS_02 1	CP_LVIS_01 5	0.02	0.02	0.026	-0.026	0.011	-0.038	100	4.00E-04	2.10E-01
CP_LVIS_02 3	CP_LVIS_01 3	0.005	0.005	0.027	-0.027	0.031	-0.024	100	2.50E-05	2.49E-01
CP_LVIS_03 2	CP_LVIS_03 1	0.02	0.02	0.231	-0.231	0.234	-0.228	100	2.27E-05	1.76E+01
CP_LVIS_03 1	CP_LVIS_01 3	0.02	0.005	0.343	-0.343	0.339	-0.347	100	2.57E-06	3.89E+01
CP_LVIS_03 1	CP_LVIS_02 3	0.02	0.005	0.345	-0.345	0.341	-0.349	100	2.54E-06	3.93E+01
CP_LVIS_02 2	CP_LVIS_01 4	0.005	0.005	0.211	-0.211	0.557	-0.019	91.91	1.14E-06	2.01E+01
CP_LVIS_03 2	CP_LVIS_01 3	0.02	0.005	0.628	-0.628	0.614	-0.643	100	7.66E-07	1.31E+02
CP_LVIS_03 2	CP_LVIS_02 3	0.02	0.005	0.630	-0.630	0.615	-0.645	100	7.62E-07	1.31E+02

Table 8: CP UVVIS Ghost data.

From the area of the ghosts, it appears that some point-like ghosts are present, namely those created by the ADC two prisms facing surfaces, and by the two flat surfaces inside the ADC elements (where the two prisms are glued to the lenses). For these ghosts, the area is << 1arcsec^2; consequently the adopted area of the ghost was 1 arcsec^2, i.e. seeing limited. These ghosts (and the diffuse one due to the field lens internal reflections) are the most intense ones.
All other ghosts, due to inter-elements and intra-element interactions, are much weaker (2 orders of magnitude). Moreover, some of these ghosts, due to the tilted faces of prisms, will only partially enter the slit (e.g. the last in the table).
Even considering all the possible ghosts, and summing up their intensity (disregarding the fact that not all will be superimposed in the same positions) the total ratio is still <4.5e-4.

4.3 CP NIR Arm

CP-NIR arm is similar to the UV-VIS arm (same first order parameters, except the wavelength range). Unlike the UV-VIS, the NIR arm does not include an ADC, since the atmospheric dispersion is less severe than in the UV-VIS range and is considered acceptable (see Figure 16) in the instrument system trade-off. The CP NIR Arm includes a doublet (CP_LIR_01) in order to reduce the telescope F/11 beam to an F/6.5 beam. The doublet has an aspherical surface deviating less than 4 µm with respect to the BFS (see Figure 29), deemed feasible to manufacture. Two flat mirrors (CP_FM_IR and CP_TT_IR) relay the light to the slit. In order to allow the entering of light in the NIR spectrograph Dewar, the CP NIR Arm includes a flat window (CP_W_IR), and to reduce noise in the NIR spectrograph, a cold stop was introduced after the window itself (CP_ST_IR). A field lens (CP_LIR_02), placed near the slit, remaps the telescope pupil on the grating of the spectrograph (as in the UV-VIS arm). The whole CP NIR Arm layout is presented in Figure 21.

4.3.1 Nominal design

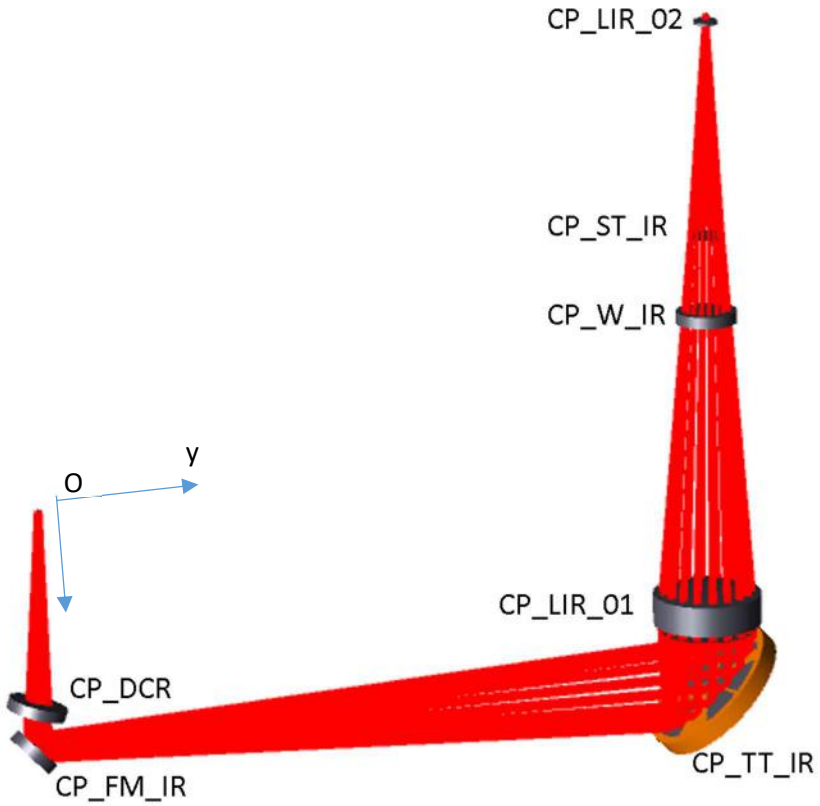

Figure 21: NIR arm CP layout.

4.3.2 1st order parameters

In Table 9 first orders parameters of the CP-NIR arm are reported.

Input F/N	**F/11**
Field of view	12x12 arcsec
Output F/N	F/6.5
Image scale	110 µm / arcsec
Wavelength range	800-2000 nm

Table 9: CP NIR 1st order parameters.

4.3.3 Optical prescription

In Table 10 data of the elements of the CP NIR are reported.
In Table 11 the coordinates of the elements are reported, where the origin of the coordinates system is the center of the TFP, the z axis is parallel to and has the same direction as the beam leaving the TFP, the y axis is oriented toward the NIR slit position (see Figure 21).
The diameter of the stop is slightly oversized, to avoid vignetting problems.

Element	Radius of Curvature (mm)	Thickness (mm)	Material	Free Diameter (mm)
Telescope Focal Plane		85.000		
CP_DCR		5.000	SILICA	24.00
CP_DCR 2nd surf		15.000		24.00
CP_FM_IR		-295.430	Mirror	20.00
CP_TT_IR		24.000	Mirror	62.00
CP_LIR_01 S1	75.515 Ev. Asph: 4th:-7.673e-8 6th:2.810e-11	5.000	S-TIM2	45.40
CP_LIR_01 S2	46.778	12.235	CAF2	45.40
CP_LIR_01 S3	-222.844	118.367		45.40
CP_W_IR		5.000	SILICA	24.00
CP_W_IR 2nd Surf		33.000		24.00
CP_ST_IR		95.572		15.50 (nominal 14.46)
CP_LIR_02 S1	41.500	1.500	SILICA	8.00
CP_LIR_02 S2		3.163		8.00
NIR entrance slit				

Table 10: NIR optical prescriptions.

Element	x (mm)	Y (mm)	Z (mm)	Angle (deg)
Telescope Focal Plane	0.00	0.00	0.00	0.00
CP_DCR	0.00	0.00	85.00	15.00
CP_DCR 2nd surf	0.00	-1.29	89.83	15.00
CP_FM_IR	0.00	-0.45	104.83	45.00
CP_TT_IR	0.00	294.98	104.83	135.00
CP_LIR_01 S1	0.00	294.98	80.83	180.00
CP_LIR_01 S2	0.00	294.98	75.83	180.00
CP_LIR_01 S3	0.00	294.98	63.59	180.00
CP_W_IR S1	0.00	294.98	-54.77	180.00
CP_W_IR S2	0.26	294.98	-59.77	180.00 (3 in y)
CP_ST_IR	0.08	294.98	-92.77	180.00
CP_LIR_02 S1	0.08	294.98	-186.34	180.00
CP_LIR_02 S2	0.08	294.98	-187.84	180.00
NIR entrance slit	0.08	294.98	-191.00	180.00

Table 11: NIR elements vertices coordinates and orientation.

4.3.4 Footprints

In following figures (from Figure 22 to Figure 28) footprints on elements of the CP-NIR are reported.

Different colors represent different positions in the field, e.g. the center and two extremes on the 1” slit.

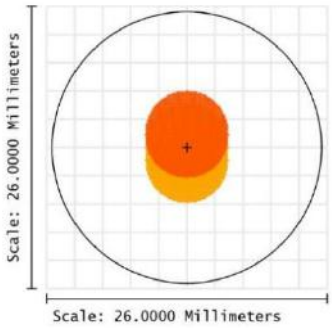

Figure 22: Footprint on CP_DCR first surface.

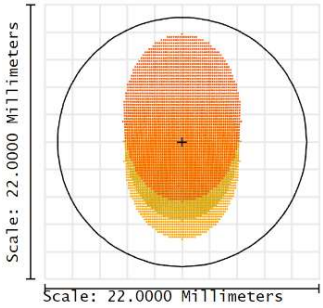

Figure 23: Footprint on CP_FM_IR.

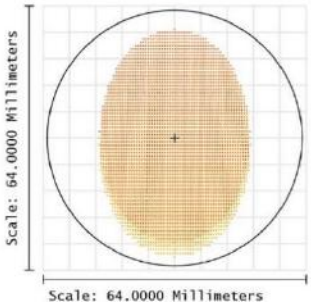

Figure 24: Footprint on CP_TT_VIS.

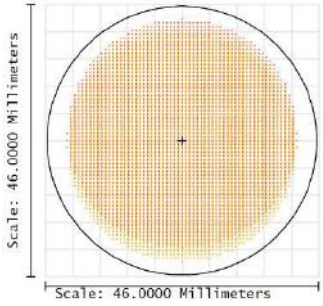

Figure 25: Footprint on CP_LIR_01.

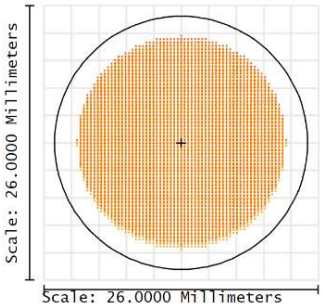

Figure 26: Footprint on CP_W_IR.

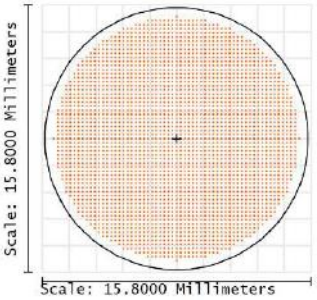

Figure 27: Footprint on CP_ST_IR.

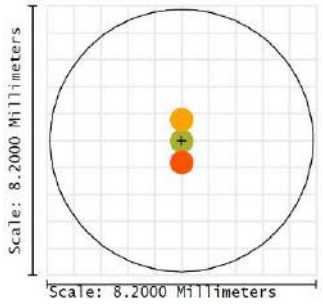

Figure 28: Footprint on CP_LIR_02.

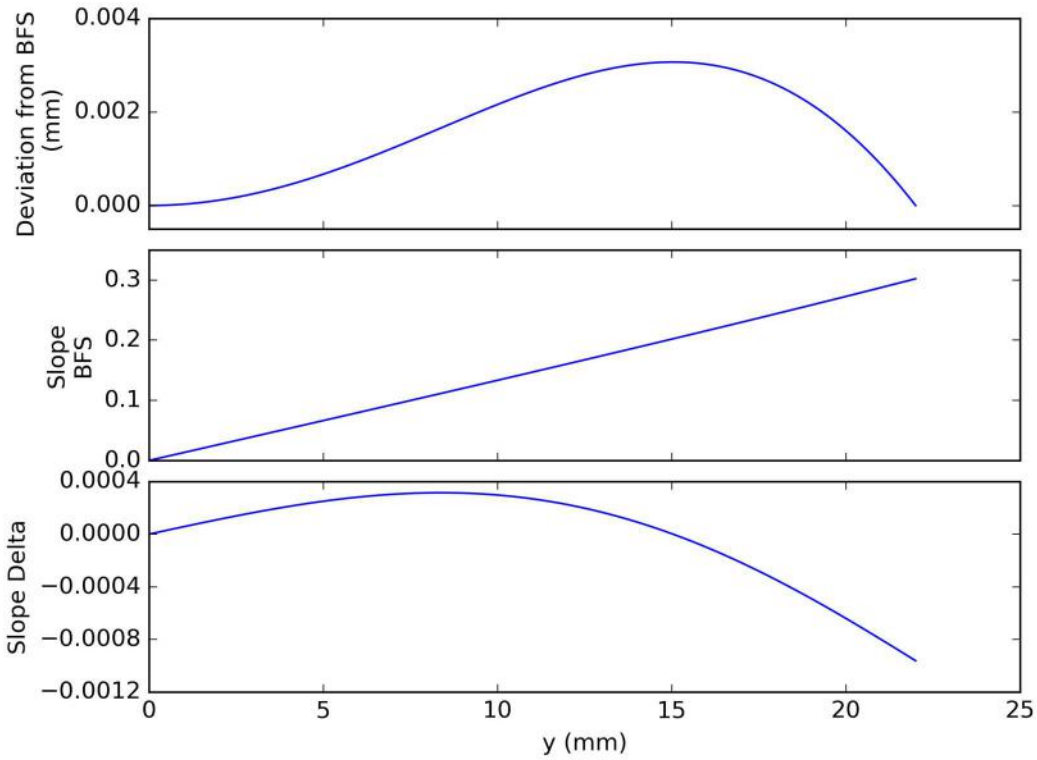

Figure 29: CP_LIR_01 aspherical surface deviation from Best Fitting Sphere (BFS).

4.3.5 Image quality

In Figure 30, spot diagrams for the CP-NIR arm are presented for the center and two extremes of the slit. Boxes of 55 µm corresponds to 0.5 arcsec.

In Figure 31, the encircled energy for the CP-NIR arm is plotted, showing that 80% of the energy is contained in a circle of radius 12.5 µm or ~1/10th of 1 arcsec.

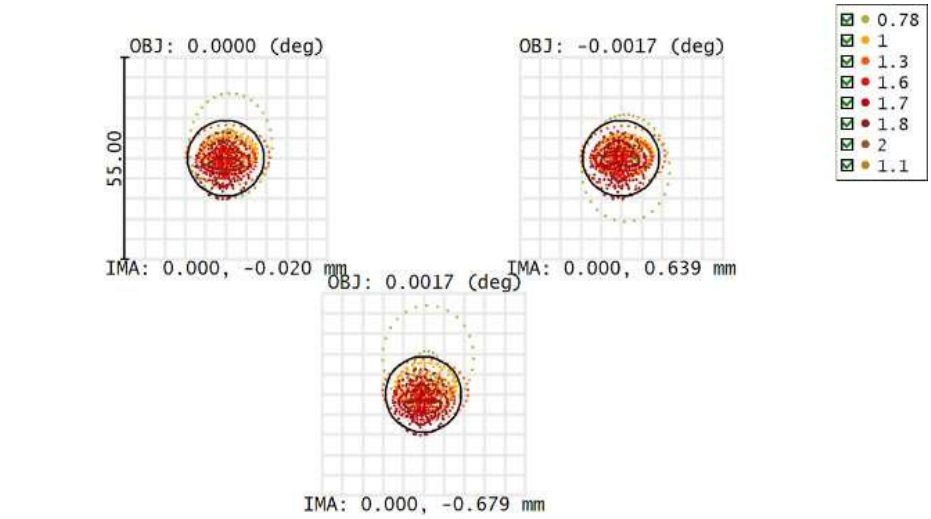

Figure 30: CP-NIR Spot Diagrams.

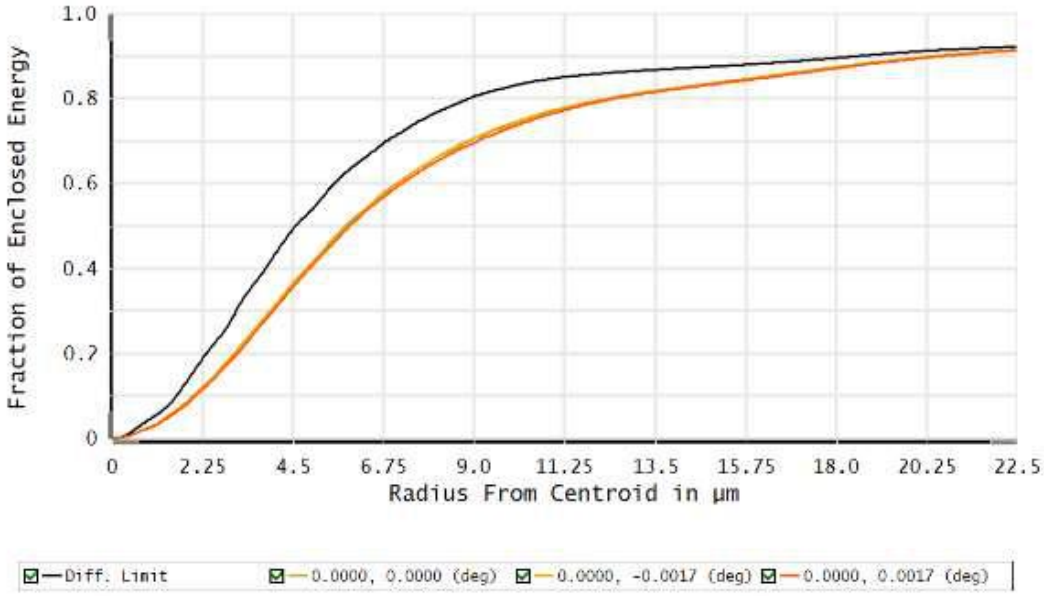

Figure 31: CP-NIR Encircled energy.

4.3.6 Sensitivity analysis

A sensitivity analysis was performed to identify the movements of the image on the slit due to movements of single elements of the CP_NIR. The same coordinate system and nomenclature was adopted as in 4.2.7.

	µm/mm			µm/arcmin		
	dXi/dXe	dXi/dYe	dXi/dZe	dXi/dAXe	dXi/dAYe	dXi/dAZe
	dYi/dXe	dYi/dYe	dYi/dZe	dYi/dAXe	dYi/dAYe	dYi/dAZe
	dZi/dXe	dZi/dYe	dZi/dZe	dZi/dAXe	dZi/dAYe	dZi/dAZe
CP_DCR_IR	0	0	0	0	0	0
	0	0	0	0	0	0
	0	0	0	0	0	0
CP_FM_IR	0	0	0	0	-25	0
	0	0	-835	35	0	0
	0	0	494	0	0	0
CP_TT_IR	0	0	0	0	97	0
	0	0	-835	-137	0	0
	0	0	-489	0	0	0
CP_LIR_02	1545	0	0	0	2	0
	0	1545	0	-2	0	0
	7	6	-562	0	0	0
CP_W_IR	0	0	0	0	0	0
	0	0	0	0	0	0
	0	0	0	0	0	0
CP_LIR_02	45	0	0	0	0	0
	0	45	0	0	0	0
	2	3	-79	0	0	0

Table 12: CP NIR image displacement due to CP NIR elements displacements and tilts.

4.3.7 Tolerance analysis

A preliminary Tolerance analysis has been conducted, in the same manner as in 4.2.8. The used tolerances are in Table 13 and in Table 14. The Montecarlo analysis statistics (Table 15) show that the RMS spot radius (nominal 5.5µm) is 7µm (less than 0.1 arcsec) for 90% of the realizations. The maximum displacement of the focal plane (compensator) is +/-1.2mm.

Used values:

Elements positioning

Element	Dx[mm]	Dy[mm]	Dz[mm]	Tx [deg]	Ty [deg]
CP_DCR	0.2	0.2	0.2	0.2	0.2
CP_FM_IR	0.2	0.2	0.2	0.1	0.1
CP_TT_IR	0.2	0.2	0.2	0.1	0.1
CP_LIR_01	0.2	0.2	0.2	0.2	0.2
CP_W_IR	0.2	0.2	0.2	0.2	0.2
CP_LIR_02	0.2	0.2	0.2	0.2	0.2

Table 13: CP NIR elements displacements and tilts.

Elements manufacturing

- Glasses: Index of refraction +/- 1e-3 (+/- 5e-4 for CAF2); abbe 1%
- Surfaces quality 0.5 fringe (@633nm); first surface of doublet (aspheric) 0.2 fringes
- Curvature: Planarity +/- 3 fringe (1 fringe for mirrors). Radius, 0.1% of radius.
- Thickness +/- 0.2mm
- Elements surfaces mutual positioning (e.g. wedge).

Element	Tx [deg]	Ty [deg]
CP_DCR	0.1	0.1
CP_LIR_01 S2	0.026	0.026
CP_LIR_01 S3	0.050	0.050
CP_W_IR	0.050	0.050
CP_LIR_02	0.1	0.1

Table 14: CP NIR elements manufacturing error (wedge).

Percentage	MF (mm)
90%<	0.0071
80%<	0.0069
50%<	0.0064
20%<	0.0061
10%<	0.0060

Table 15: CP NIR 100 MC realizations statistics.

4.3.8 CP NIR Ghosts

Ghosts, due to double parasite reflections on transmissive elements, are present on the slit plane of the CP NIR.

Given the large distances among elements, the main effects are due to double reflections inside a single element, namely the window, the field lens and the dichroic.

In Table 16 data of the ghosts are reported, calculated as in 4.2.9.

S1	S2	r1	r2	Xmax [mm]	Xmin [mm]	Ymax [mm]	Ymin [mm]	P%	R	A [arcsec^2]
CP_DCR 2	CP_DCR 1	0.05	0.05	0.188	-0.186	-0.853	-1.217	99.8	2.22E-04	11.26
CP_LIR_2 2	CP_LIR_2 1	0.02	0.02	0.217	-0.216	0.215	-0.213	99.8	2.61E-05	15.28
CP_W_IR 2	CP_W_IR 1	0.02	0.02	0.153	-0.838	0.494	-0.492	99.8	4.95E-06	80.73
CP_LIR_2 1	CP_DCR 1	0.02	0.05	3.822	-3.825	3.817	-3.820	99.8	2.07E-07	4826.73
CP_LIR_2 1	CP_DCR 2	0.02	0.05	3.950	-3.953	4.750	-2.901	98.54	1.97E-07	4997.38
CP_LIR_2 2	CP_DCR 1	0.02	0.05	4.674	-4.675	4.689	-4.690	86.48	1.19E-07	7246.91
CP_LIR_2 2	CP_DCR 2	0.02	0.05	4.712	-4.706	4.743	-4.221	77.46	1.11E-07	6977.82
CP_W_IR 2	CP_DCR 2	0.02	0.05	5.073	-4.649	5.138	-4.137	20.07	2.69E-08	7452.40
CP_W_IR 2	CP_DCR 1	0.02	0.05	4.979	-4.776	4.872	-4.871	20.76	2.64E-08	7854.94
CP_W_IR 1	CP_DCR 2	0.02	0.05	4.823	-4.821	4.985	-4.212	19.14	2.61E-08	7330.16

Table 16: CP NIR Ghost data.

As noted above, the highest R ghosts are those due to internal reflections in one element.

The most intense ghost is due to the dichroic (mostly for the 5% reflectivity) and is 2.2e-4 times less intense than the nominal image; the ghost due to the field lens 10 times weaker, while that due to the window approx. 40 times less. All other ghosts, due to inter-elements interactions, are much weaker (3 orders of magnitude).

Note that due to the non-perpendicularity of dichroic and window faces w.r.t. to the beam chief ray, the ghosts due to these elements are only partially or not at all entering in the slit.

The ghost due to the dichroic is decentered along the long side of the slit by about -360 µm, and for a source on axis it will not be on the slit (roughly 660x2 µm long). A source imaged on the 'top' of the slit will on the other hand, form a ghost on the lower part of the slit (not arriving to superimpose on the center of the field).

The ghost due to the window is decentered along the short side of the slit by approx. 320 µm, but with a size of 500 µm, it will be superimposed to the center of the field. The two scenarios are shown in Figure 32.
Even considering all the possible ghosts, and summing up their intensity (disregarding the fact that not all will be superimposed in the same positions), the total ratio is still <2.5e-4.

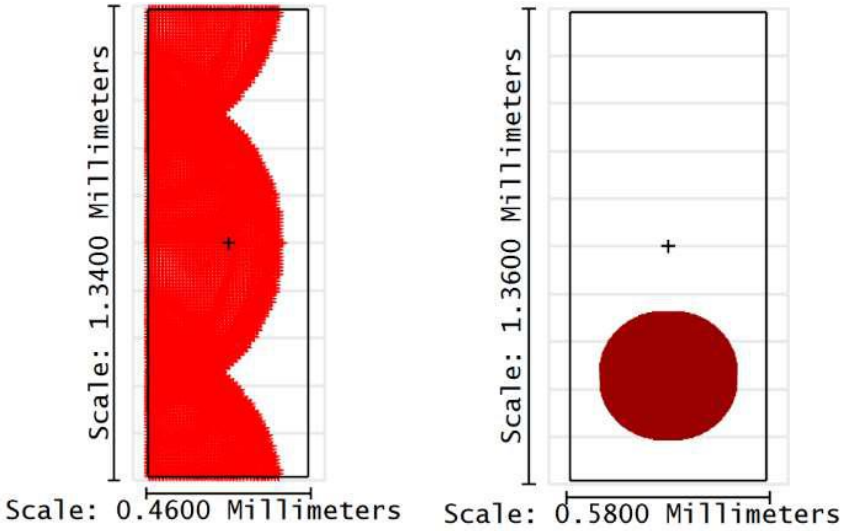

Figure 32: Ghosts due to window (left) and to dichroic (right) for a 12x5 arcsec slit.

4.4 CP Thermal behavior

The Common Path nominal design assumes a working temperature of T=10 °C. We model here how slits and best focus position change within the [0°C-20°C] range, in order to understand if temperature changes may cause defocus and/or wandering (on the slit plane) of the image at the entrance of the spectrographs. In the following discussion, the coordinate system is as follows (Figure 33):

Origin: Nominal centre of the flange
Z: perpendicular to the flange, towards CP (away from telescope)
Y: on the plane of the flange, from O towards UVVIS slit nominal centre
X: completes the system

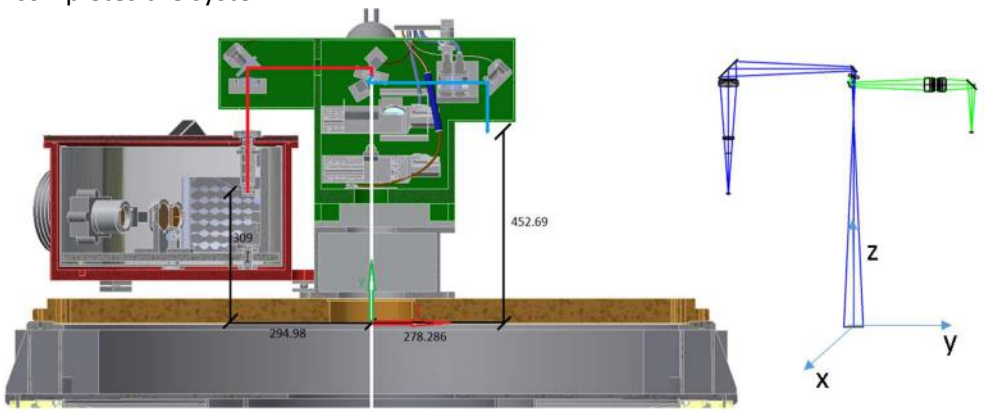

Figure 33: Coordinate reference frame.

4.4.1 Slits Position

The position of the slit is extensively discussed in the Mechanical Design document [RD1]. Here we simply present the results for five different temperatures (Table 17), i.e. the delta of position

coordinate for the mechanical slits due to variations of temperature.

		0°	5°	10°	15°	20°
UVVIS	Δ_X (mm)	0.000	0.000	0.0000	0.000	0.000
	Δ_Y (mm)	-0.064	-0.032	0.0000	0.032	0.064
	Δ_Z (mm)	-0.012	-0.006	0.0000	0.006	0.012
		0°	5°	10°	15°	20°
NIR	Δ_X (mm)	0.000	0.000	0.0000	0.000	0.000
	Δ_Y (mm)	0.070	0.035	0.0000	-0.035	-0.070
	Δ_Z (mm)	-0.012	-0.006	0.0000	0.006	0.012

Table 17: Slit position offset in µm w.r.t. nominal temperature of 10C.

4.4.2 Best focus position

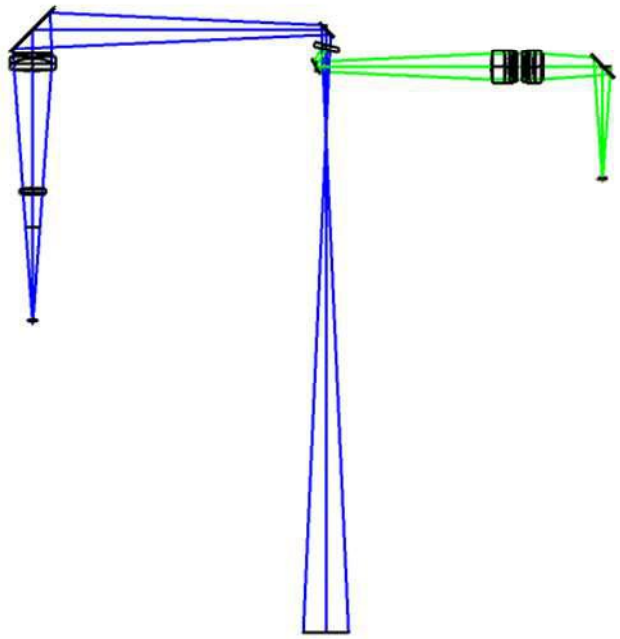

Figure 34: Common Path Optical Layout from the flange interface to NIR (blue) and UVVIS (green) focus positions.

For the optical analysis, we adopted the nominal position of the back of the flange centre as the Global Coordinate reference. The system was evaluated at five temperatures: 0, 5, 10, 15, and 20°C.
The Z displacement of the flange, due to temperature variations has been accounted for by inserting a surface of variable thickness (-20 µm for T=0, -10 µm for T=5 etc.) which displaces the entire CP w.r.t. the nominal position of the Flange. 20 µm is the rounding of the calculated flange thermal expansion and its uncertainty (12+/-5 µm, see Mechanics Design document) and is considered to be a pessimistic evaluation.
We introduced a CTE= 23×10^{-6} K^{-1} for all the remaining distances up to the last mirror in the UVVIS arm and last lens in the NIR arm. All the elements are assumed to be at the same temperature (0, 5, 10, 15, 20°C). The thermal behavior of the real mounting points of the lenses has been ignored, and for the NIR arm, the different temperature of the cryogenic part has been disregarded. Moreover, no variations have been introduced in the telescope temperature, i.e. the telescope is supposed to be athermal.
The absolute coordinates of the Best Focus position (after a quick focus) and changes w.r.t. the nominal

position are summarized in the following table.

		0°	5°	10°	15°	20°
UVVIS	X (mm)	0.0000	0.0000	0.0000	0.0000	0.0000
	Y (mm)	278.2274	278.2569	278.2864	278.3160	278.2864
	Z (mm)	452.6768	452.6844	452.6915	452.6981	452.7041
	Δ_X (mm)	0.000	0.0000	0.0000	0.000	0.0000
	Δ_Y (mm)	-0.059	-0.030	0.0000	0.030	0.059
	Δ_Z (mm)	-0.015	-0.007	0.0000	0.007	0.013
		0°	5°	10°	15°	20°
NIR	X (mm)	0.0809	0.0809	0.0809	0.0809	0.0809
	Y (mm)	-294.9118	-294.9458	-294.9797	-295.0137	-295.0477
	Z (mm)	308.9939	309.0015	309.0088	309.0157	309.0223
	Δ_X (mm)	0.000	0.000	0.0000	0.000	0.000
	Δ_Y (mm)	0.068	0.034	0.0000	-0.034	-0.068
	Δ_Z (mm)	-0.015	-0.007	0.0000	0.007	0.014
Lens shift	Delta Y [mm]	0.1	0.05	0.00	-0.05	-0.1

Table 18: Best Focus position and its delta w.r.t. nominal for different temperatures.

From these data, it appears that the position of the best focus (Z axis) is within a range of ~20 µm for the UVVIS, and similar figures for the NIR (after the NIR lens doublet, mounted on a motorized system, is moved by +/- 100 µm).

We stress that these figures are obtained assuming that the Telescope Focal Plane best position remains fixed in the global coordinates system, at (0,500,0) mm from the nominal flange centre (O).

The spot diagrams on the nominal position of the slit are essentially constant, as can be seen by the following two spot diagrams, at T=10C and T=20C for UVVIS arm.

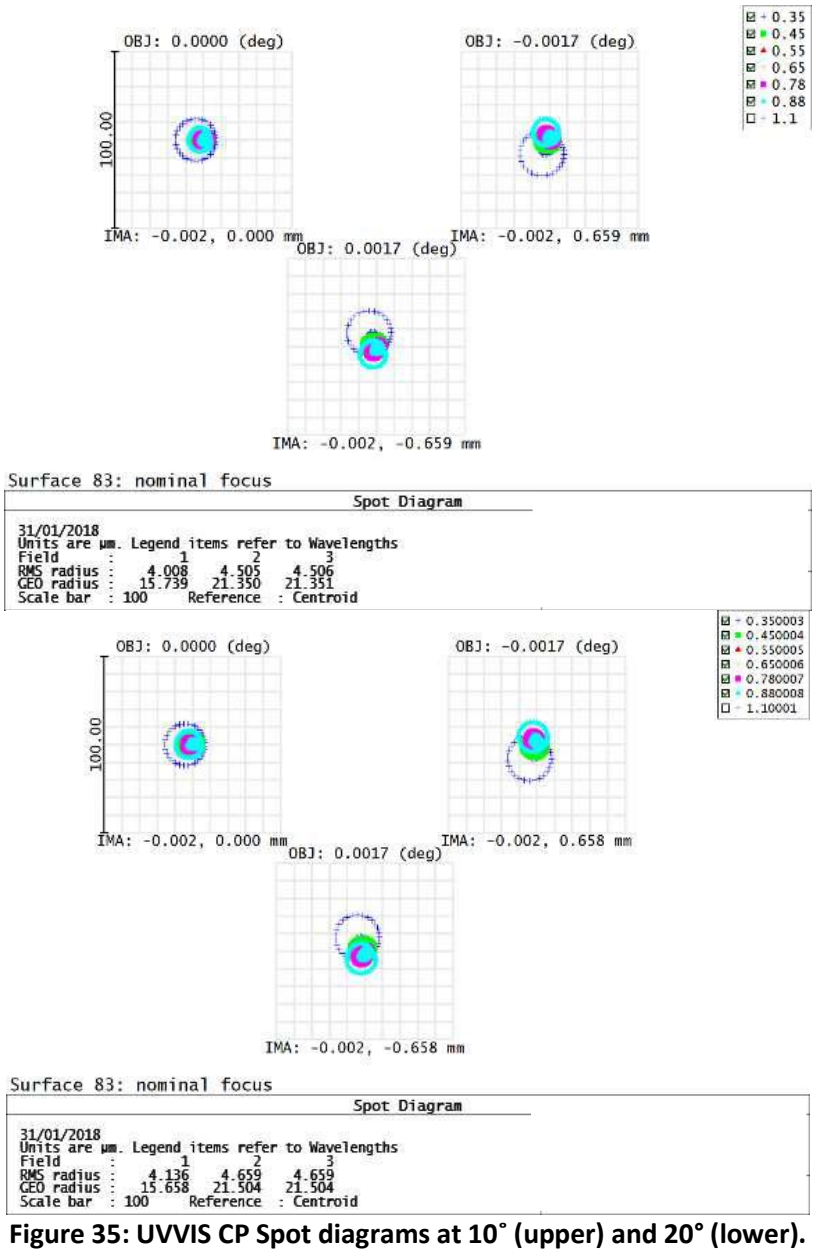

Figure 35: UVVIS CP Spot diagrams at 10˚ (upper) and 20° (lower).

4.4.3 Image displacement on the slit

If we compare the positions of the slits and best focus for different temperatures presented in Table 17 and Table 18, we can conclude that:

- On the plane XY (parallel to the flange), the image and the flange itself will expand by the same values: 0 mm in tangential directions and ~0.07 mm in radial directions. Assuming that the slit is co-moving with the flange, no movement of the image on the slit will be present. If we consider a 10-20% error in analyses due to CTE inhomogeneity or differences in flange and CP, modelling, etc., we can expect a possible ~15 µm movement along the 1320 µm long slit.
- On the Z direction, Focus remains in the nominal position in +/-15 µm range for both arms (refocusing NIR CP). This takes into account a +/-20µm displacement of the flange.

Given these figures, the displacement of the image on the slits will depend essentially on how the mechanical slit will move, inside the spectrographs, w.r.t. the nominal position inside the spectrographs themselves, and on how the spectrographs will 'co-move' with the flange.

4.5 Tip-Tilt Mirrors

To correct for misalignment between the two spectrographs, the adoption of two tip tilt mirrors in the CP is foreseen. A complete analysis of the deformation will be present in [RD1] at the FDR, but preliminary figures for the displacement of images produced by the CP due to mechanical flexures of optical elements are in the order of +/-50 µm (about +/-0.4 arcsec in sky).
Consequently, we assumed a minimal correction of 5 µm (0.04 arcsec) and requested that whatever is the correction, the pupil position should not vary more than 1% of its diameter.
For space and accessibility reasons, we plan to use as Tip-Tilt mirrors the 'external' mirrors of both arms, i.e. CP_TT_VIS and CP_TT_IR.
For the NIR Arm, the pupil requirement translates in a maximum tilt of the tip-tilt mirror of about +/-2 arcmin, while for the UVVIS arm it is about +/-4 arcmin. From values of Table 4 and Table 12, this translates to a maximum correction of about 200 µm for both arms, while the requested precision (5 µm) is in the order of 30-15 microrad.
The selected tilt motor PI S-330.2SH assures a range of about 7 arcmin, a resolution of 5e-2 microrad and a repeatability of 15e-2 microrad, 2 orders of magnitude smaller than the minimal correction requested.

5 UV-VIS Spectrograph

5.1 Overall Description

The SOXS UV-VIS spectrograph is based on a novel concept in which the incoming beam is partitioned into four polychromatic beams (quasi-orders) using dichroic surfaces, each covering a waveband range of ~100 nm. Each quasi-order is diffracted by a custom-made ion-etched grating. The four beams enter a three-element catadioptric camera that images them onto a common detector. The goal of the partitioning is to maximize the overall system throughput.

5.2 Optical layout

SOXS UV-VIS is divided into two levels, both conceptually and mechanically (see Figure 36). The first level divides the CP beam into four collimated beams, each covering a different wavelength range. The second level includes the dispersers and camera – imaging the spectra of each quasi-order to a common detector.

The beam from SOXS CP is directed into the UV-VIS enclosure and is folded by a flat pickup mirror with a diameter of ϕ=12.7 mm located 30 mm downstream from the CP focus. The beam intercepts a ϕ=76.2 mm off-axis-parabolic mirror at an angle of 30°, creating a collimated beam with a diameter of ϕ=45 mm The collimated beam is partitioned into four beams using flat dichroic mirrors at $\sim 45^{\circ}$ AoI. The 1st element each beam intercepts in the 2nd level is the ion-etched gratings. These are tilted by 45° wrt the Nasmyth flange so that the incidence angle of the collimated beam is ~41°. The dispersed beams are then imaged by the catadioptric camera onto the common detector. The field flattener also serves as cryostat window, and is inserted through a rectangular aperture in the camera's corrector. The detector, an e2V CCD44-82 CCD, is located 4 mm behind the field flattener back surface.

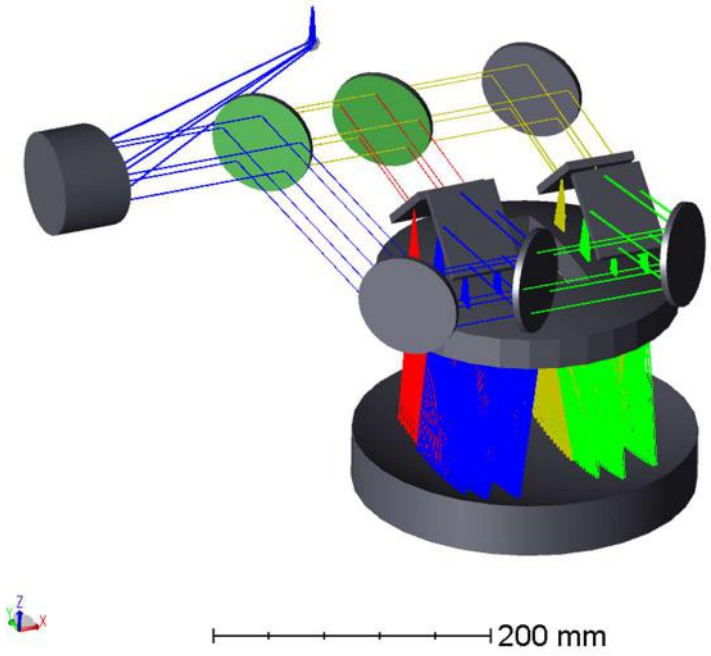

Figure 36: SOXS UV-VIS Spectrograph.

Quasi-Order	Wavelength Range [nm]
u	350 – 440
g	427 – 545
r	522 – 680
i	656 – 850

Table 19: SOXS UV-VIS Quasi-Orders.

5.2.1 First order parameters

The system 1st order parameters are listed in Table 20. A Zemax and CAD file of the system is attached to this document.

Collimator Focal Ratio	6.5
Collimator Beam diameter	45 mm
Spectral range	350-850 nm
Resolution (1 arcsec slit)	3500-7000
Slit scale	110 um/arcsec
Foreseen slit widths	0.5 – 1.0 – 1.5 – 5.0 arcsec
Silt height	12 arcsec
Camera Output Focal Ratio	3.11
Detector	e2V CCD44-82
Detector Scale	~53 µm/arcsec
Main Disperser	Four custom ion etched gratings
Working temperature	Ambient (−5C − 20C)

Table 20: UV-VIS Spectrograph 1st Order Parameters.

5.2.2 Optical prescription

5.2.2.1 Collimator

The system collimator is a 30° off-axis-parabola (OAP) with an EFL of 272.55 mm and an off-axis distance of 146.3 mm. The F/# is matched to the CP (F/6.5) yielding a ϕ=45 mm beam. The F/# and desired beam width dictate a reflected focal length (RFL) of 292.12 mm. We choose a 30° OAP over a higher AoI OAP due to improved manufacturability and coating efficiency for low incidence angle OAPs. This results in the pupil not falling directly on the grating, but due to the high uniformity of ion-etched gratings and the small FoV, this is not expected to affect the spectrum, nor does it significantly increase the grating's clear aperture.

5.2.2.2Feed

Our system includes three dichroic surfaces to divide the beam into four quasi-orders. Each quasi-order beam is reflected/transmitted by two dichroic surfaces. The first one is a dichroic mirror tilted at ~ 45 deg reflecting *u*+*g* and transmitting *r*+*i*. The two beams are than further divided by secondary dichroic mirrors which are tilted at ~ 45° to ensure proper positioning of the beams on the gratings. The transmitted beams (*g* + *i*) are finally reflected towards their gratings by dielectric mirrors at ~ 45°. The mirrors are rotated by a few degrees to feed the gratings at the designed 41° AoI.

5.2.2.3Gratings and Resolution

The SOXS UV-VIS arm uses four ion-etched gratings from the Fraunhofer Institute as the system dispersers. We chose the grating parameters (line density, diameter, and feed angle) so that the following conditions are realized:

- Littrow angle is roughly ~ 41° at each quasi-order center to maximize efficiency.

- Average resolution > 4500 for all of the quasi-orders.
- Resolution for a 1 arcsec slit is > 3500 across the entire band, and is > 4000 for at least 75% of the quasi-order.

The grating parameters are given in Table 21.

Quasi-Order	Wavelength Range [nm]	Line Density (lines/mm)	Feed Angle [°]	$\lambda_{Littrow}$ [nm]
u	350 – 440	3380	41	388.2
g	427 – 545	2655	41	494.2
r	522 – 680	2070	41	633.9
i	656 – 850	1660	41	790.4

Table 21: Grating parameters.

Resolution vs. wavelength is reported in Figure **37**. Average resolution and standard deviation across each quasi-order is given in Table 22.

Quasi-Order	$\bar{R}$	$\sigma(\bar{R})$
u	4995	1059
g	4634	890
r	4633	909
i	4601	878

Table 22: Average Resolution.

The resolution is calculated by ray tracing the centroid position on the detector for each wavelength, taking into account the slit width (1”), and the diameter of the enslitted energy (see section 5.3). The wavelength solution is interpolated with an 8th degree polynomial.

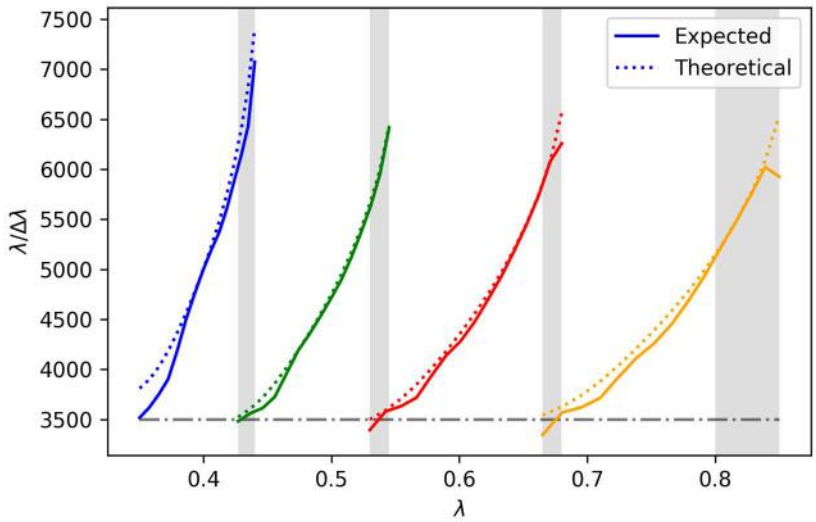

Figure 37**: Spectral resolution for 1 arcsec slit. The shaded regions are the spectral overlap regions both between the quasi orders and between the UV-VIS and NIR arms. The dotted lines are the theoretical resolution plots for the gratings given their characteristics. This figure shows there is only minimal degradation due to optical aberrations.**

5.2.2.4 Camera

The optical prescription of the camera is shown in Table 23, and its layout is shown in Figure 38. The camera is made of three aspheric elements and is inspired by the camera designed for MOONS (RD13).

The first element is a CaF2 aspheric corrector with a rectangular aperture removed from its center. The second element is an aspheric fused silica mirror. The third and last element is an aspheric field flattener which is cut into a rectangular shape, and serves also as the window of the cryostat. The sag of the aspheric surfaces is shown in Figure 39. The aspheric departures are not challenging for modern manufacturing techniques.

The camera's focal length is ~140 mm, and functions as four F/3.1 off-axis cameras. The two materials (CaF2 and fused silica) suffer essentially zero absorption in the relevant wavelength range. We have worked closely with potential manufacturers, to comply with manufacturing requirements. For the corrector and mirror we keep a 15 mm mechanical margin on the clear aperture.

Name	**Radius (mm)**	**Thickness (mm)**	**Material**	**CA SDIA (mm)**	**Mechanichal SDIA(mm)**	**Asphere *4th,6th,8th***
Asphere Corrector	324.88	25.00	F SILICA	93	110	
	456.46			93	110	2.20E-08, 3.87E-13, 9.21E-18
Air	Infinity	146.31				
Mirror	328.28		MIRROR	108	125.00	9.83E-10, 5.34E-14, -7.06E-19
Air	Infinity	123.61				
Detector Window	70.24	30.00	F SILICA	15 × 42	18 × 46	4.81E-07, -6.88E-11, 9.06E-14
	Infinity	4.00		3.5 × 35	18 × 46	

Table 23: Camera prescription.

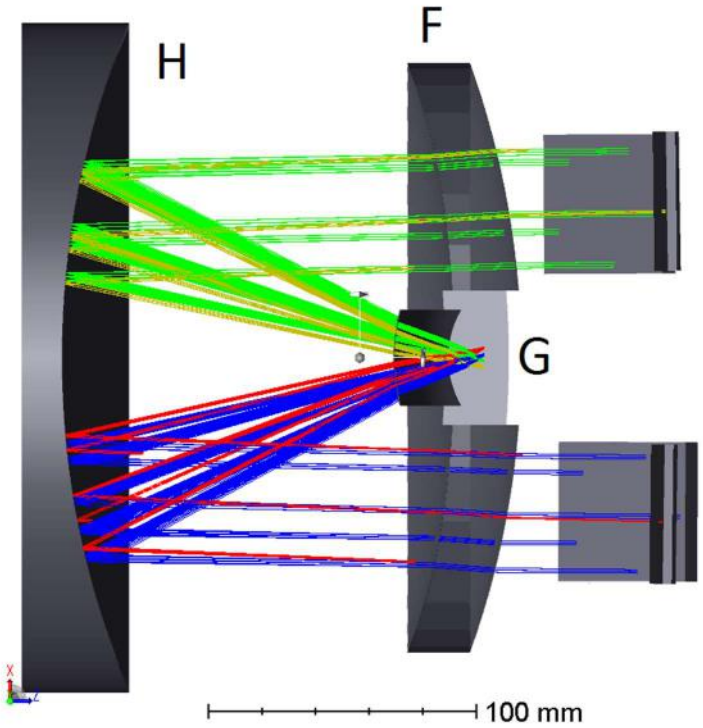

Figure 38: optical layout of the camera. F,G,H are the CaF2 corrector, fused silica field flattener, and the aspheric mirror, respectively.

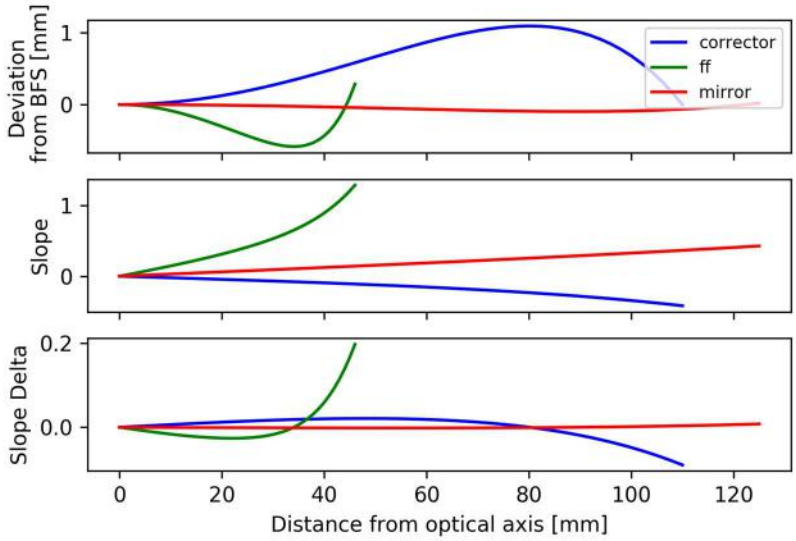

Figure 39: UV-VIS Aspheric surfaces deviation.

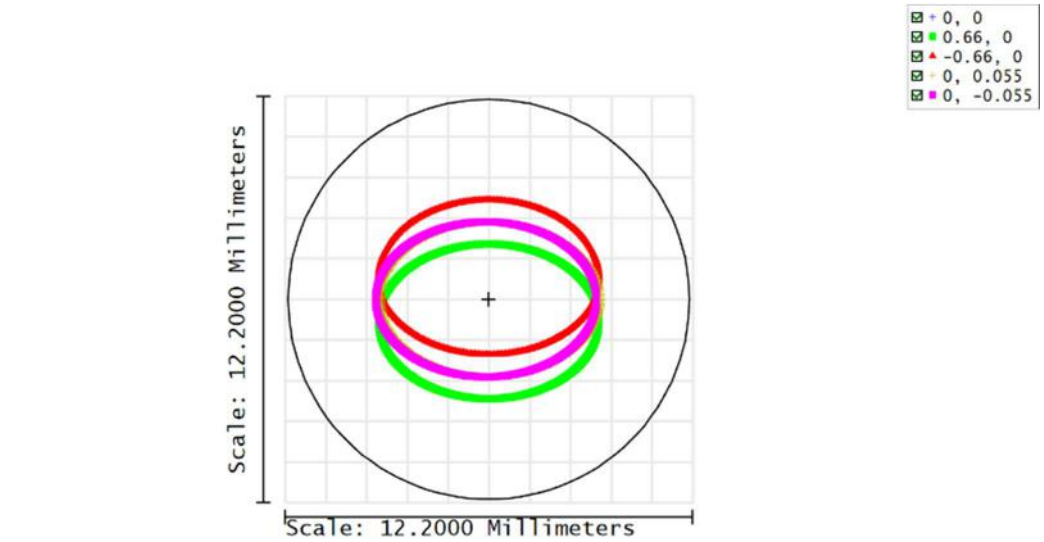

Aperture Diameter: 12.0000

Footprint Diagram	
28/03/2018 Surface 3: Pickup mirror Ray X Min = -3.3761 Ray X Max = 3.3641 Ray Y Min = -2.9807 Ray Y Max = 2.9807 Max Radius= 3.4209 Wavelength= All Legend items refer to Field positions	Zemax Zemax OpticStudio 17 SOXS_feb7_AspherMirror_v0004.zmx Configuration 1 of 4

Figure 40: Footprint on pickup-mirror.

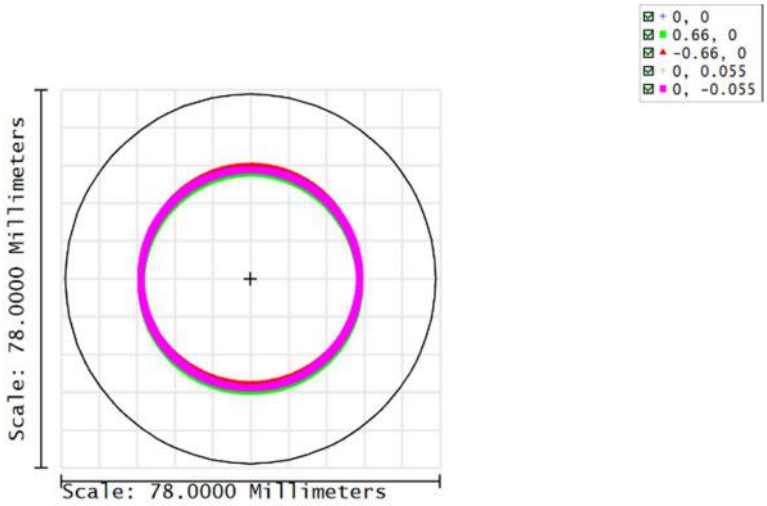

Aperture Diameter: 76.2000

Footprint Diagram	
28/03/2018 Surface 7: OAP Ray X Min = -22.5547 Ray X Max = 22.5547 Ray Y Min = -23.1643 Ray Y Max = 23.1518 Max Radius= 23.1643 Wavelength= All Legend items refer to Field positions	Zemax Zemax OpticStudio 17 SOXS_feb7_AspherMirror_v0004.zmx Configuration 1 of 4

Figure 41: Footprint on OAP.

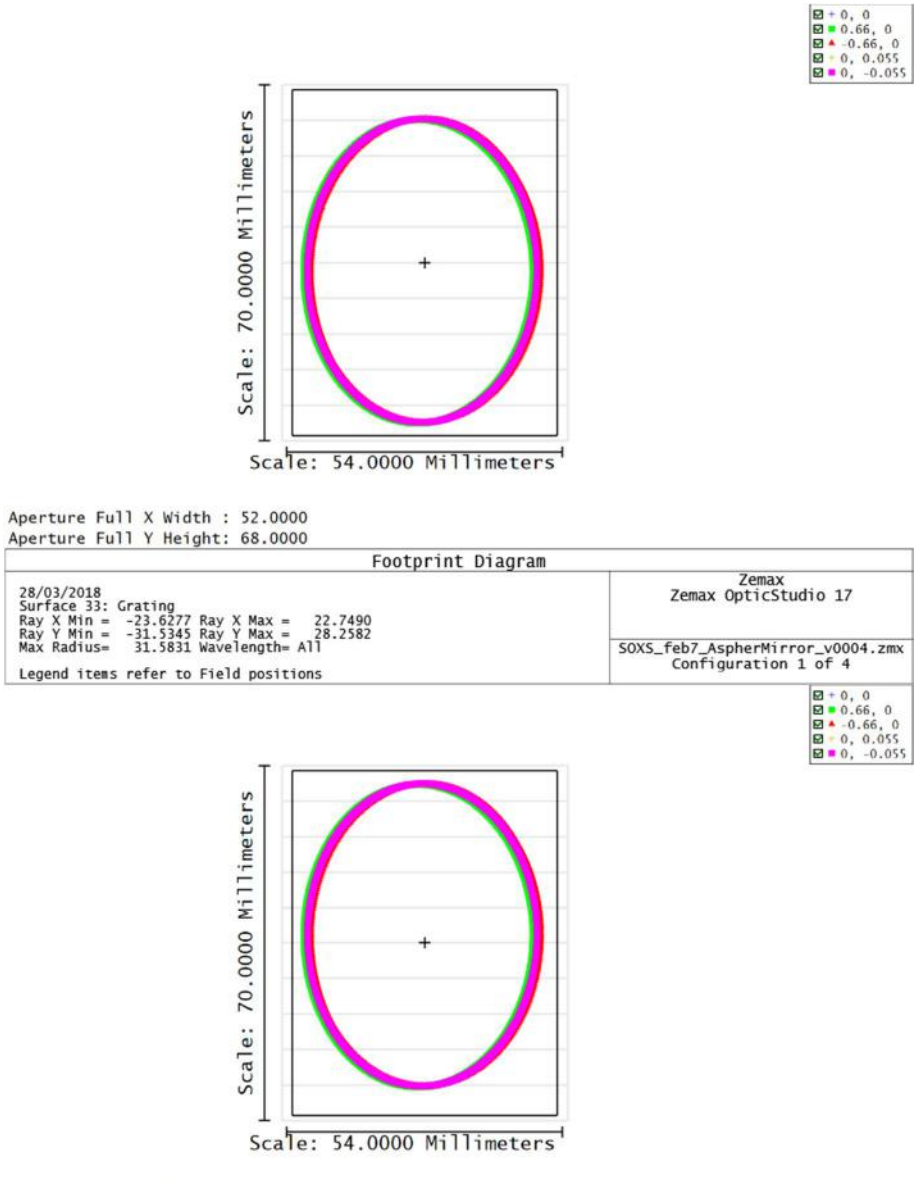

Figure 42 Footprint on u-band gratings on the entrance surface (top) and exit surface (bottom). Shown are the fields ±6'' in the cross-dispersion, and ±0.5'' in the dispersion direction (not visible due to symbol sizes).

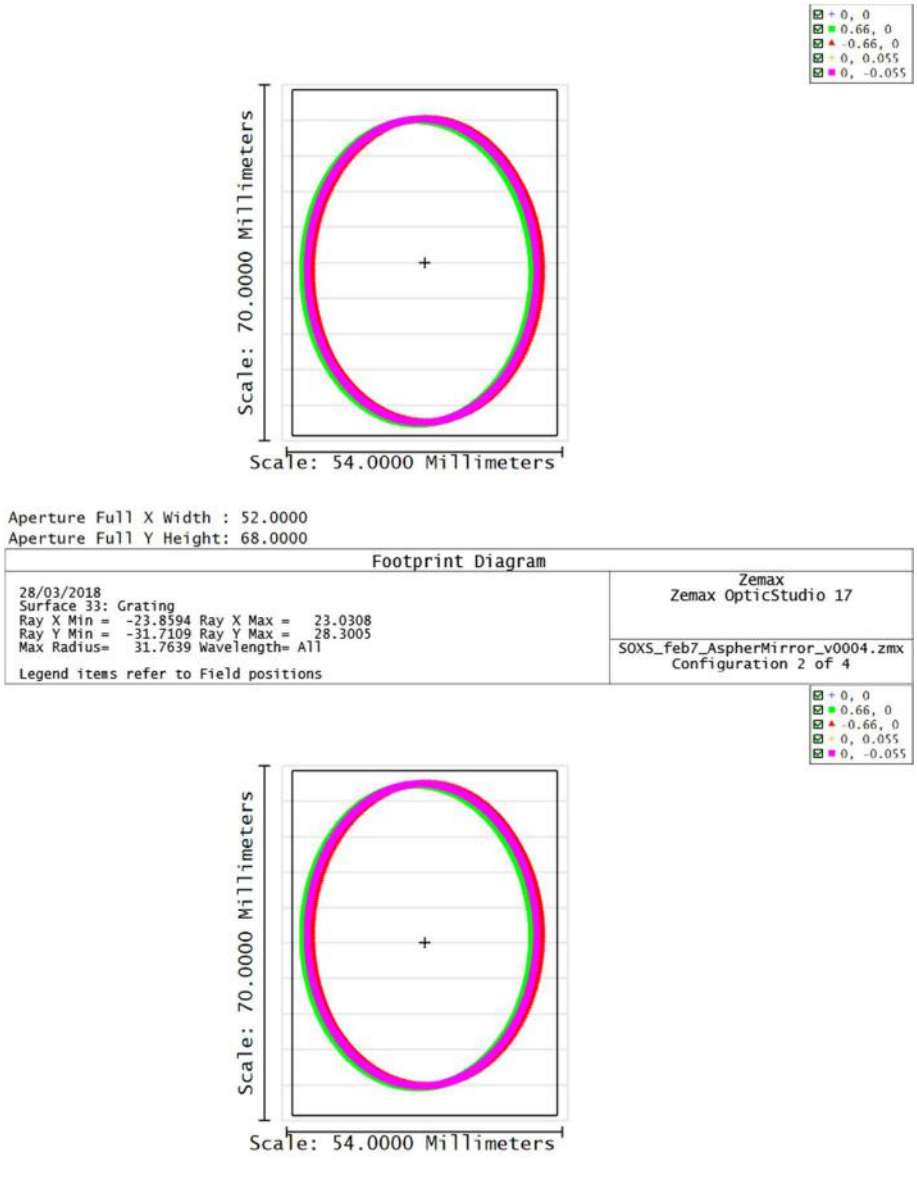

Figure 43: Footprint on g-band gratings on the entrance surface (top) and exit surface (bottom). Shown are the fields ±6'' in the cross-dispersion, and ±0.5'' in the dispersion direction (not visible due to symbol sizes).

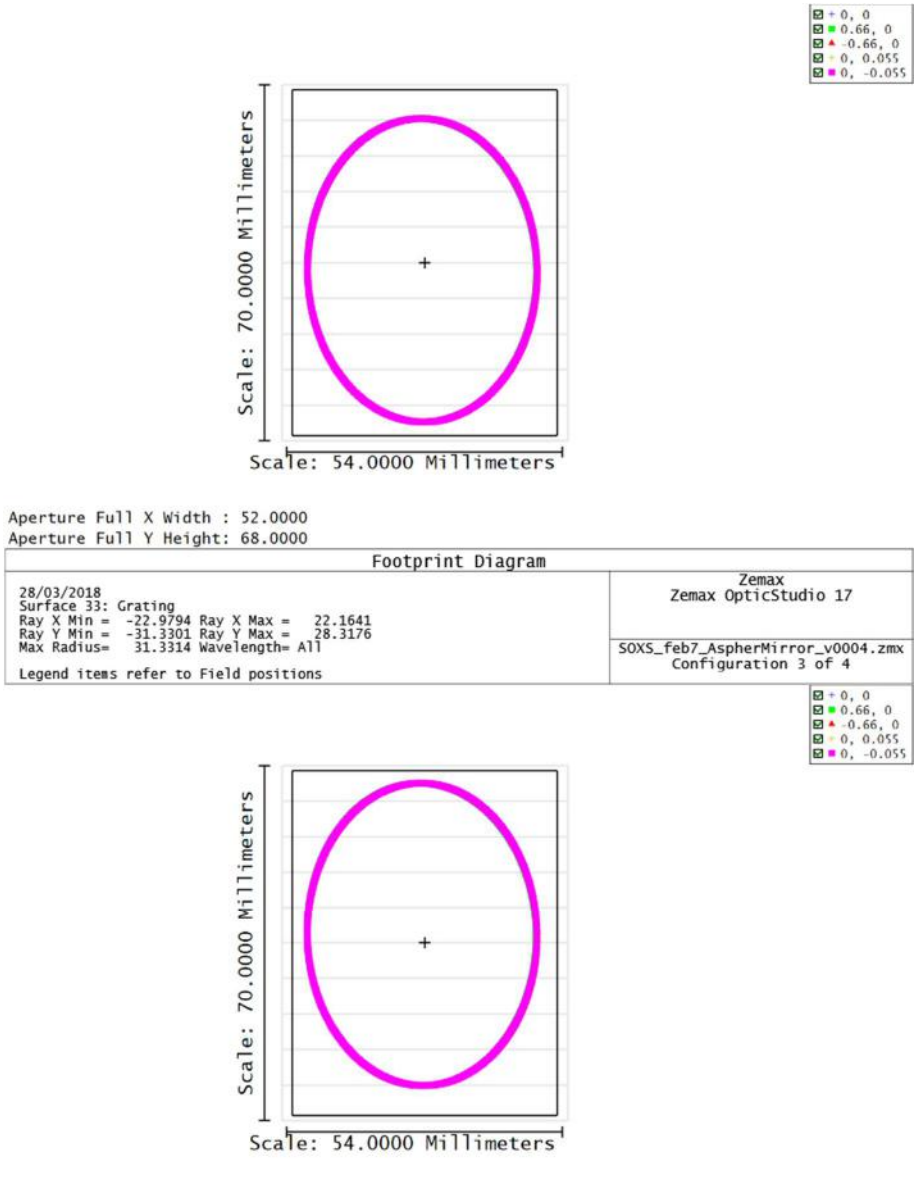

Figure 44: Footprint on r-band gratings on the entrance surface (top) and exit surface (bottom). Shown are the fields ±6'' in the cross-dispersion, and ±0.5'' in the dispersion direction (not visible due to symbol sizes).

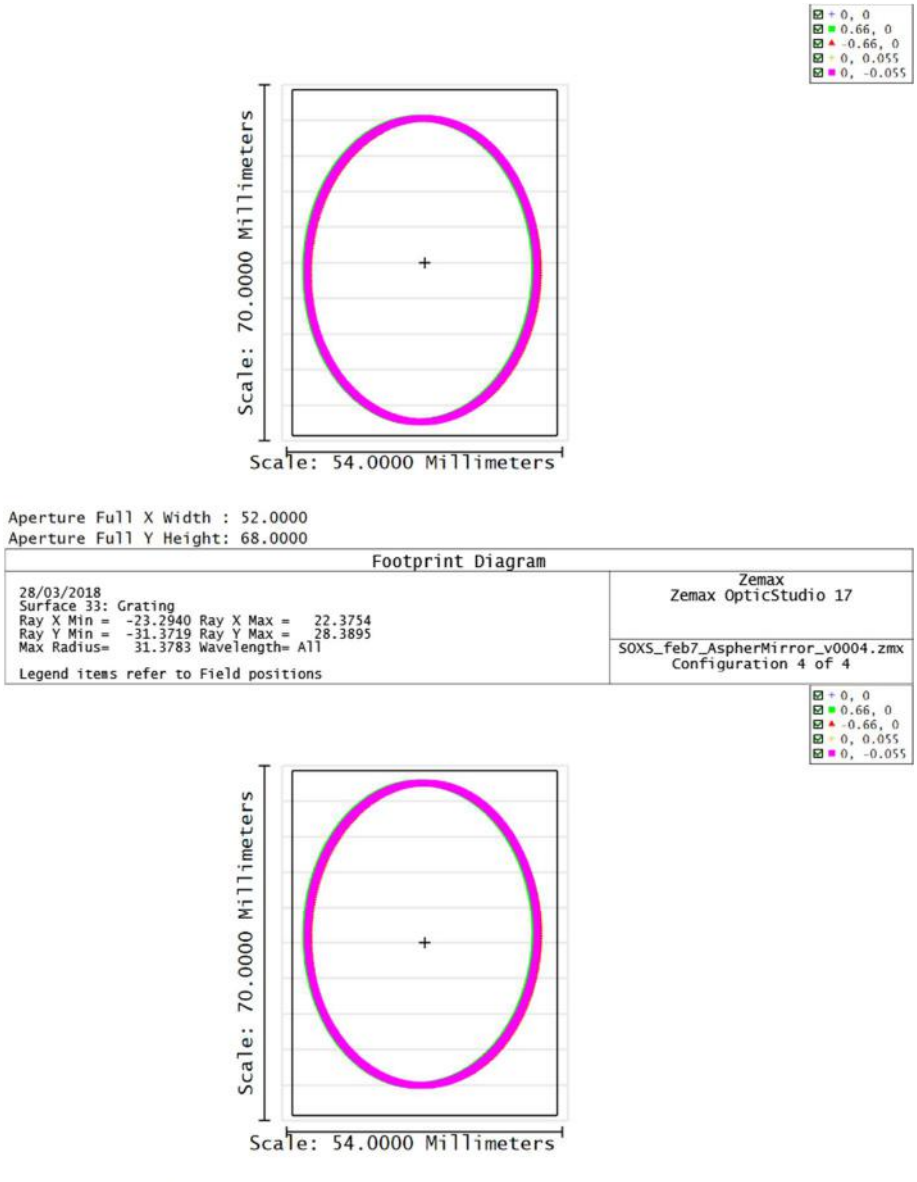

Figure 45: Footprint on i-band gratings on the entrance surface (top) and exit surface (bottom). Shown are the fields ±6'' in the cross-dispersion, and ±0.5'' in the dispersion direction (not visible due to symbol sizes).

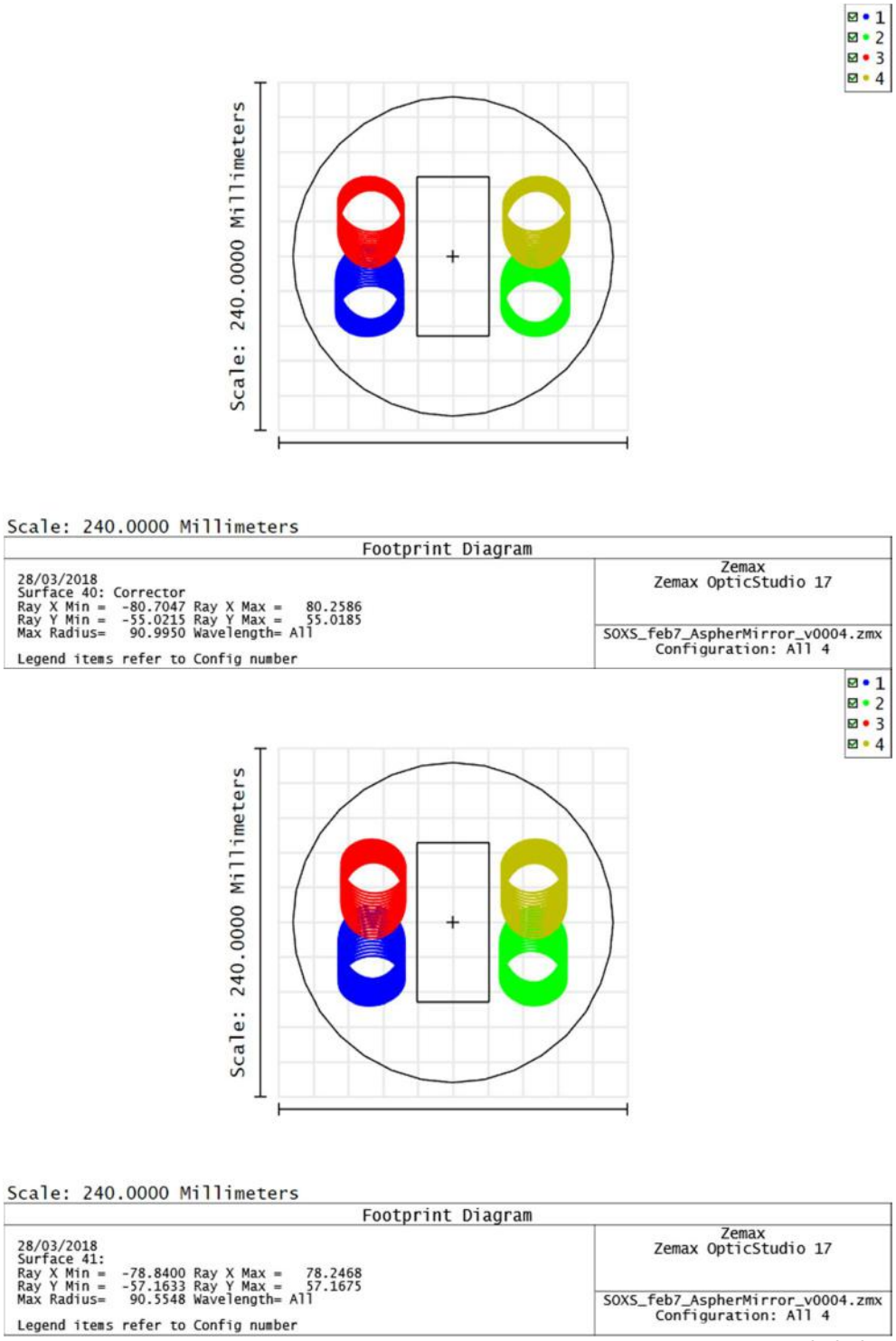

Figure 46: Footprint on the CaF2 corrector entrance (top) and exit (bottom). 1/2/3/4 represent u/g/r/i.

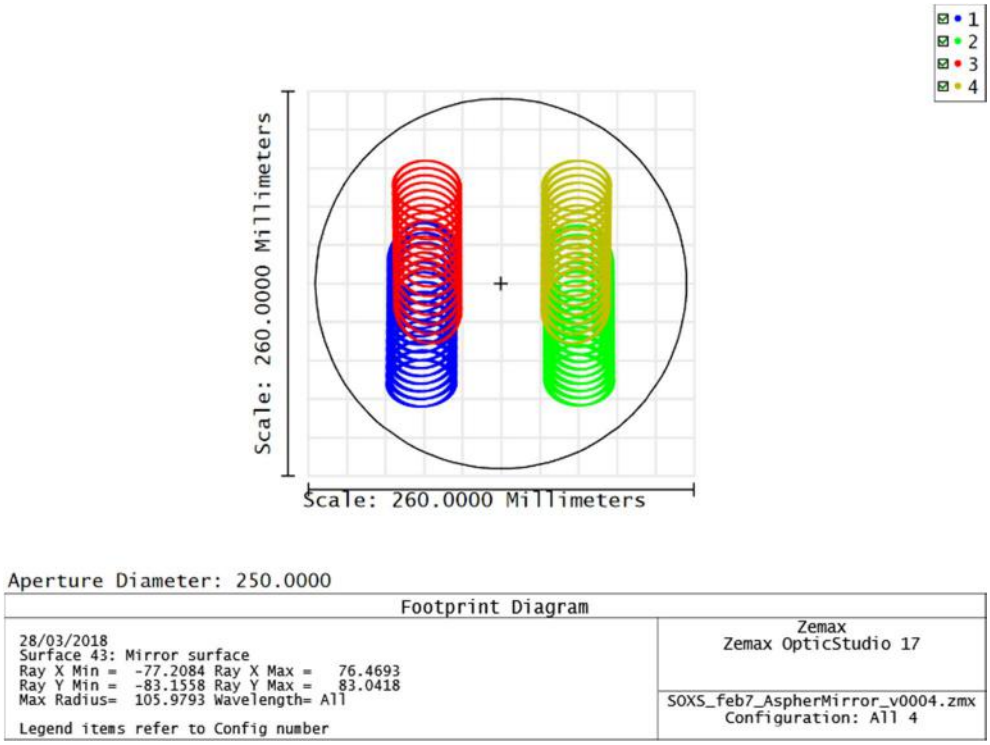

Aperture Diameter: 250.0000

Footprint Diagram	
28/03/2018 Surface 43: Mirror surface Ray X Min = -77.2084 Ray X Max = 76.4693 Ray Y Min = -83.1558 Ray Y Max = 83.0418 Max Radius= 105.9793 Wavelength= All Legend items refer to Config number	Zemax Zemax OpticStudio 17 SOXS_feb7_AspherMirror_v0004.zmx Configuration: All 4

Figure 47: Footprint on the aspheric mirror. 1/2/3/4 represent u/g/r/i.

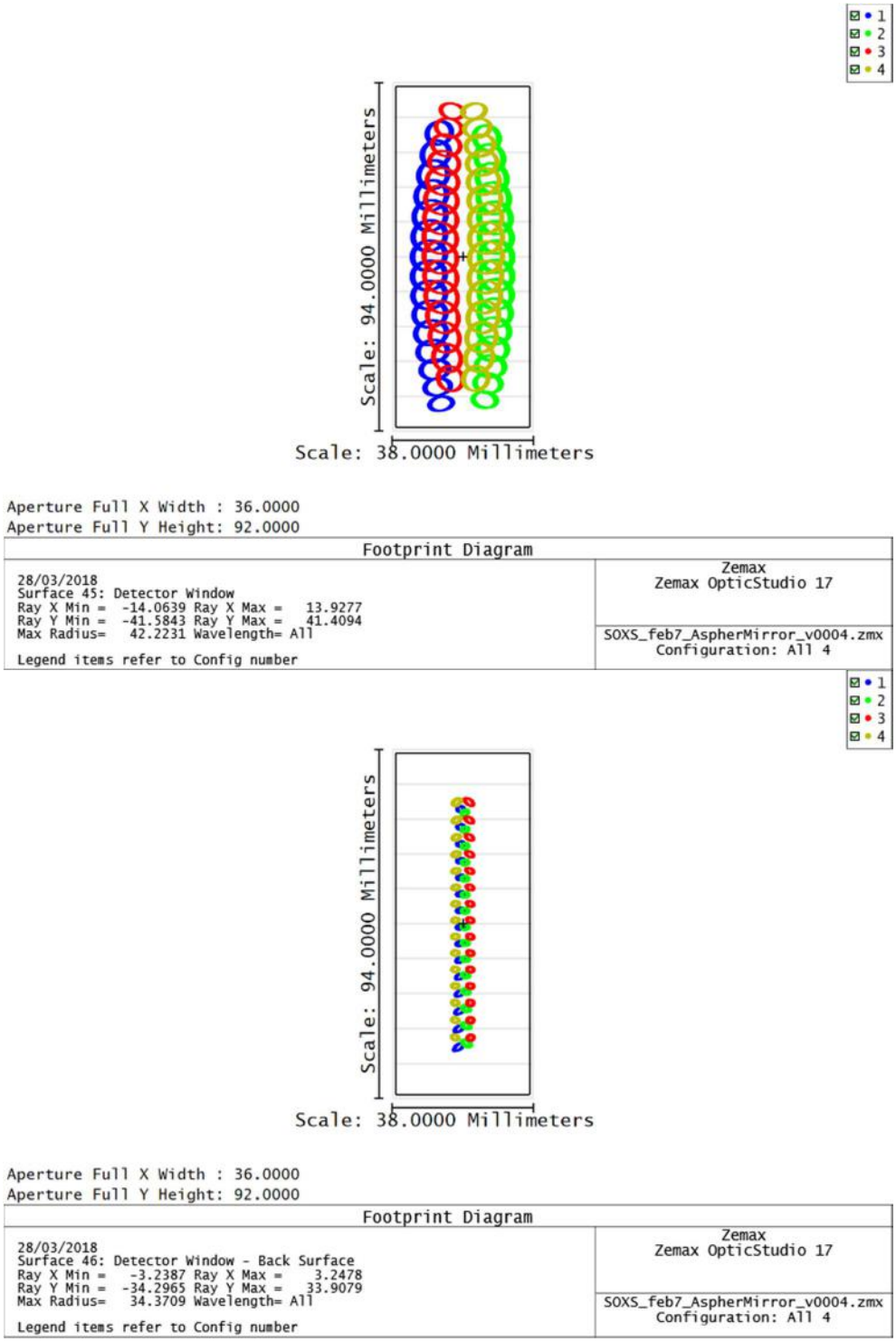

Figure 48: Footprint on the fused silica field flattener entrance (top) and exit (bottom). 1/2/3/4 represent u/g/r/i.

5.2.3 Detector system

The UV-VIS CCD detector system for SOXS is designed to reach a wavelength response from 350 to 850 nm. It consists of an E2V CCD44-82 2k x 4k CCD, a detector head, a CCD controller, a shutter, commercial shutter control unit and a commercial temperature controller. The detector E2V CCD44-

82 is a high performance back illuminated CCD with a 15µm square pixel, image area of 30.7x61.4mm and a high quantum efficiency (QE = 90% at 500nm). The detector controller will be ESO's NGC system to comply with ESO's standard and to reduce compatibility failure with ESO's hardware and software systems. Table 24 is a summary of the detector system characteristics. For further information about UV-VIS detector, see RD7.

Detector	CCD44-82
Chip type	Thinned back illuminated
Pixel size	15 µm
Area	2048 x 4096 pixels, 30.7 x 61.4 mm
QE at 500 nm	90%
Coating	yes
Flatness	Better than 20 µm peak to valley
Peak signal	200 K e^-/pixel
Charge transfer efficiency	99.9995 %
Read-out modes	Low noise (50-100 kpix/sec, TBC) Fast (600 kpix/sec, TBC) Binning: 1x1, 1x2, 2x2
Gain (e^-/ADU)	Low noise mode: 0.6 ± 0.1 Fast mode: 2 ± 0.2
Detector Read-out Noise (RMS)	Low noise mode: <3 e^- Fast mode: < 8e^-

Table 24: UV-VIS detector main characteristics

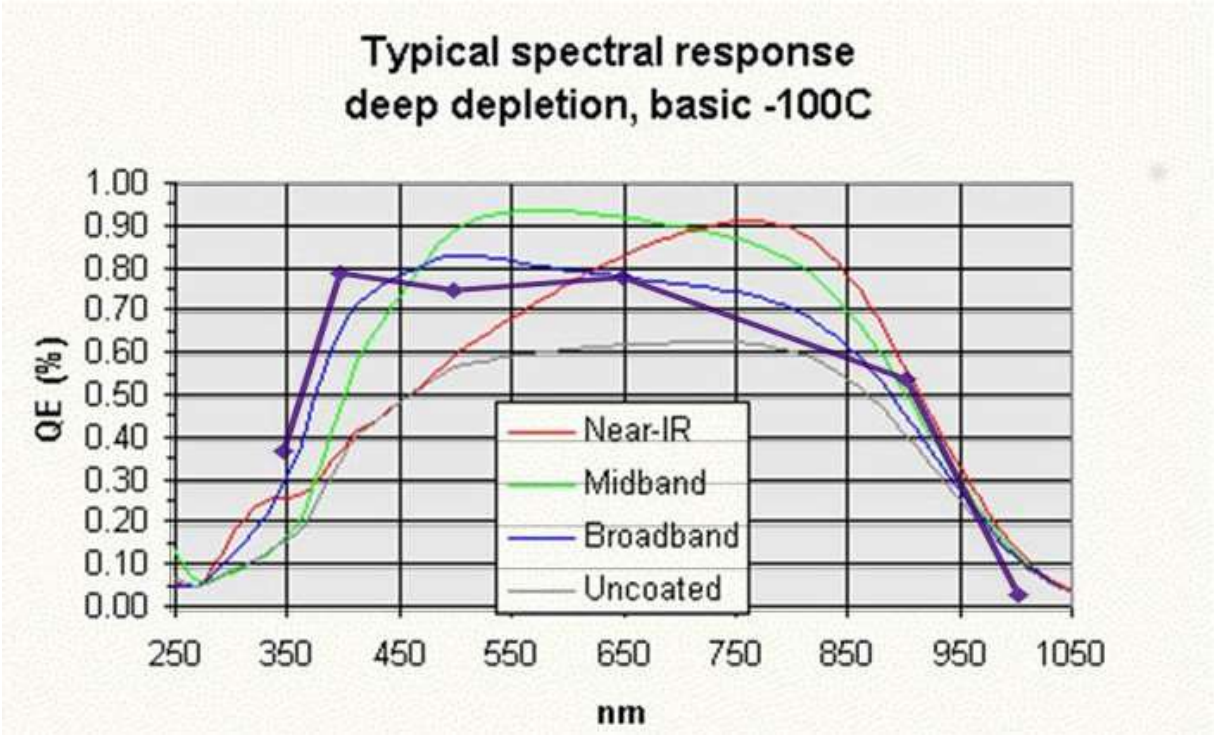

Figure 49: e2v CCD QE

5.3 Optical Quality and Performances

The plate scale on the detector is 53 µm/arcsec or 0.28 arcsec/pixel. To ensure that the instrument is

seeing limited (typical seeing is 0.7''-1'' at the telescope site), we required 80% enslitted energy diameter of 0.4 arcsec, which allows for more than a factor of two degradation due to manufacturing errors while remaining seeing limited. In Figure 53 we show the 80% enslitted energy diameter as a function of wavelength. Figure 53 shows that the requirement has been met, except a small departure in u-band and in the overlap regions. For the red end each quasi-order is high resolution, therefore a degradation of the image quality will not reduce the resolution below the requirement for that wavelength range.

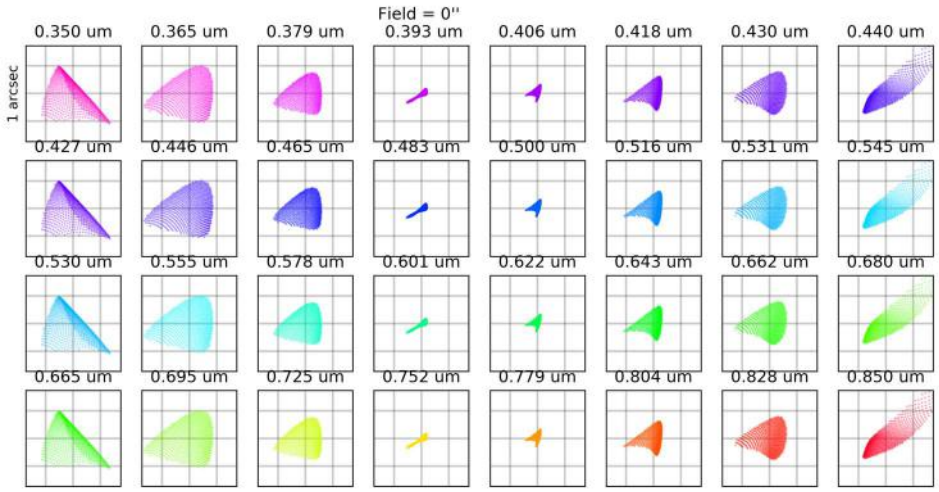

Figure 50: Spot diagram for a field set at the center of the slit. 1x1 arcsec boxes are shown, with the grid representing the pixels (15x15µm). The wavelength for each spot is written above each box.

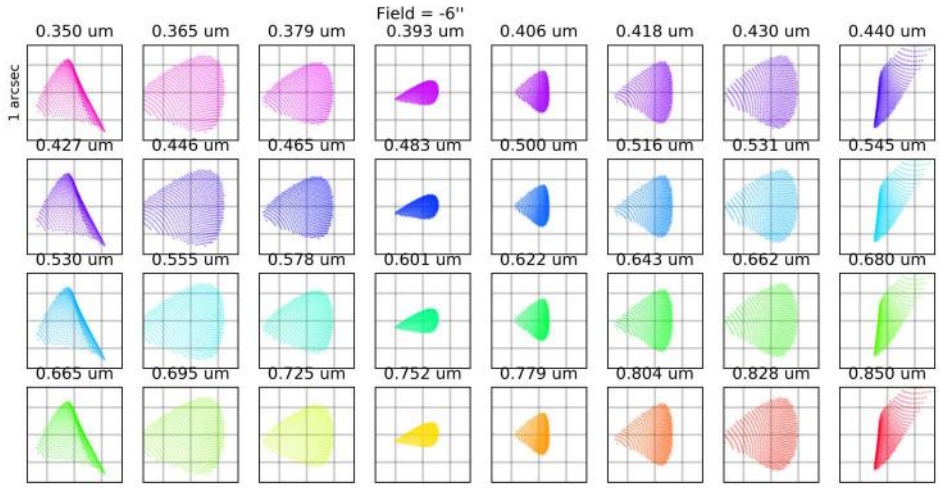

Figure 51: Spot diagram for a field set at the -6 arcsec edge of the slit. 1x1 arcsec boxes are shown, with the grid representing the pixels (15x15µm). The wavelength for each spot is written above each box.

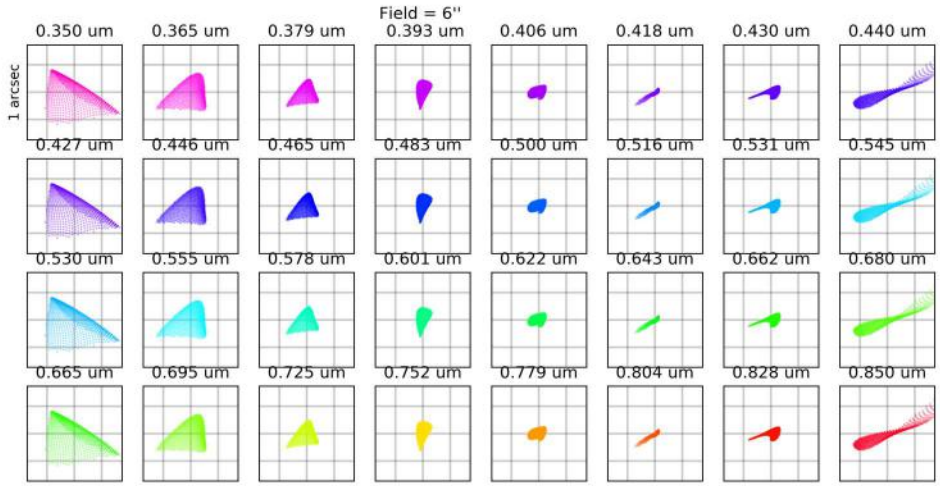

Figure 52: Spot diagram for a field set at the +6 arcsec edge of the slit. 1x1 arcsec boxes are shown, with the grid representing the pixels (15x15µm). The wavelength for each spot is written above each box.

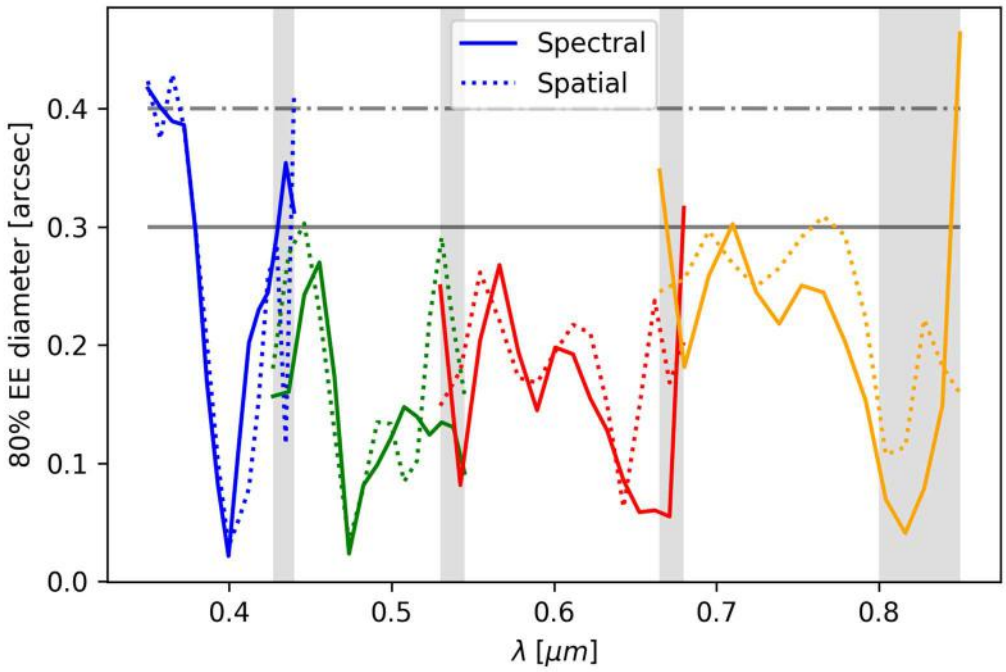

Figure 53: 80% enslitted energy diameter as a function of wavelength in both the spectral (solid) and spatial (dashed) directions.

5.3.1 Spectral Format and Overlap

The spectral format is shown in Figure 54. The margin of each quasi-order from the detectors edge is given in Table 25. The current overlap between quasi-orders is 13-25 nm, also the final overlap is

determined by the finite step width in each dichroic surface. The overlap for each band down to the detector edge is given in the last two columns of Table 25, as can be seen there is a large margin (>0.5 mm) from the edge of the detector. The quasi-orders are similarly separated from each other with distances of ~2 mm.

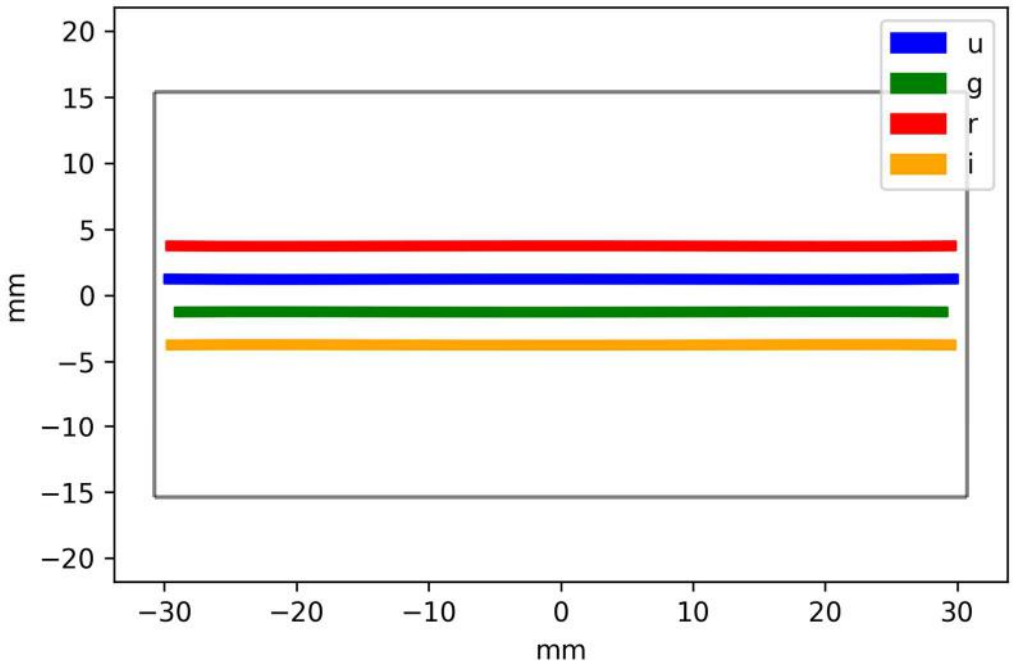

Figure 54: Spectral Format. The black rectangle represents the actual size of the CCD.

	Bottom margin		Top margin		Overlap
	mm	pixels	mm	pixels	
u	0.719	48	0.72	48	u to g: 13 nm (427-440)
g	1.51	101	1.511	101	g to r: 23 nm (522-545)
r	0.867	58	0.868	58	r to i: 24 nm (656-680)
i	0.901	60	0.902	60	i to NIR: 50 nm (800-850)

Table 25: Margins and spectral overlap.

5.4 Throughput

The main advantage of our modular design is the high efficiency gratings. In the following section we give an estimate of the system throughput from the slit down to the detector. We assume 98% contingency for each element/sub-system, see **Table 26**.

The throughput of the ordered ion-etched gratings has been simulated by Franhofer and is shown in **Figure 55**. The gratings have an average efficiency of >85%. Including contingency we expect a throughput of the grating above >80%. The camera is comprised of CaF2 and fused silica, which suffer no bulk absorption, and will only suffer losses due to air-glass interfaces.

Quasi-order		u	g	r	i
Fold Mirror	Expected	0.985	0.985	0.985	0.985
	w/ contingency	0.965	0.965	0.965	0.965
OAP	Expected	0.985	0.985	0.985	0.985
	w/ contingency	0.965	0.965	0.965	0.965
First Dochroic	Expected	0.984	0.984	0.991	0.991
	w/ contingency	0.964	0.964	0.971	0.971
Fold Mirror (u+g)	Expected	0.990	0.990	1.000	1.000
	w/ contingency	0.970	0.970	0.980	0.980
Second dichroic	Expected	0.984	0.984	0.991	0.991
	w/ contingency	0.964	0.964	0.971	0.971
Disperser	Air-glass interfaces	0.990	0.990	0.990	0.990
	Grating efficiency	0.864	0.884	0.880	0.877
	w/ contingency	0.838	0.858	0.854	0.851
Camera		0.920	0.920	0.920	0.920
UV-VIS Spectrograph	Total	0.732	0.749	0.764	0.761
	w/ contingency	0.648	0.663	0.677	0.674
Common Path		0.820	0.820	0.820	0.820
Telescope		0.510	0.510	0.510	0.510
Overall	Total	0.316	0.322	0.316	0.314
	w/ contingency	0.274	0.279	0.274	0.272

Table 26: Throughput estimates.

u

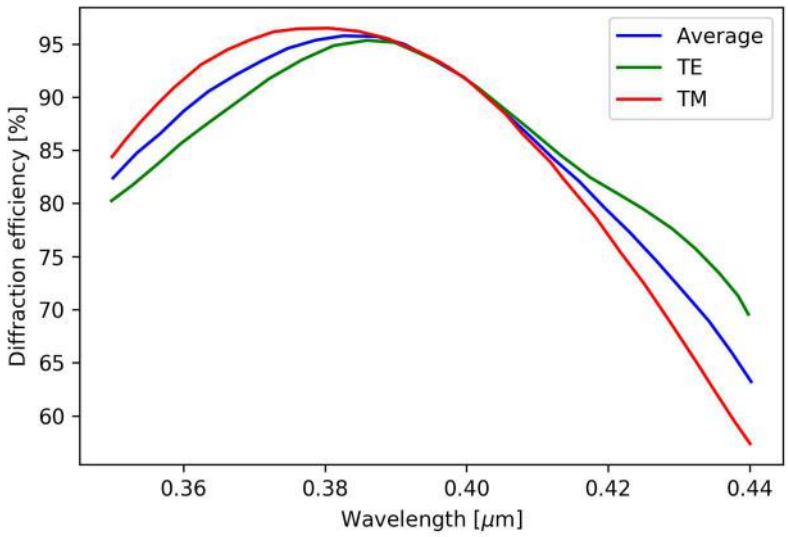

g

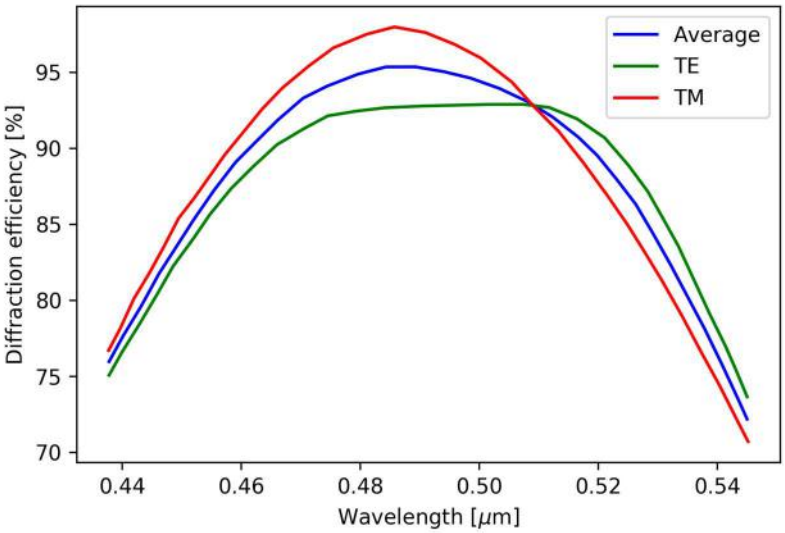
Average
TE
TM
Diffraction efficiency [%]
95
90
85
80
75
70
0.44
0.46
0.48
0.50
0.52
0.54
Wavelength [μm]

r

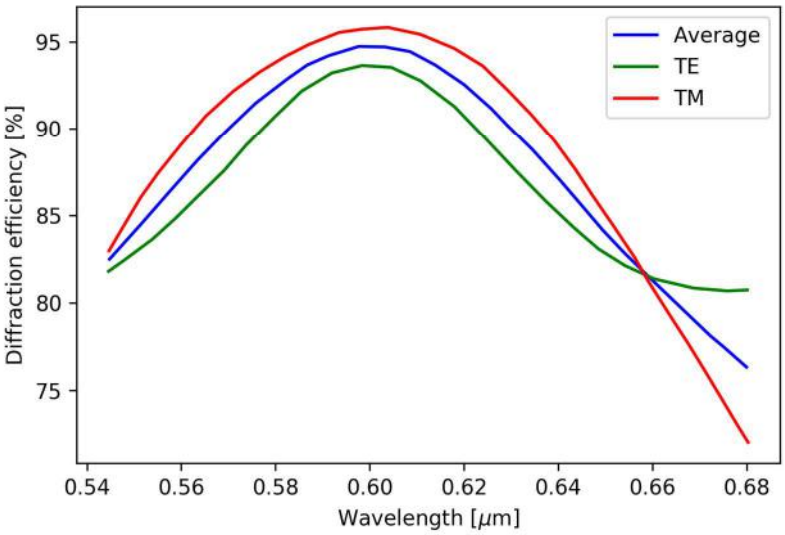
Average
TE
TM
Diffraction efficiency [%]
95
90
85
80
75
0.54
0.56
0.58
0.60
0.62
0.64
0.66
0.68
Wavelength [μm]

i

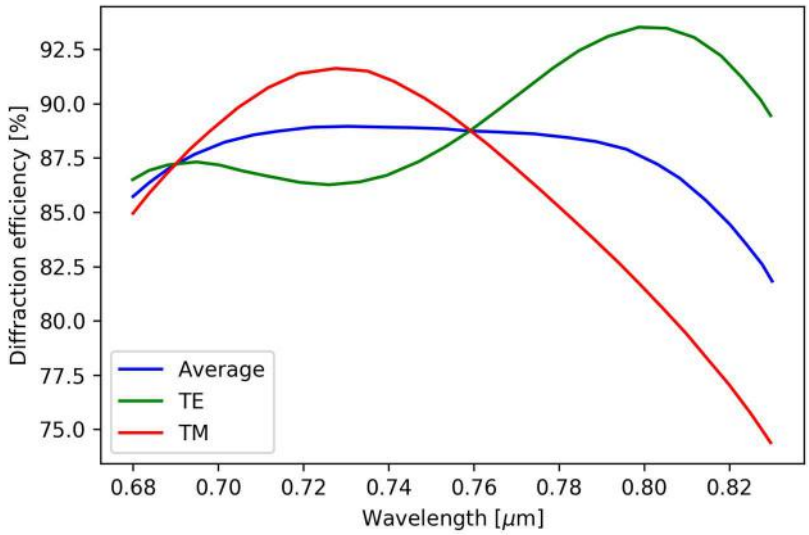

Figure 55: Ion etched grating efficiencies calculated by the vendor. From top to bottom: u, g, r, i. TE and TM are the two polarization modes.

5.5 Sensitivity and Tolerance Analysis

The system is extremely short, therefore thermal effects (Sec. 5.5.3) do not have an effect on the focus. We will use shims to adjust the position of the field flattener relative to the aspheric mirror. Due to the low sensitivity of the system, no active focus will be used.

5.5.1 Manufacturing and alignment tolerance analysis

We performed a tolerance and sensitivity analysis. We used the tolerances given in Table 27 which were chosen after consultation with Winlight. We found that these tolerances were sufficient, requiring mounting decenter and tilt precision of ±50μm/0.1°. These mounting tolerances are well within our mechanical workshop limitations. For the optical elements themselves we require 0.1% tolerance on the radii and 50 μm tolerance on the central thicknesses.

Our sensitivity analysis showed that the worst offenders are the tilt and decenter of the aspheric elements. We set the distance between the field flattener and the aspheric mirror to be a compensator. The compensator range was +/- 300 μm. The compensator statistics are given in **Table 28**. The resulting performance is shown in Figure 56.

Wedge	**0.05 mm**
Element tilt/decenter	**0.1 deg/mm**
Index (abbe)	**0.001 (1%)**
Radius	**0.1%**
Thickness	**0.05 mm**
Surface decenter	**0.125 mm**
Irregularity on aspheres (TEZI)	**+/- 0.5 µm**

Table 27: Tolerance Analysis Parameters.

	Deviation [mm]
Minimum	-0.311026
Maximum	0.305836
Mean	0.006117
Standard Deviation	0.135681

Table 28: Compensator statistics for 100 realizations of the camera: the compensator is the distance (in mm) between the field flattener and the aspheric mirror.

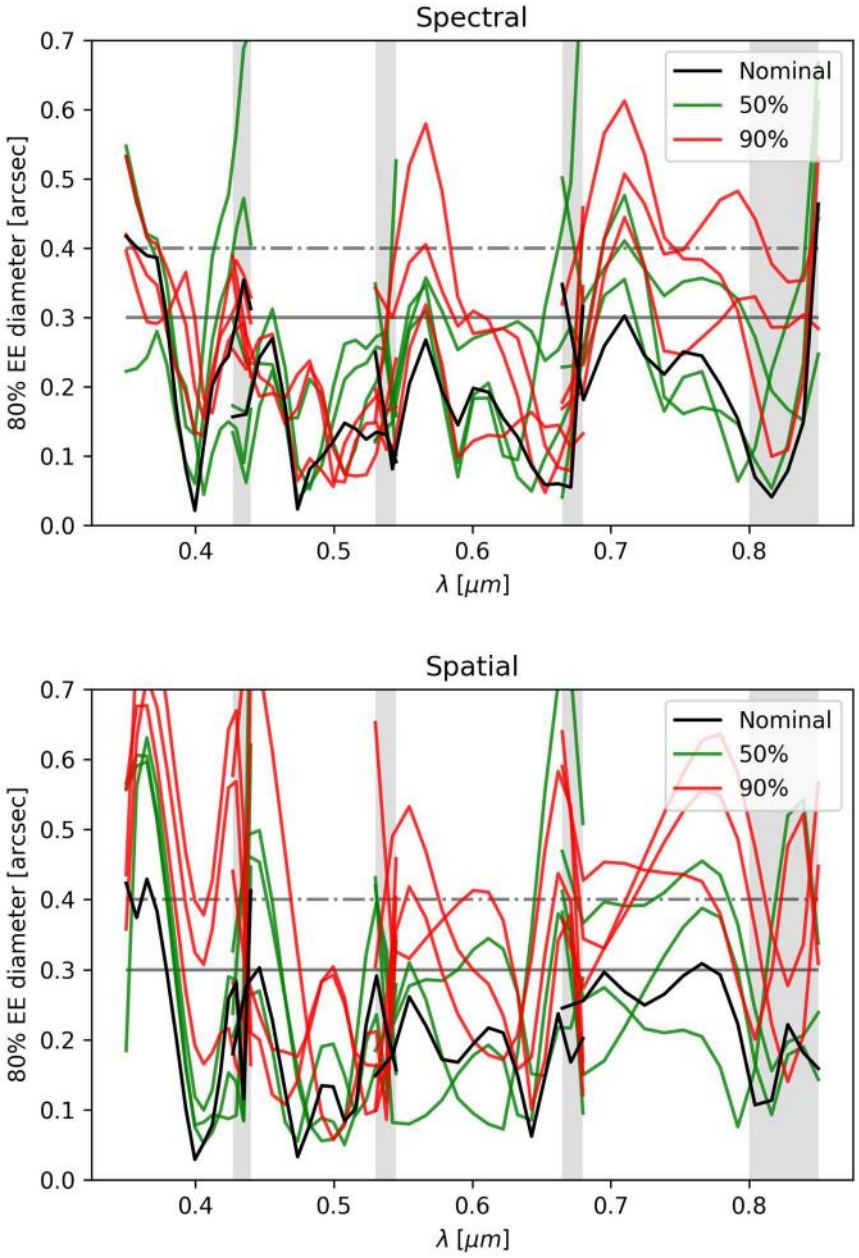

Figure 56: 80% enslitted energy diameter in the spectral (top) and spatial (bottom) directions for the Monte Carlo simulations. We show the nominal system (black), three systems around the median (green), and three systems around the 90th percentile (red).

5.5.2 Feed sensitivity and tolerance analysis

We perform a 200 sample Monte Carlo analysis assuming +/- 20 µm error in distances between elements and +/- 0.02 deg. Because the beam is collimated through all of the dichroic mirrors and the gratings, the main effect of mounting errors is a shift of the spectrum on the detector. Figure 57 shows the image quality of the worst 5% of the systems, and Figure 58 shows the position of the spectrum on the detector for 20 random realizations.

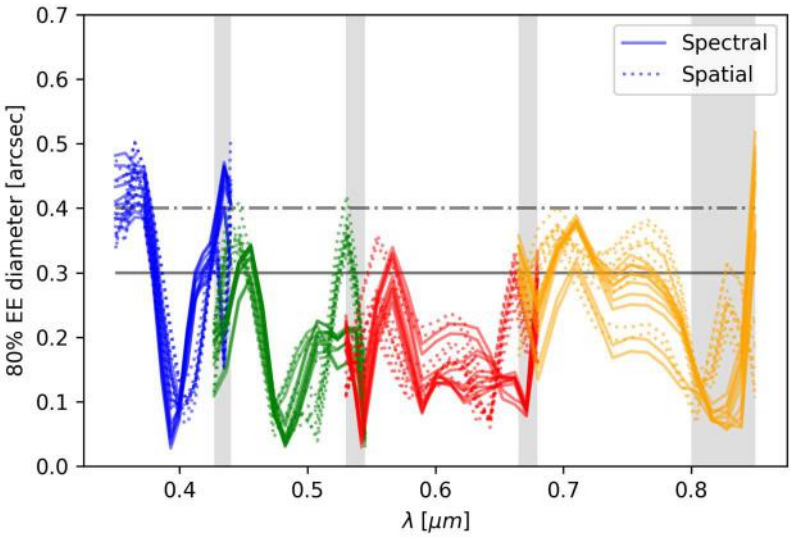

Figure 57: Image quality of the worst 5% of the realizations of the feed.

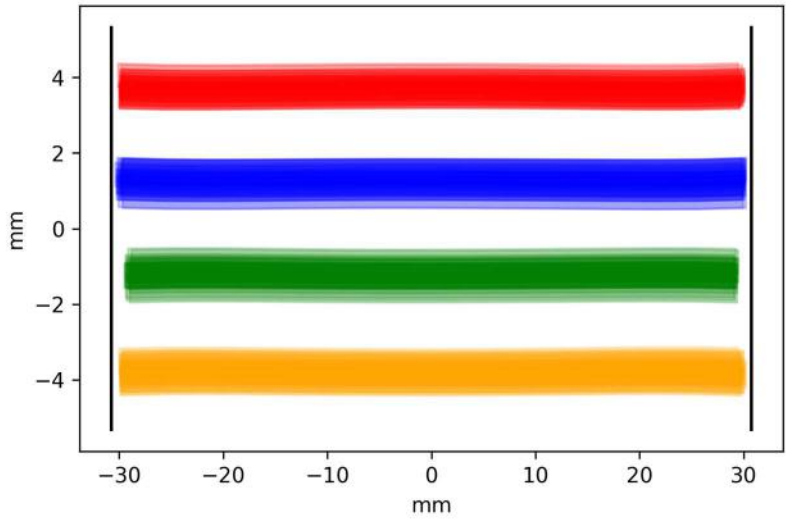

Figure 58: Position of the spectrum on the detector for 20 random realizations of the feed.

5.5.3 Thermal analysis

We performed a thermal analysis exploring three temperature values $(-5, 10, 25℃)$ with a nominal temperature set to $10℃$. The distance between the three camera lenses is maintained by invar with a CTE of 1.5 ppm/C. The distance between the pickup mirror and the OAP is also maintained by invar. The remaining distances are maintained by AL6061 with a CTE of 23.6 ppm/C

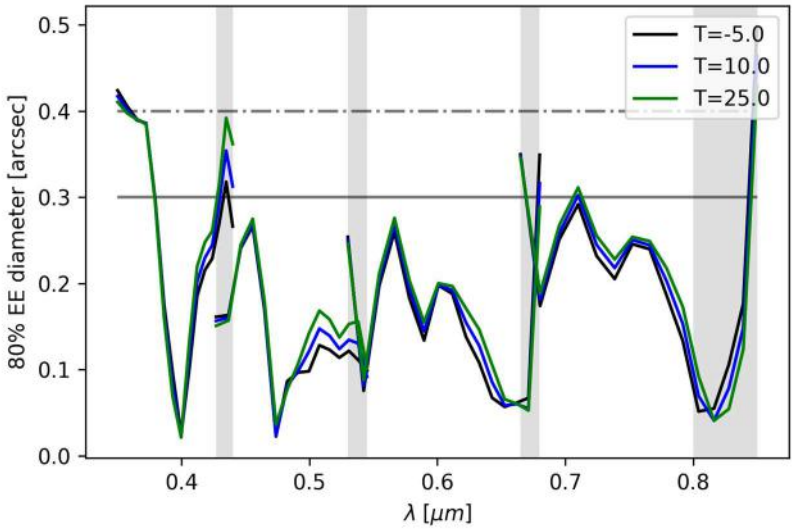

Figure 59: Effect of a 30C temperature change (-5 to 25C) without any compensation.

5.5.4 Ghost analysis

We identify four potential ghosts that can appear in the system:

- Internal reflection within the corrector
- Reflection from the planar surface of the field flattener re-reflected by the front
- Reflection from the detector which is back reflected by the front of the field flattener
- Reflection from the detector which is back reflected by the back of the field flattener

For each of the ghosts we construct a sequential model that simulates the effect and trace rays for three wavelengths (short, central, long) for each quasi-order. The ghosts are shown in Figure 60. From the figure it is clear that only reflection from the detector back from the planar surface of the field flattened overlaps with the trace. However this reflection is diffuse with a spot diameter of ~ 5 mm, therefore there is a 1/300 attenutation due to focus, in addition to a 90% attenuation from the detector and a 98% attenutation from the field flattener AR coating. The relative intensity of this ghost is $\frac{1}{300} \times 0.1 \times 0.02 = 6 \times 10^{-6}$. We conclude this ghost poses no risk.

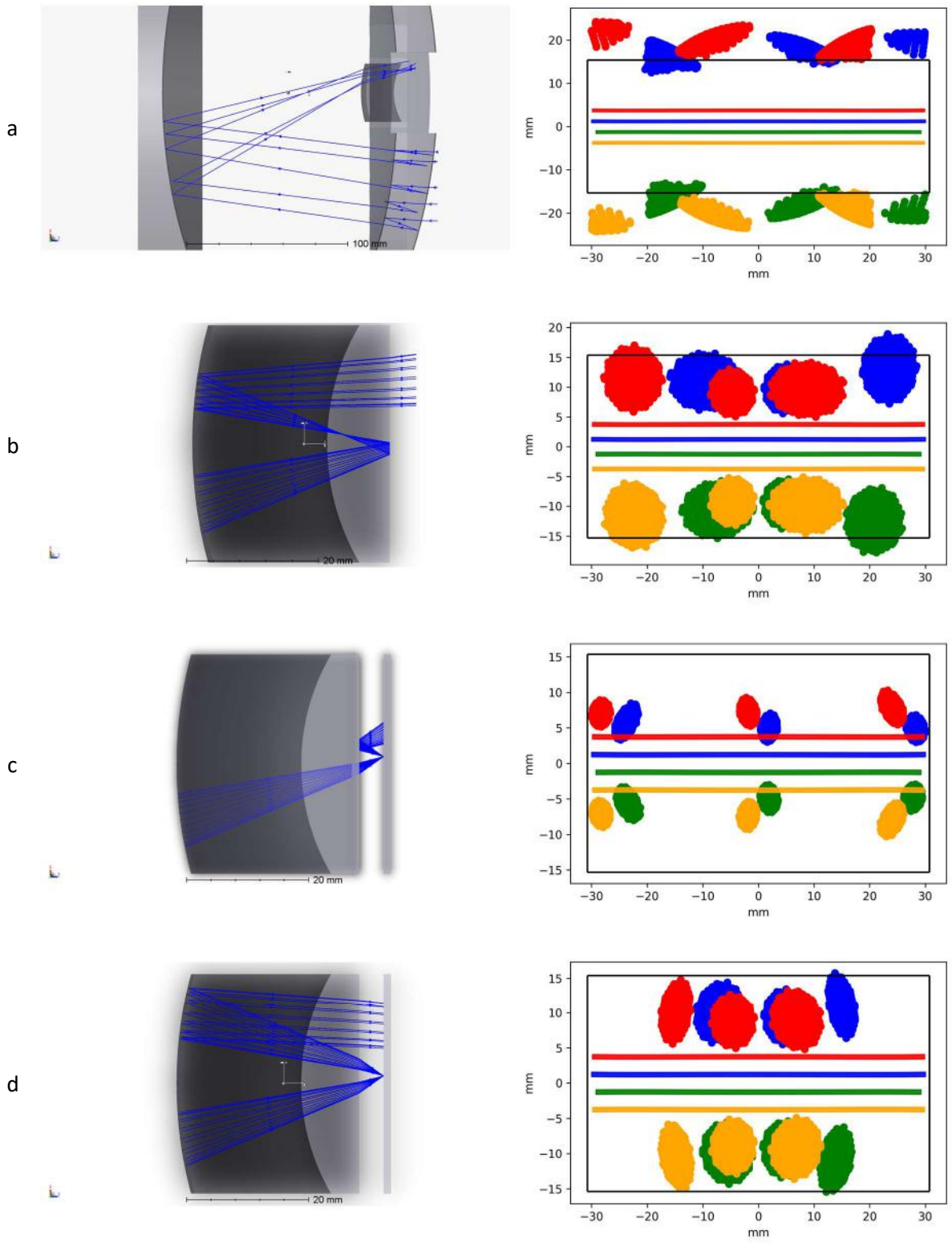

Figure 60: Potential ghosts in the UV-VIS arm.

5.5.4.1 Spectral leakage and 2nd order diffraction

Any spectral leakage from the dichroics will arrive at the gratings at the designed AoI. Therefore for m=1 they will be imaged off of the detector and pose no risk. The only residual risk is from u-band light leaking to the i-band grating and being diffracted at 2nd order (m=2). The i-band grating sits behind two dichroics leading to a 1%^2 (max 5%^2 at specific spikes).
A further suppression of order 10%-20% would be due to optimization of the grating for 1st as opposed to 2nd order. A simulation from the manufacturer showing the i-band 2nd order efficiency is shown in Figure 61. In the unlikely event that there is still unacceptable stray light from m=2, it is possible to insert an order blocking filter before the i-band mirror.

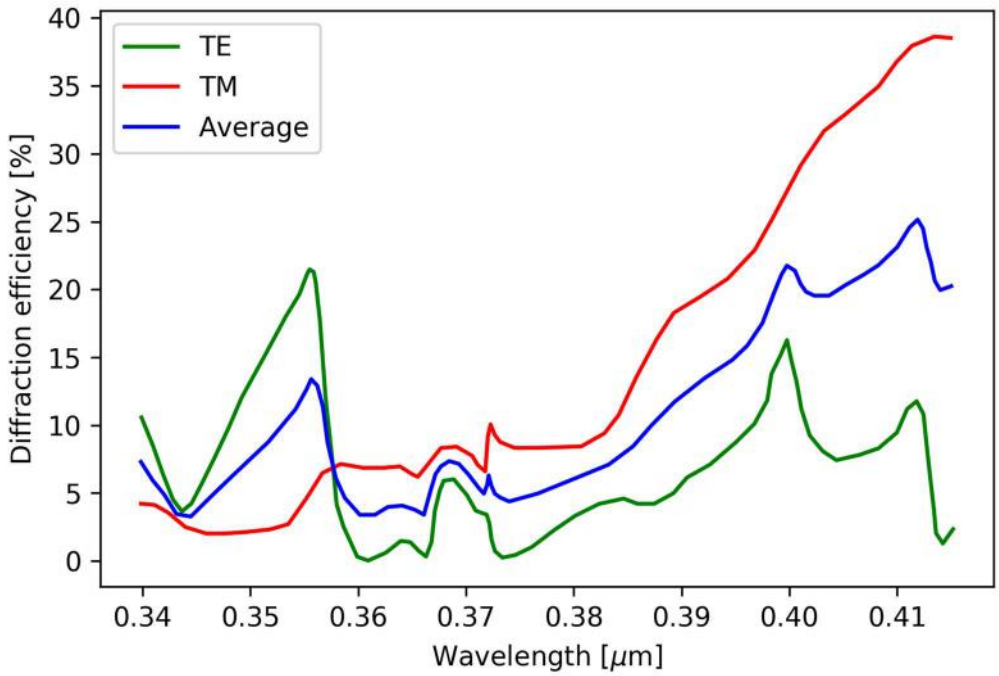

Figure 61 i-band grating 2nd order efficiency to u-band light. In the relevant wavelength range the efficiency is <20%; TE and TM are the two polarization modes.

6 NIR Spectrograph

6.1 Overall Description

The SOXS NIR spectrograph is a near infrared echelle spectrograph, with R=5000 (for 1 arcsec slit), covering a wavelength range from 800 to 2000nm with 15 orders.

6.1.1 Optical layout and first orders parameters

Based on the 4C layout (see [RD2]), the NIR spectrograph is composed of a double pass collimator and a refractive camera, a disperser (grating) and a cross disperser. The design is depicted in Figure 62, and the main parameters are summarized in Table 29.

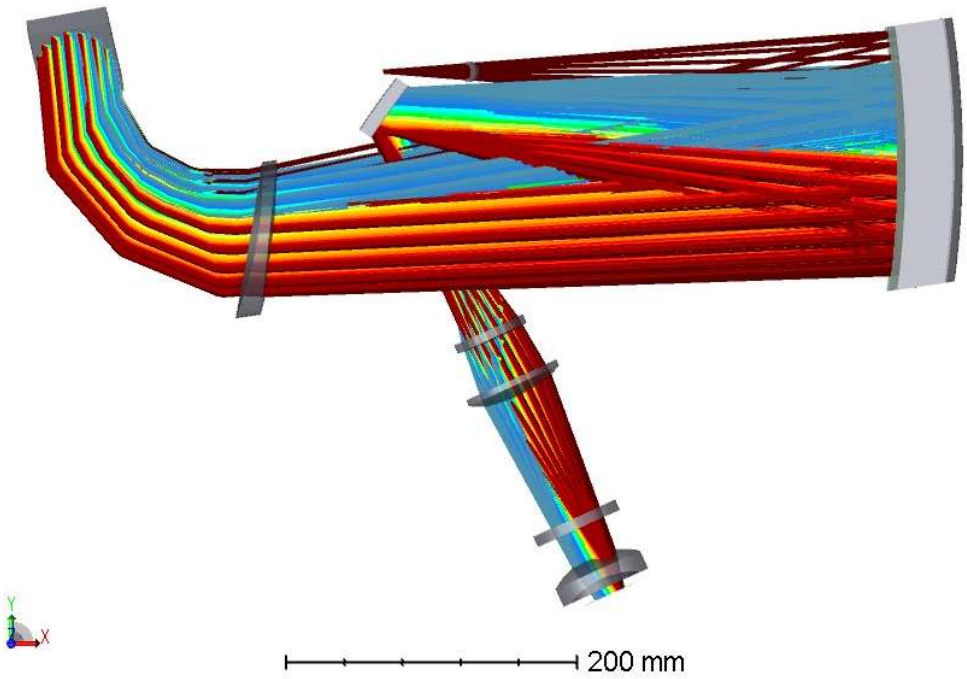

Figure 62: SOXS-NIR Spectrograph Layout.

Collimator Focal Ratio	6.5
Collimator Beam diameter	50mm
Spectral range	800-2000 nm
Resolution (1 arcsec slit)	5000
Foreseen slits	0.5 - 1.0 - 1.5 - 5 arcsec
Silt height	12 arcsec
Camera Output Focal Ratio	~3.7
Detector	2K x2K , 18 µm side pixel
Detector Scale	1arcsec/4pixel
Main Disperser	Grating 44° blaze angle, 4° off-plane
Cross Disperser	3 Cleartran Prisms of apex angle 20°, 20°, 26°
Total Volume (optical surfaces)	~700 x450 x200 mm
Working temperature	150K. 40K for the last two elements of the camera and detector

Table 29: NIR Spectrograph main parameters.

As it can be seen in the Table 29, the wavelength range was extended to 2 µm with an extra order with respect to the PDR design as discussed in [RD5]. This required changing the working temperature from 180K to 150K and other minor changes.

6.1.2 Index of refraction

Cryogenic refractive index measurements are necessary since the SOXS NIR spectrograph works at 40K and 150K. At these low temperatures, it is not guaranteed that the implemented glasses in Zemax are reliable and therefore they need to be verified. We found in the literature measurements for the absolute index of refraction of Cleartran® ZnS [RD3], Infrasil 301 [RD4] and CAF2 [RD5].
Zemax uses a relative index of refraction where the index of refraction of air is exactly 1. Therefore, it was necessary to adapt the absolute index of refraction found in the literature. We proceeded as follows:

- We produce tables of index of refraction for different temperatures and wavelengths using the Sellmeier formula given in the literature.
- We use the Zemax Glass Fitting Tool to fit the tables produced above in order to find the Sellmeier coefficients for the relative index of refraction used by Zemax. The RMS of the fits was of the order of 1e-7, which is better than the typical instrumental error of 1e-6 reported in the reference papers.

We found that better fits with smaller RMS errors were possible when we restricted the temperature range and wavelength range to match our range of interest. We therefore produced glasses that didn't have any temperature dependence since it was not required in the optimization process. In the end, it was seen that using our fitted glasses or the Zemax glasses made little difference.

6.1.3 Optical prescriptions

For each element, we report here the main characteristics, footprint and some notes.

6.1.3.1 Folding Mirror (NIR-FM)

The folding mirror (NIR-FM) is a small mirror placed 60mm after the slit plane, whose aim is to bend by 90° the beam, allowing the accommodation of the spectrograph.

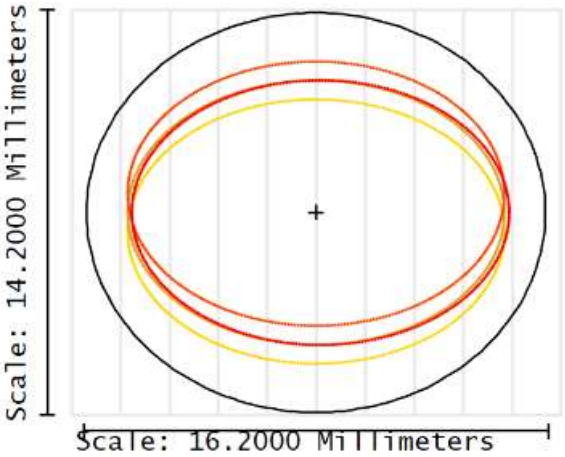

Figure 63: NIR-FM Footprint.

Clear Aperture diameter / size	16 x 14 mm
Radius of curvature	Flat

6.1.3.2 Collimator (NIR-CM and NIR-CL)

The collimator of the system is a Maksutov telescope, used off-axis (and consequently cut). The system has an input f/# of 6.5 (produced by the CP NIR arm) and produces a collimated beam of diameter ~50mm.

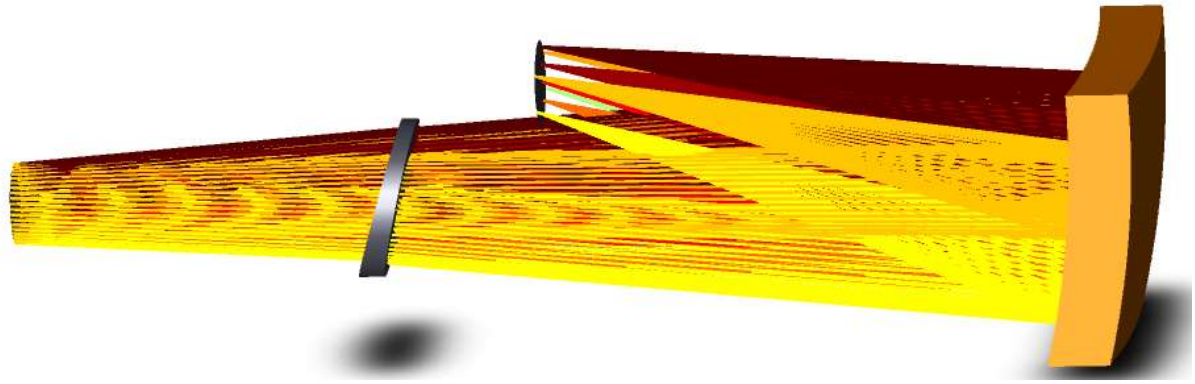

Figure 64: Layout of the collimator.

Table 30 and Table 31 summarize the main parameters of the NIR collimator. Values in Table 31 are for room temperature conditions (P=1 atm, T=20°) and at 0.6328 μm, useful for manufacturing and alignment of the collimator as a standalone system.

Design	Off axis Maksutov
Input F#	6.5
Mirror	
Clear Aperture diameter / size	180 x 168mm
Radius of curvature	640.30mm (concave, spherical)
Corrector lens	
Radii of curvature	322.24 – 258.60mm (convex, concave, spherical)
Clear Aperture diameter / size	104mm
Thickness (of the generating lens center)	10mm

Table 30: Collimator first order parameters.

Surface	Radius of curvature (mm)	Thickness (mm)	Material	Free Diameter (mm)
1 Pupil (decenter 75.222)	-	250.911	Air	50
2 Corrector lens	-258.606	10.000	INFRASIL	104
3	-322.248	434.516	Air	104
4 Main mirror	-642.197	-354.106	Mirror	180 x 180
Defocus	-	0.431		
5 Focal plane	-304.974	-	-	50

Table 31: Collimator Prescription @ T=20°, P=1ATM, wl=0.6328μm.

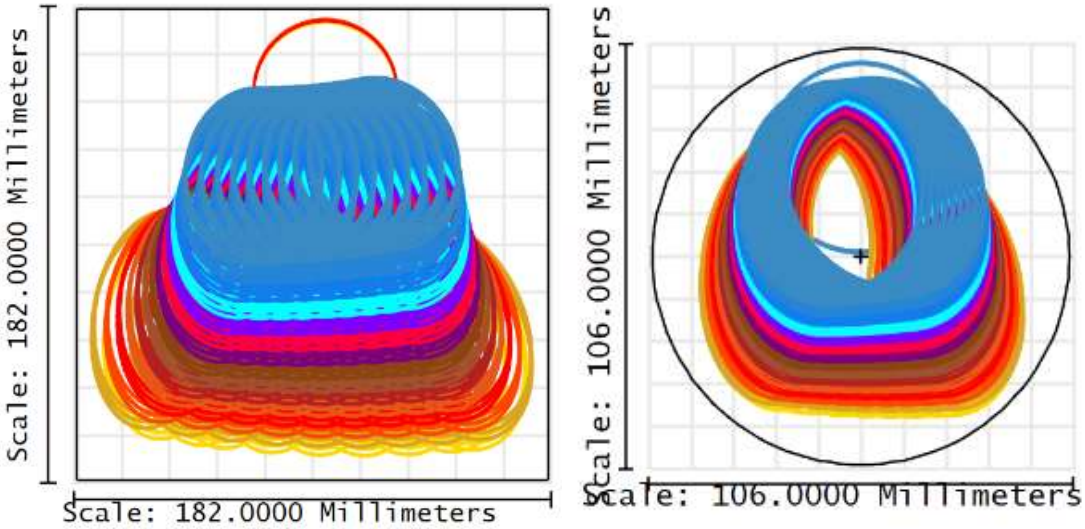

Figure 65: Collimator Mirror and Corrector lens (both surfaces) footprints.

Figure 66 presents the spots on the spherical focal plane for a wavelength of 632.8 at room temperature and 1100nm cryogenic, and it shows that the quality is near diffraction limited for the whole field of view used by the IR spectrograph. Data at 632.8nm are given for manufacturing.

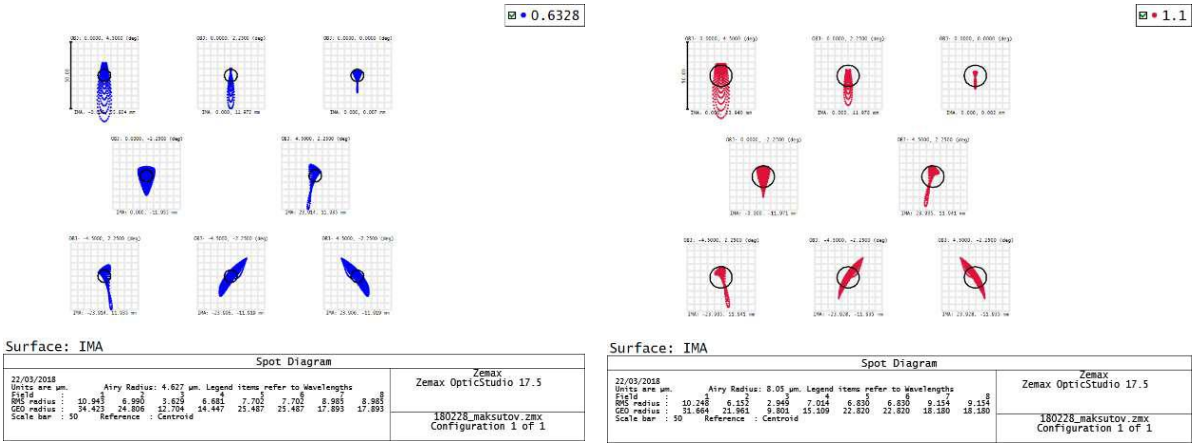

Figure 66: Collimator spot diagrams @ 632.8, room temperature and 1100 nm, cryogenic.

6.1.3.3 Prisms (NIR-P1, NIR-P2, NIR-P3)

Three Cleartran prisms, used in double pass, are the cross-dispersers of the system.

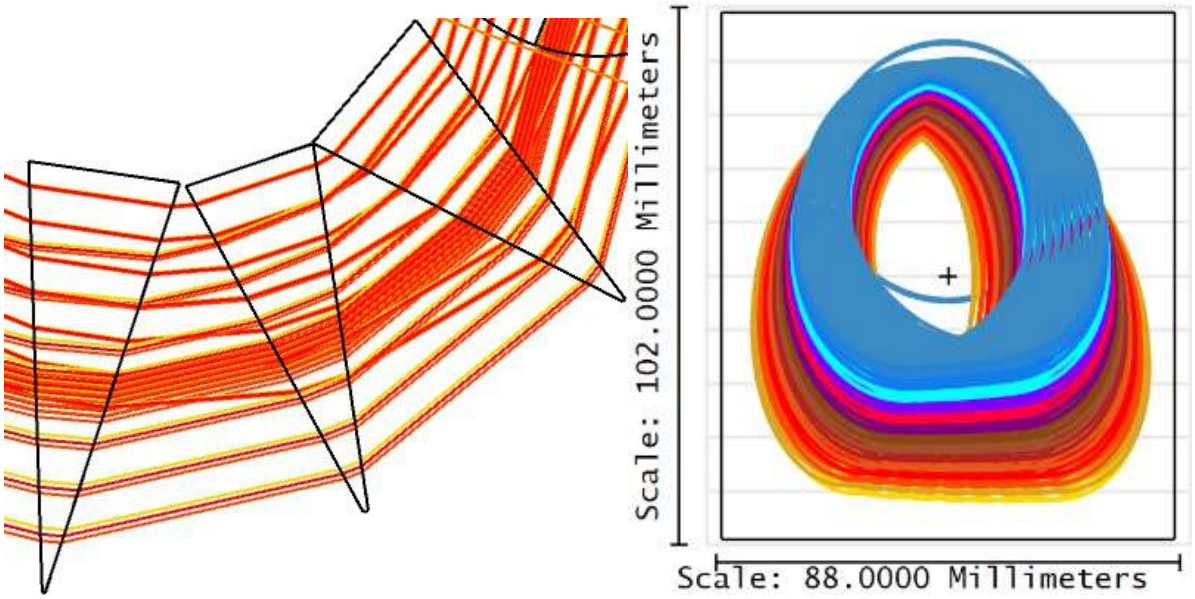

Figure 67: The three prism and the footprint on the first one.

Radii of curvature	Flat
Clear Aperture diameter / size	116 x 77 x 100mm Prism 1: 86.0x100mm, base thickness=35.62mm Prism 2: 73.0x 86mm, base thickness=31.19mm Prism 3: 77.0x 80mm, base thickness=37.18mm
Apex angle	20°,20°,26°
Glass	Cleartran

6.1.3.4 Grating (NIR-G)

The Grating is the main disperser of the system.

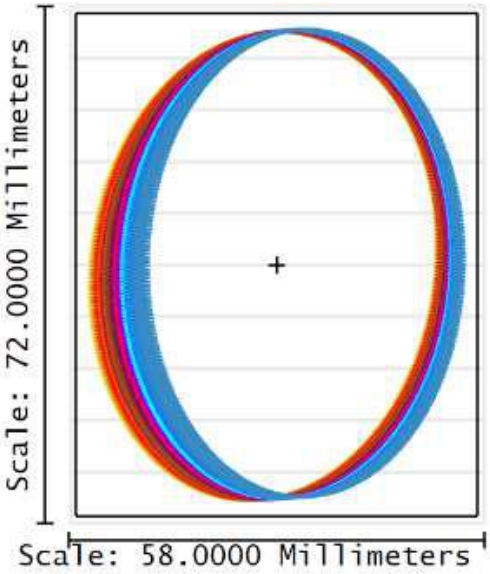

Figure 68: Grating Footprint.

Radii of curvature	Flat
Clear Aperture diameter / size	56x70mm
Lines/mm	72
Blaze angle	44°
Off-plane angle	4°

6.1.3.5 Spherical Fold Mirror (NIR-SM)

The Fold Mirror (NIR-FM) is a spherical mirror, placed after the second pass through the collimator, whose aim is to fold the beam after the dispersion and before the camera, in order to obtain a more compact design. The mirror, placed approximately in the position of the focus of the collimator, creates a pupil, reducing the necessary diameter of the camera lenses.

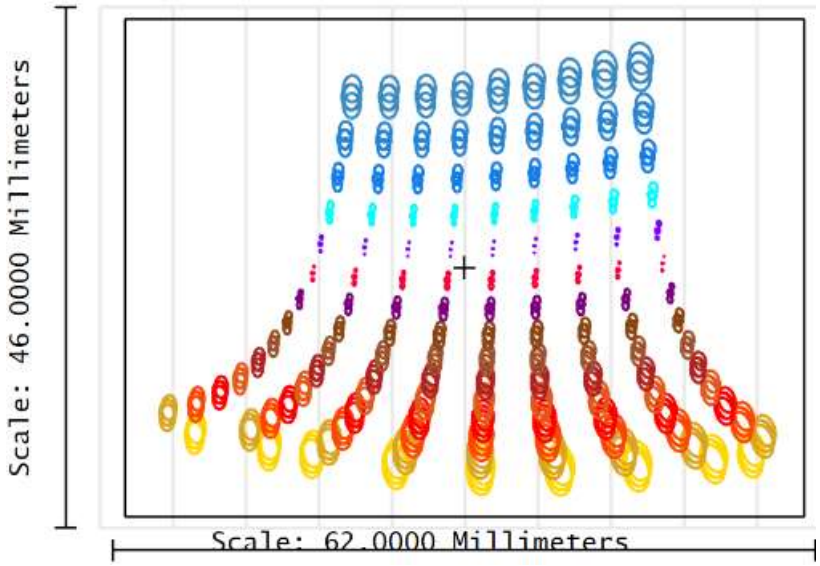

Figure 69: NIR-SM Footprint.

Radius of curvature	-640.0 mm (concave)
Clear Aperture diameter / size	60 x 44 mm

6.1.3.6 Camera

The Camera reimages the focal plane produced by the second pass through the collimator on the detector. It is a completely transmissive system, composed of three single lenses. The camera includes a filter, to cut transmissivity of the system above 2.0 µm, in order to reduce the noise on the detector. The detector itself is slightly tilted to correct for residual chromatic error. Figure 70 shows the camera layout, considered as a stand-alone system; Table 32 describes the Camera surfaces, and Figure 71 presents the spot diagrams for two different wavelengths. The radius of curvature of the object plane was optimized to obtain a flat image surface. All values in the table are given for an environment having T= 20C and P=1atm, to permit manufacturing and alignment at room temperature conditions. Similarly, object plane position is optimized to have the image plane in the nominal position (not the tilt).
The camera has one aspherical surface with a maximum deviation from the best fitting spherical surface of 40µm (see Figure 71).
Nominal data (@ working temperature) of the camera are reported in Table 32.

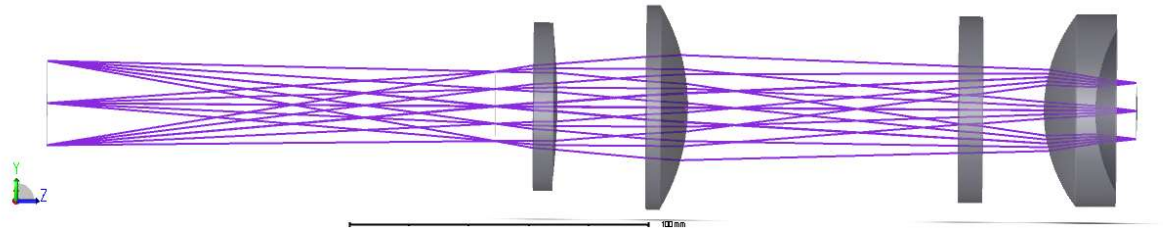

Figure 70: NIR Camera layout.

Surface	Radius of Curvature (mm)	Thickness (mm)	Material	Free Diameter (mm)
0 Object	113.481	150.496	Air	28.0
1 Pupil	-	-150.496	Air	23.08
2	-	157.23	Air	-
3 NIR_L1 S1	Infinity	8.006	Cleartran	52.0
4 NIR_L1 S2	-205.343 Asph: 4^{th}:3.0731e-7 6^{th}:5.739e-11	29.852	Air	52.0
5 NIR_L2 S1	Infinity	13.993	CAF2	68.0
6 NIR_L2 S2	-66.635	90.836	Air	68.0
7 NIR_W S1	Infinity	8.001	Infrasil	62.0
8 NIR_W S2	Infinity	20.484	Air	62.0
9 NIR_L3 S1	52.652	17.280	Cleartran	64.0
10 NIR_L3 S2	55.794	12.0042	Air	54.0
11 Refocus	-	0	Air	-
12 Image	Infinity	-	-	-

Table 32: NIR Camera prescriptions (@632.8nm and T=20C, P=1atm).

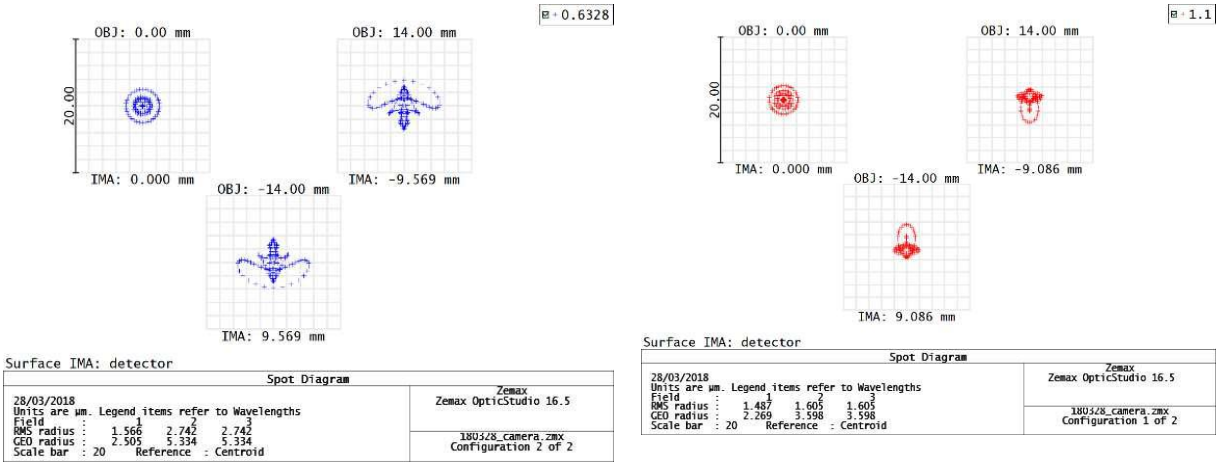

Figure 71: NIR Camera spot diagrams @632.8 (left) and @1100 nm (right).

FIRST LENS (NIR-L1)

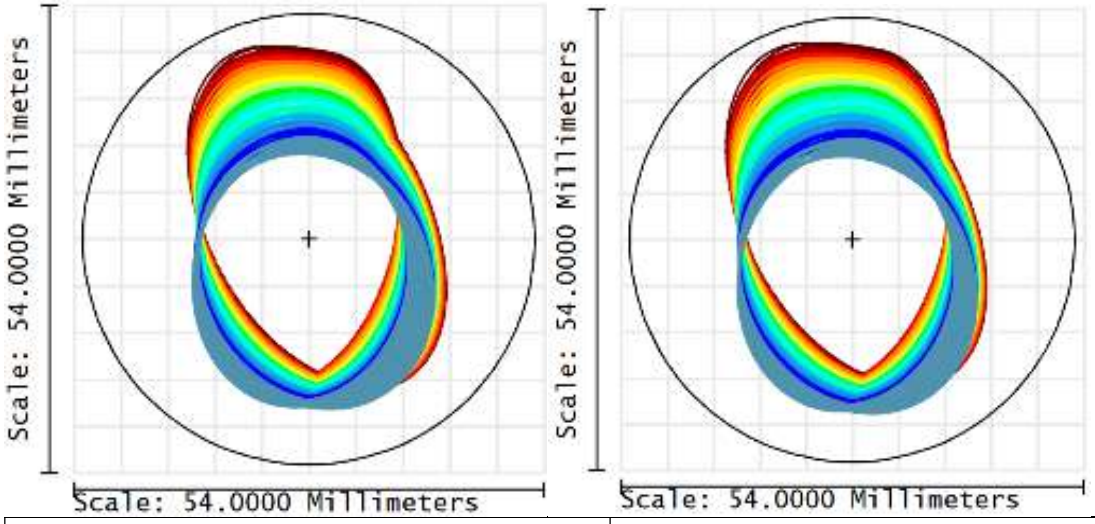

Radii of curvature	Flat, -205.190 mm
Clear Aperture diameter / size	52 mm
Glass	Cleartran
Aspheric shape	On second surface 4th :3.08e-7 6th:5.76e-11
Thickness (center)	8 mm

Figure 72: NIR-L1 Footprints.

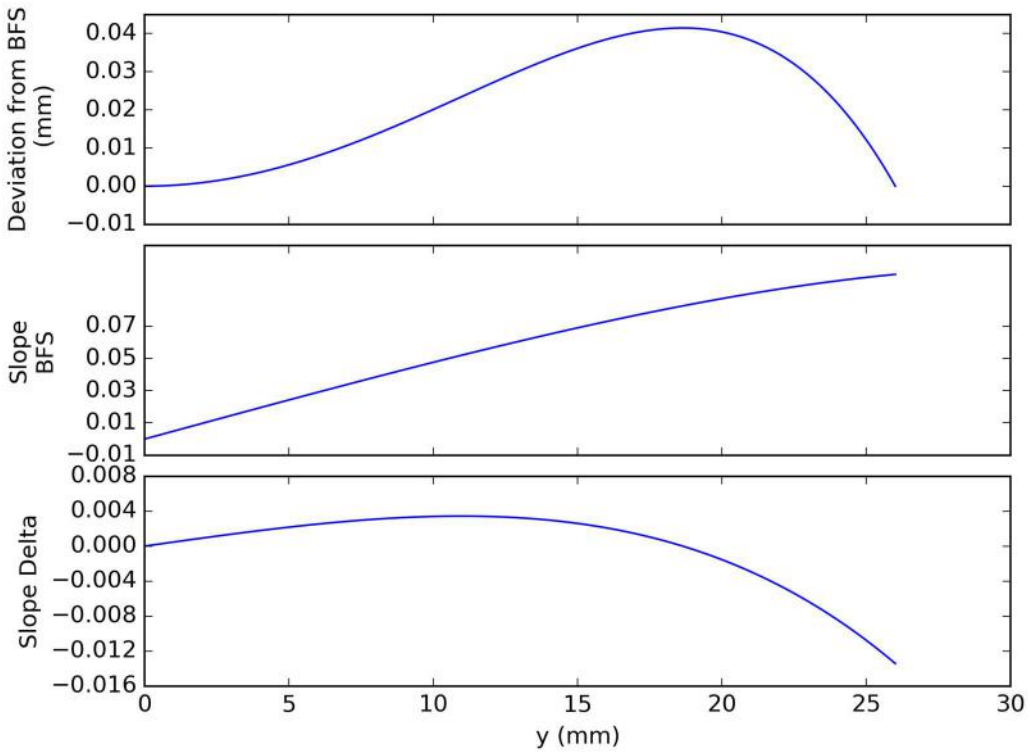

Figure 73: Aspherical surface of NIR-L1 deviation from Best fitting Sphere.

SECOND LENS (NIR-L2).

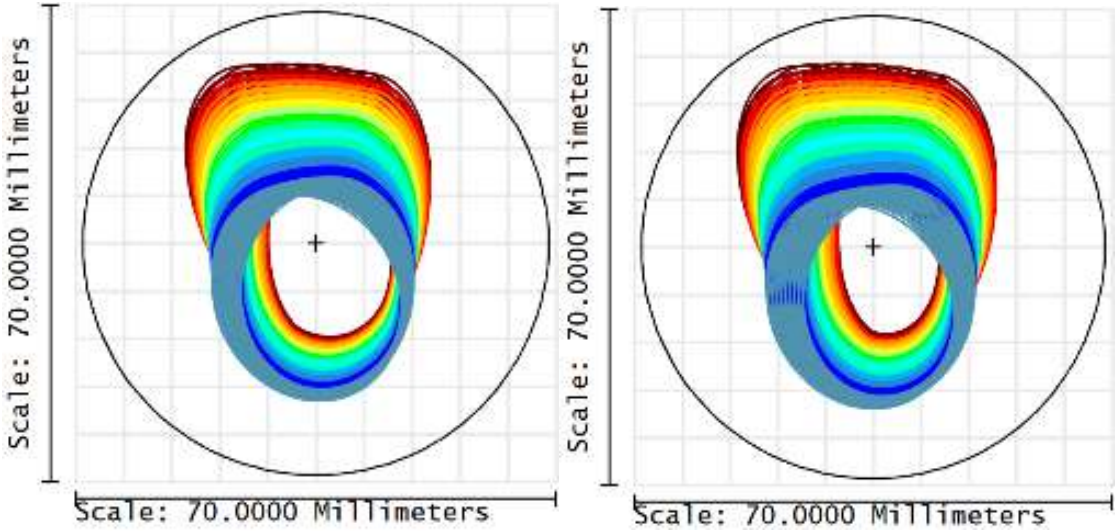

Figure 74: NIR-L2 Footprints.

Radii of curvature	Flat, -66.480 mm
Clear Aperture diameter / size	68 mm
Glass	CAF2
Thickness (center)	13.96 mm

THIRD LENS (NIR-L3)

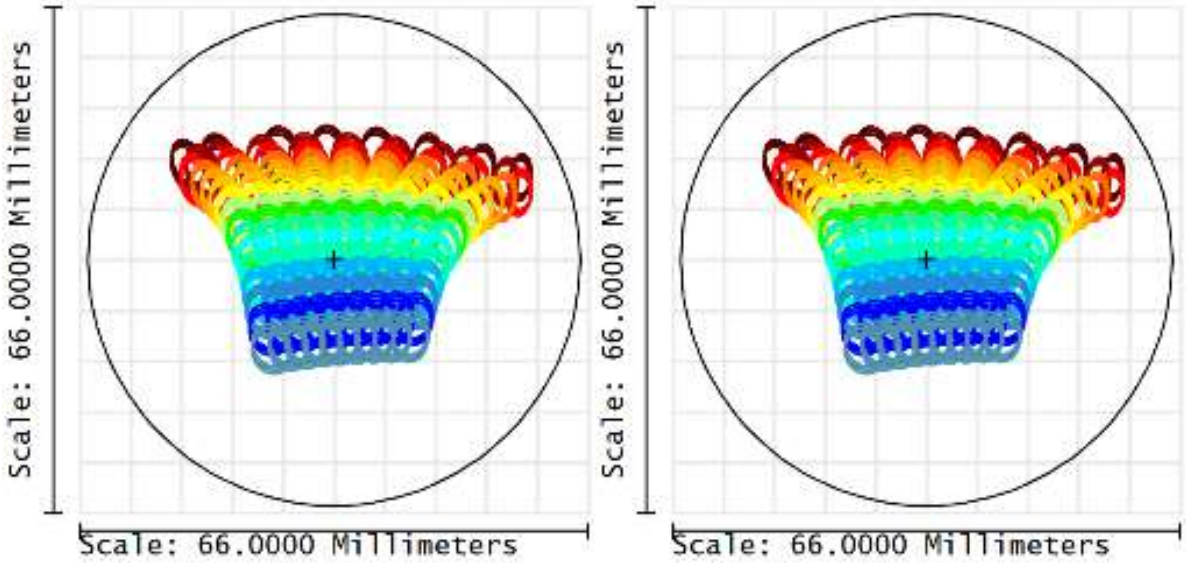

Figure 75: NIR-L3 Footprints.

Radii of curvature	52.620, 55.760 mm
Clear Aperture diameter / size	32, 27 mm
Glass	Cleartran
Thickness (center)	17.27 mm

FILTER (NIR-F)

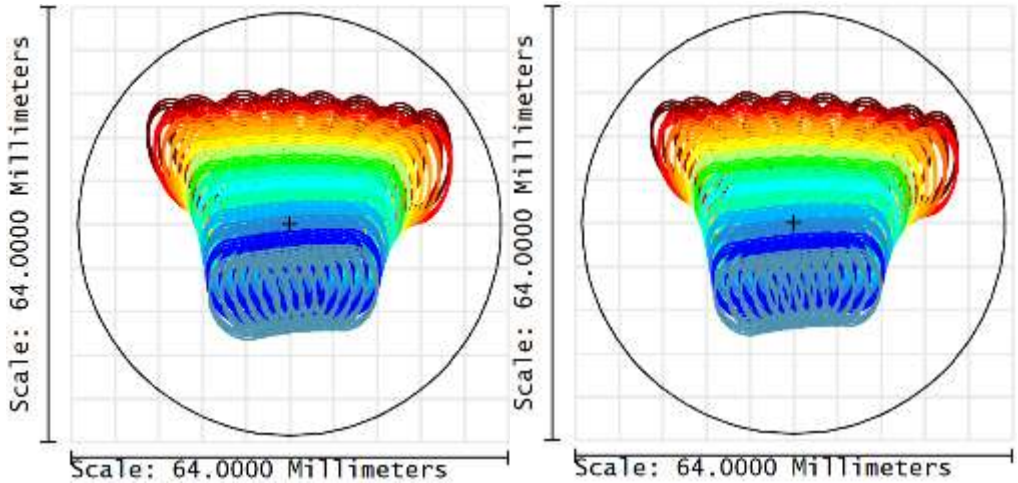

Figure 76 NIR-L3 Footprints.

Radii of curvature	Flat
Clear Aperture diameter / size	62 mm
Glass	Infrasil
Thickness (center)	8 mm

6.1.3.7 Complete optical data

	Radius [mm]	Thickness [mm]	Material	Diameter [mm]	Decenter X [mm]	Decenter Y [mm]	Tilt X [deg]	Tilt Y [deg]	Tilt Z [deg]	Order
0 Object		-22750.000		1.32						
1 Stop		22750.000		3500.00						
2 Slit		60.000		1.32						
3 CB 1		0.000		0.00	0.000	0.000	0.000	-45.000	0.000	0.000
4 NIR-SM		0.000	MIRROR	16.00						
5 CB 2		0.000		0.00	0.000	0.000	0.000	-45.000	0.000	0.000
6		60.000		10.56						
7 CB 3		0.000		0.00	0.000	-24.000	8.211	0.000	0.000	1.000
8		-353.060		49.35						
9 NIR-CM	640.300	433.300	MIRROR	236.00						
10 NIR-CL S1	322.240	10.000	INFRASIL	192.00						
11 NIR-CL S2	258.600	20.000		192.00						
12 CB 4		0.000		0.00	0.000	-54.477	4.379	0.000	0.000	0.000
13 CB 5		0.000		0.00	0.000	0.000	-23.390	0.000	0.000	0.000
14 NIR-P1		0.000	CLEARTRAN	52.10						
15 CB 5		0.000		0.00	0.000	0.000	10.000	0.000	0.000	0.000
16		25.000	CLEARTRAN	51.29						
17 CB 6		0.000		0.00	0.000	0.000	10.000	0.000	0.000	0.000
18		0.000		51.97						
19 CB 7		0.000		0.00	0.000	0.000	-23.390	0.000	0.000	0.000
20		26.000		47.90						
21 CB 8		0.000		0.00	0.000	0.000	-23.390	0.000	0.000	0.000
22 NIR-P2		0.000	CLEARTRAN	51.85						
23 CB 9		0.000		0.00	0.000	0.000	10.000	0.000	0.000	0.000
24		21.000	CLEARTRAN	51.01						
25 CB 10		0.000		0.00	0.000	0.000	10.000	0.000	0.000	0.000
26		0.000		51.48						
27 CB 11		0.000		0.00	0.000	0.000	-23.390	0.000	0.000	0.000
28		29.000		47.65						
29 CB 12		0.000		0.00	0.000	0.000	-30.960	0.000	0.000	0.000
30 NIR-P3		0.000	CLEARTRAN	57.11						
31 CB 13		0.000		0.00	0.000	0.000	13.000	0.000	0.000	0.000
32		23.000	CLEARTRAN	55.49						
33 CB 14		0.000		0.00	0.000	0.000	13.000	0.000	0.000	0.000
34		0.000		57.38						
35 CB 15		0.000		0.00	0.000	0.000	-30.960	0.000	0.000	0.000
36		0.000		50.38						
37		45.000		50.38						
38 CB 16		0.000		0.00	0.000	0.000	0.000	0.000	90.000	0.000
39 CB 17		0.000		0.00	0.000	0.000	-44.000	4.000	0.000	0.000

40 NIR-G		0.000	MIRROR	67.25	0.072	9.000	0.000	0.000	0.000	0.000
41 CB 18		0.000		0.00	0.000	0.000	44.000	-4.000	0.000	-1.000
42 CB 19		0.000		0.00	0.000	0.000	0.000	0.000	-90.000	0.000
43		-45.000		58.64						
44 CB 20		0.000		0.00	0.000	0.000	30.960	0.000	0.000	0.000
45 NIR-P3		0.000	CLEARTRAN	91.41						
46 CB 21		0.000		0.00	0.000	0.000	-13.000	0.000	0.000	0.000
47		-23.000	CLEARTRAN	88.19						
48 CB 22		0.000		0.00	0.000	0.000	-13.000	0.000	0.000	0.000
49		0.000		91.98						
50 CB 23		0.000		0.00	0.000	0.000	30.960	0.000	0.000	0.000
51		-29.000		88.79						
52 CB 24		0.000		0.00	0.000	0.000	23.390	0.000	0.000	0.000
53 NIR-P2		0.000	CLEARTRAN	112.66						
54 CB 25		0.000		0.00	0.000	0.000	-10.000	0.000	0.000	0.000
55		-21.000	CLEARTRAN	110.06						
56 CB 26		0.000		0.00	0.000	0.000	-10.000	0.000	0.000	0.000
57		0.000		113.16						
58 CB 27		0.000		0.00	0.000	0.000	23.390	0.000	0.000	0.000
59		-26.000		112.74						
60 CB 28		0.000		0.00	0.000	0.000	23.390	0.000	0.000	0.000
61 NIR-P1		0.000	CLEARTRAN	138.84						
62 CB 29		0.000		0.00	0.000	0.000	-10.000	0.000	0.000	0.000
63		-25.000	CLEARTRAN	135.65						
64 CB 30		0.000		0.00	0.000	0.000	-10.000	0.000	0.000	0.000
65		0.000		139.33						
66 CB 31		0.000		0.00	0.000	0.000	23.390	0.000	0.000	0.000
67 CB 32		-20.000		0.00	0.000	54.477	-4.379	0.000	0.000	-1.000
68 NIR-CL S2	258.600	-10.000	INFRASIL	192.00						
69 NIR-CL S1	322.240	-433.300		192.00						
70 NIR-CM	640.300	353.060	MIRROR	362.92						
71 CB 33		0.000		0.00	0.000	-3.645	-13.711	0.000	0.000	0.000
72 CB 34		0.000		0.00	0.000	0.000	-30.000	0.000	0.000	0.000
73 NIR-FM	-640.000	0.000	MIRROR	69.62						
74 CB 35		-165.000		0.00	0.000	0.000	-30.000	0.000	0.000	0.000
75		0.000		0.00						
76		0.000		46.77						
77 NIR-L1 S1		-8.000	CLEARTRAN	52.00						
78 NIR-L1 S2	205.190 Ev Aspheric: 4th: -3.08e-7 6th:-5.76e-11	-29.760		52.00						
79 NIR-L2 S1		-13.960	CAF2	68.00						
80 NIR-L2 S2	66.480	-90.540		68.00						

81 NIR-F S1		-8.000	INFRASIL	62.00						
82 NIR-F S2		-20.460		62.00						
83 NIR-L3 S1	-52.620	-17.270	CLEARTRAN	64.00						
84 NIR-L3 S2	-55.760	-12.000		54.00						
85 Detector Tilted		0.000		45.63	X tilt (deg)- 0.006	0.000	0.000	0.000	0.000	0.000

Table 33: NIR arm optical prescription.

6.1.4 Detector System

The HAWAII 2RG is the NIR detector selected to equip the SOXS NIR spectrograph. This array presents a cut off at 2.5 µm and a wide range of spectral response. Thanks to the substrate removal, the detector allows to reach a good QE starting down to 0.6 µm obtaining a good spectral overlap with the UV-VIS CCD.

Parameter	**Parameter**
Detector Material	MBE HgCdTe double layer planar heterostructures (DLPH)
Substrate	CdZnTe substrate, removed after hybridization to minimize fringing and optimize QE
Format	2048x2048
Cut-off wavelength,	l_c=2.5 µm
Pixel size	18.0 µm
Package	GL Scientific Molybdenum base package with 3 point kinematic mount and flex-rigid pcb interface without ASIC for 32 video channels
Connector	HIROSE connector for 32 channels
Number of outputs	32 outputs for science frame access of internal bus outputs
Frame rate	0.76 Hz using 32 parallel outputs
Reset by row	Non-destructive readout possible
Readout noise	Double correlated: < 20 e^- rms 16 Fowler pairs < 7 e^- rms
Storage capacity @ 0.5 V	80 Ke^-
Dark current @ 77 K	< 0.1 e^-/s

Table 34 NIR detector characteristics.

The operative temperature will be 40K to reduce the persistence. The HAWAII 2RG is characterized by good performance in terms of dark, cosmetics and, mainly, persistence. Its main features are reported in the table below.
The adopted electronic controller is the ESO NGC. This system is the new ESO controller for UV-VIS and NIR detectors, it has good performances and guarantees full compatibility with ESO electronics. For more information about the NIR detector, please refer to [RD8].

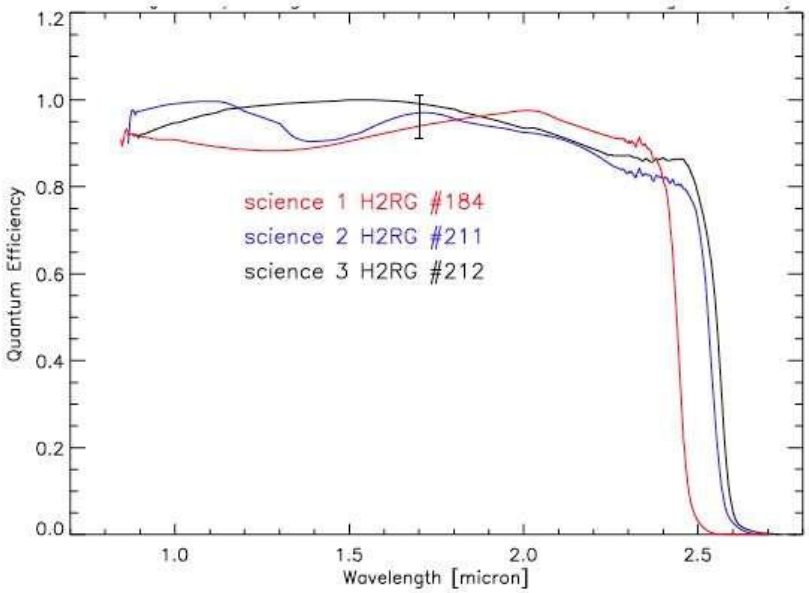

Figure 77 NIR detector quantum efficiency.

6.2 Performances

6.2.1 Orders Data

In Table 35, data of the orders (from 9 to 24) are reported: The blaze wavelength, the Free Spectral Range (FSR) and the extreme wavelengths for each order. Order 9 will be blocked by the filter but it was included in the analysis to check that it does not leak into order 10.

ORDER	FSR (μ)	MIN WL(μ)	BLAZE WL(μ)	MAX WL(μ)
9	0.238	2.025	2.144	2.263
10	0.193	1.833	1.930	2.026
11	0.159	1.674	1.754	1.834
12	0.134	1.541	1.608	1.675
13	0.114	1.427	1.484	1.541
14	0.098	1.329	1.378	1.428
15	0.086	1.244	1.286	1.329
16	0.075	1.168	1.206	1.244
17	0.067	1.102	1.135	1.168
18	0.06	1.042	1.072	1.102
19	0.053	0.989	1.016	1.042
20	0.048	0.941	0.965	0.989
21	0.044	0.897	0.919	0.941
22	0.04	0.857	0.877	0.897
23	0.036	0.821	0.839	0.857
24	0.034	0.787	0.804	0.821

Table 35: Orders data.

6.2.2 Spectral Format and inter-orders gap

The spectral format on the detector has been obtained by raytracing with the Zemax model.
Each order free spectral range was sampled with 41 wavelength points (extremes included). For each wavelength, the coordinates X and Y of the spot centroid on the detector for 3 points along the 1 arcsec (slit center and extremes) have been considered.
In Figure 78, the free spectral range of the 15 orders are reported, showing that the complete spectrum fits inside the 2k x2k detector.
Using the aforementioned X and Y coordinates, free inter-order gaps have been calculated: coordinates have been fitted with quadratic polynomials, and the distance between orders calculated as the difference of the obtained polynomials. Figure 79 shows that gaps are always greater than 10 pixels.

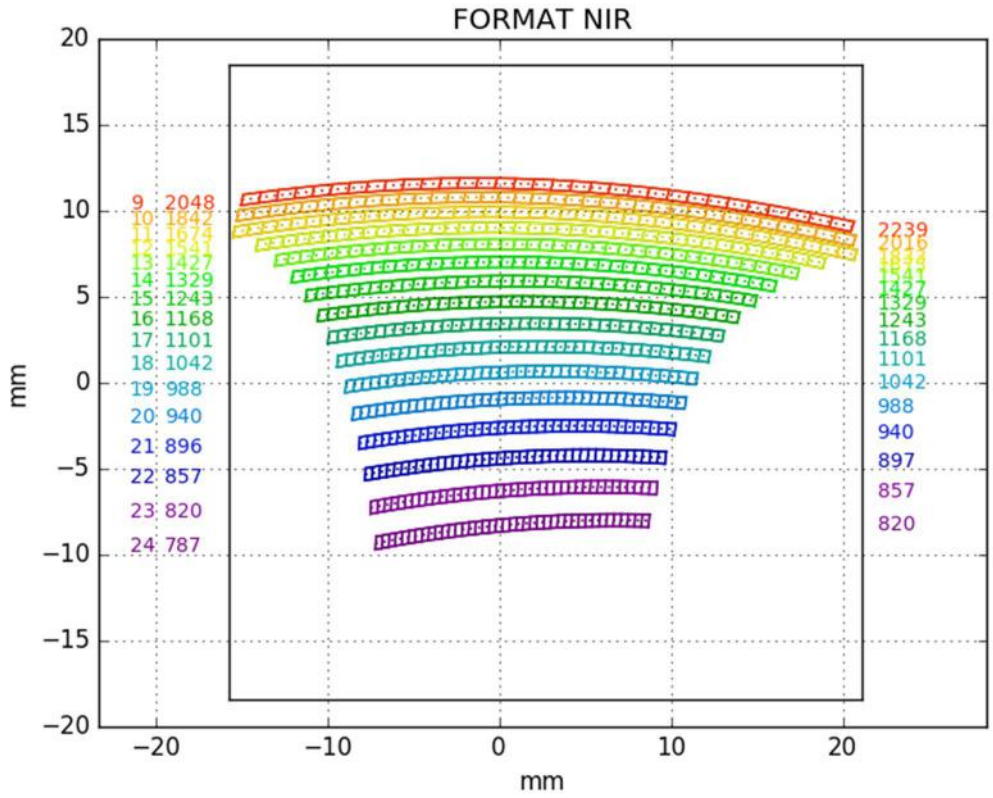

Figure 78: Spectral Format.

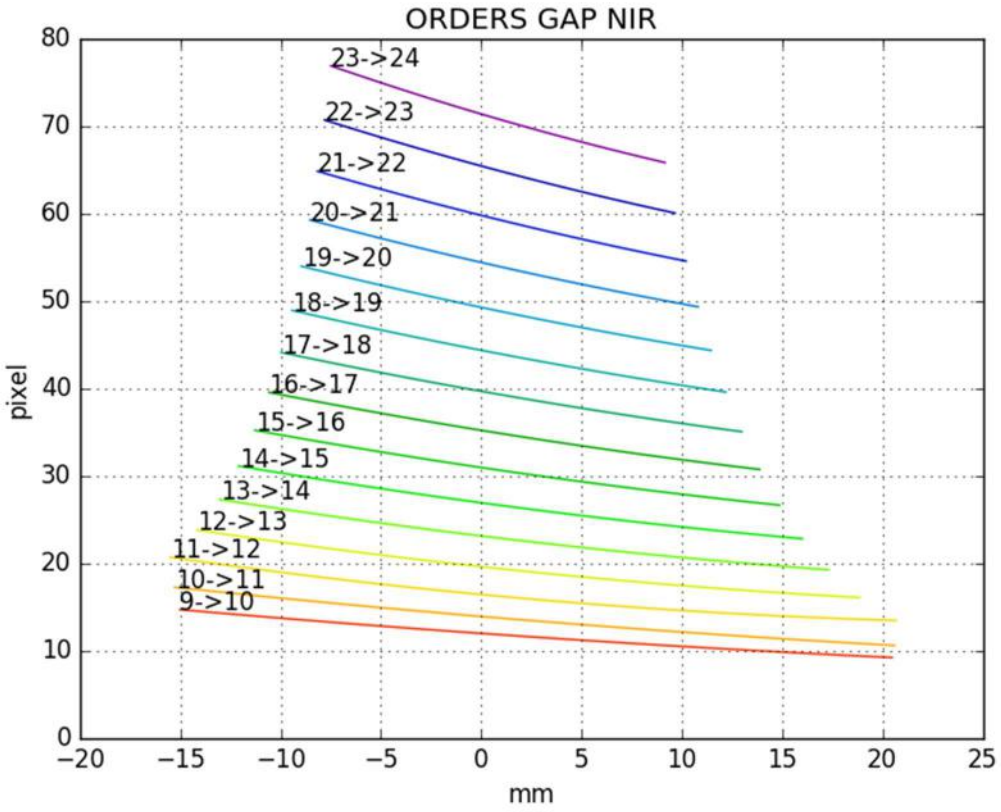

Figure 79: Inter-Order Gaps.

6.2.3 Scale and slit width

In Figure 80, the size of the image of the 1 arcsec slit on the detector is plotted. It shows that the scale on the detector is on average 0.25arcsec/pixels=0.0139arcsec/µm.

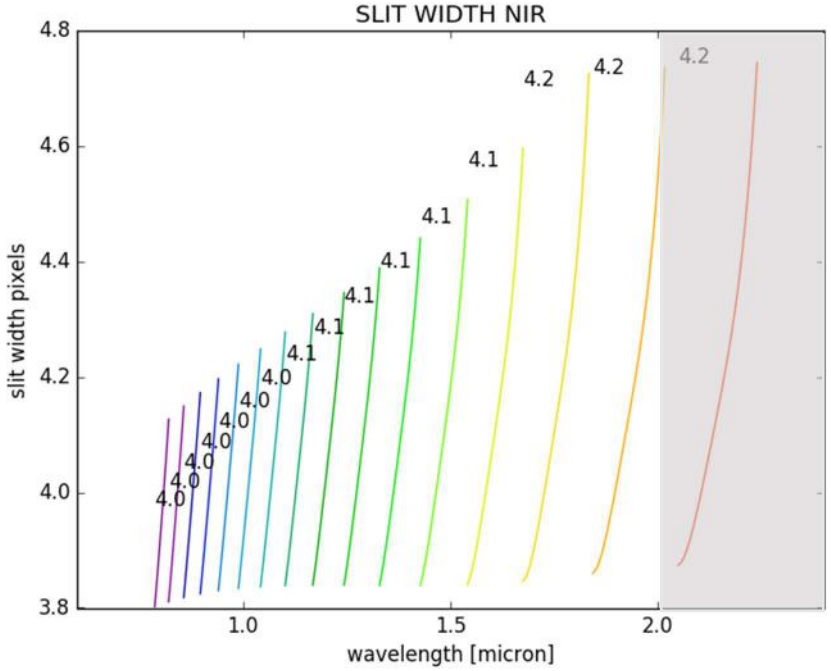

Figure 80: 1 arcsec slit image size on the detector (in pixels). Numbers in the upper part of each

order are the averages of slit width per order.

6.2.4 Image quality and Spot Diagrams

In Figure 85, Figure 83 and Figure 81 spot diagrams are reported for orders 11, 19 and 24. Boxes are 2 pixels (36 µm, 0.5 arcsec) wide. Plots are presented for 9 points along the order FSR.

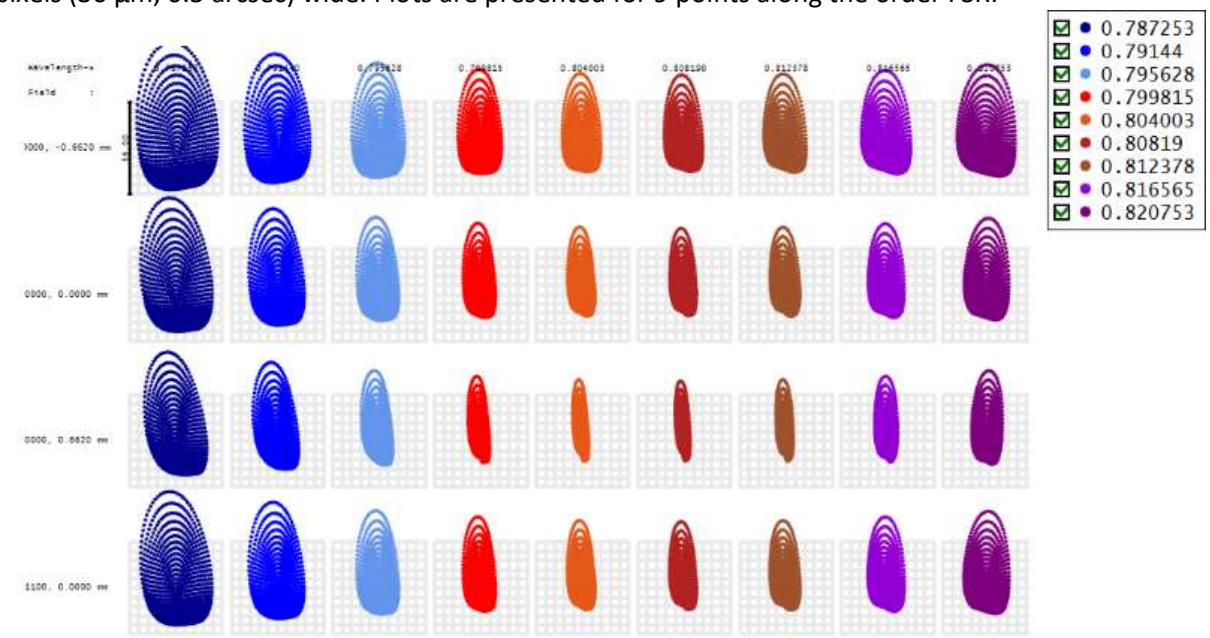

Figure 81: NIR spot diagrams (order 24, 790-821 nm).

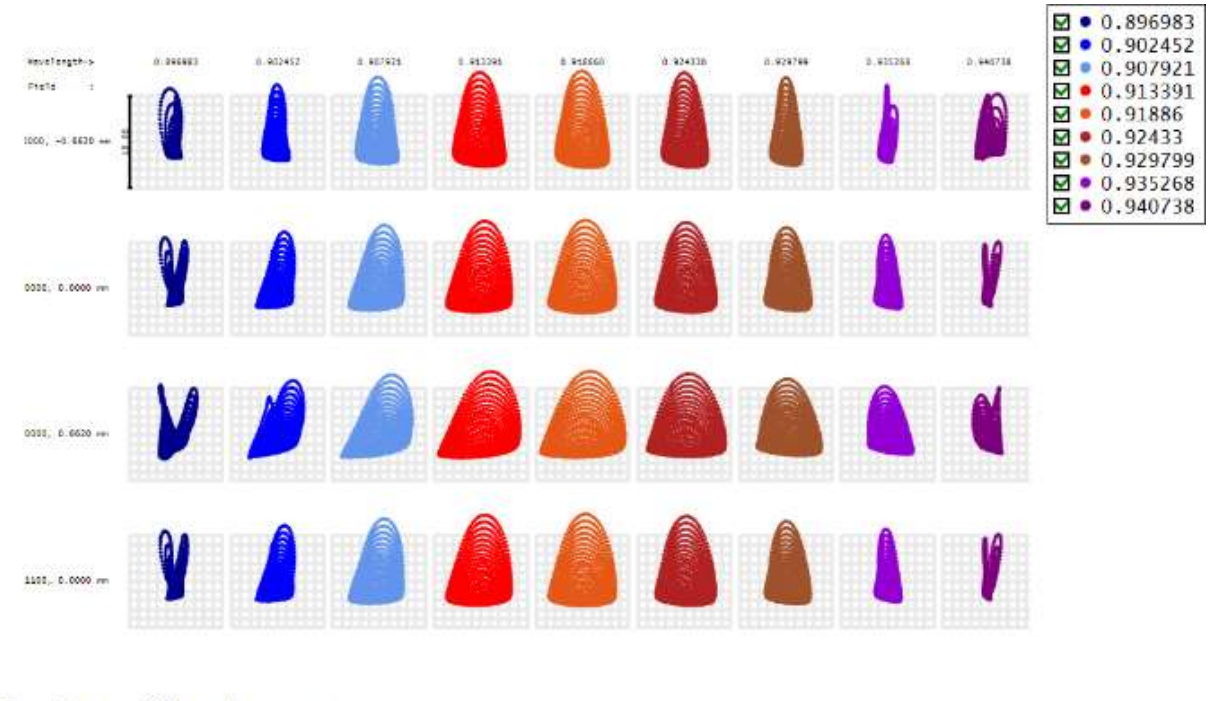

Figure 82: NIR spot diagrams (order 21, 897-941 nm).

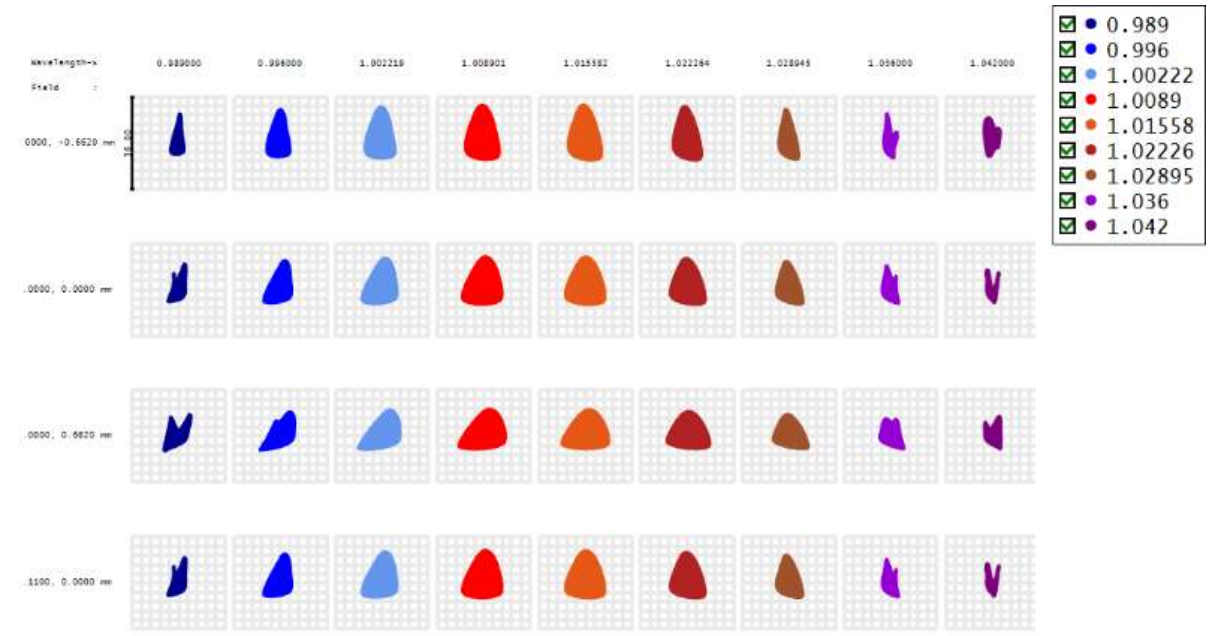

Figure 83: NIR spot diagrams (order 19, 989-1042 nm).

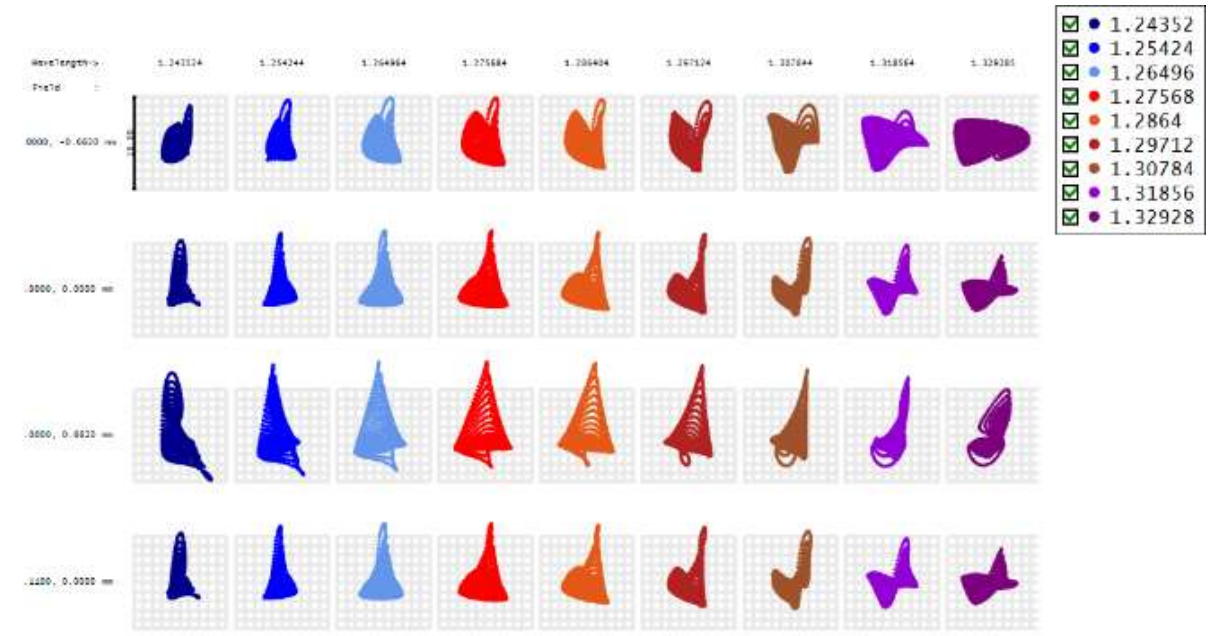

Figure 84: NIR spot diagrams (order 15, 1244-1329 nm).

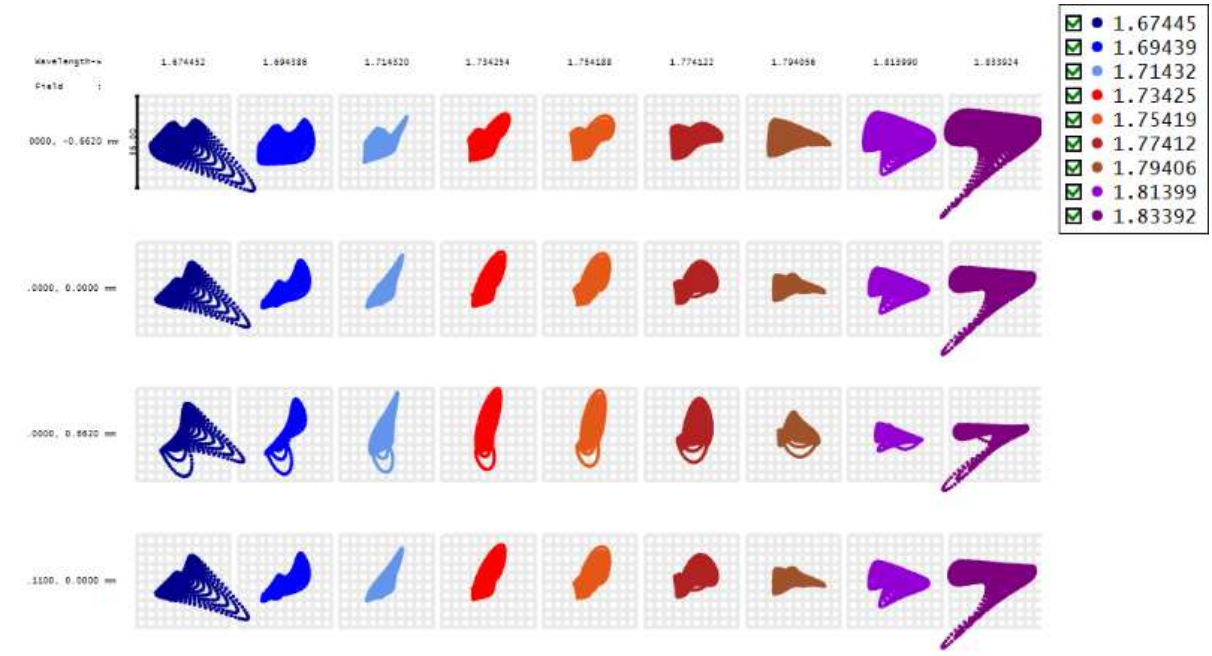

Figure 85: NIR spot diagrams (order 11, 1674-1834 nm).

6.2.5 Energy concentration and Enslitted energy

To evaluate energy concentration, we used the enslitted energy in the main dispersion direction, namely the diameter (in arcsec) containing 80% of the energy (D80).

As can be seen in Figure 86, D80 is nearly always less than 0.3 arcsec for wavelengths less than 2 µm. Values have been obtained via raytrace, and the Zemax results converted to arcsec, using the scale values shown in Figure 80.

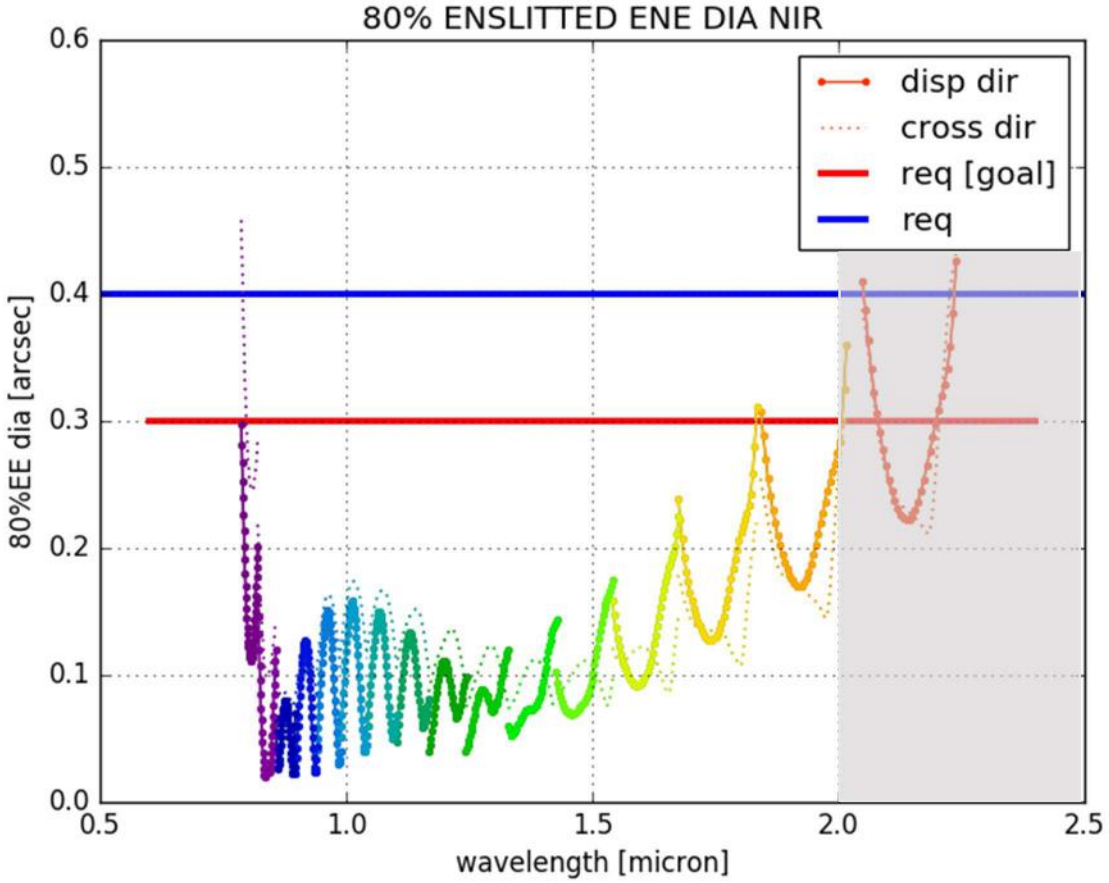

Figure 86: Enslitted energy in the main dispersion direction (D80).

6.2.6 Resolution

An estimate of the final resolution has been obtained, using the geometrical size of the slit vs. the positions of the spectral images of the slit. Figure 87 reports the obtained values, showing R to be, on average, ~5300 (for a 1 arcsec slit).

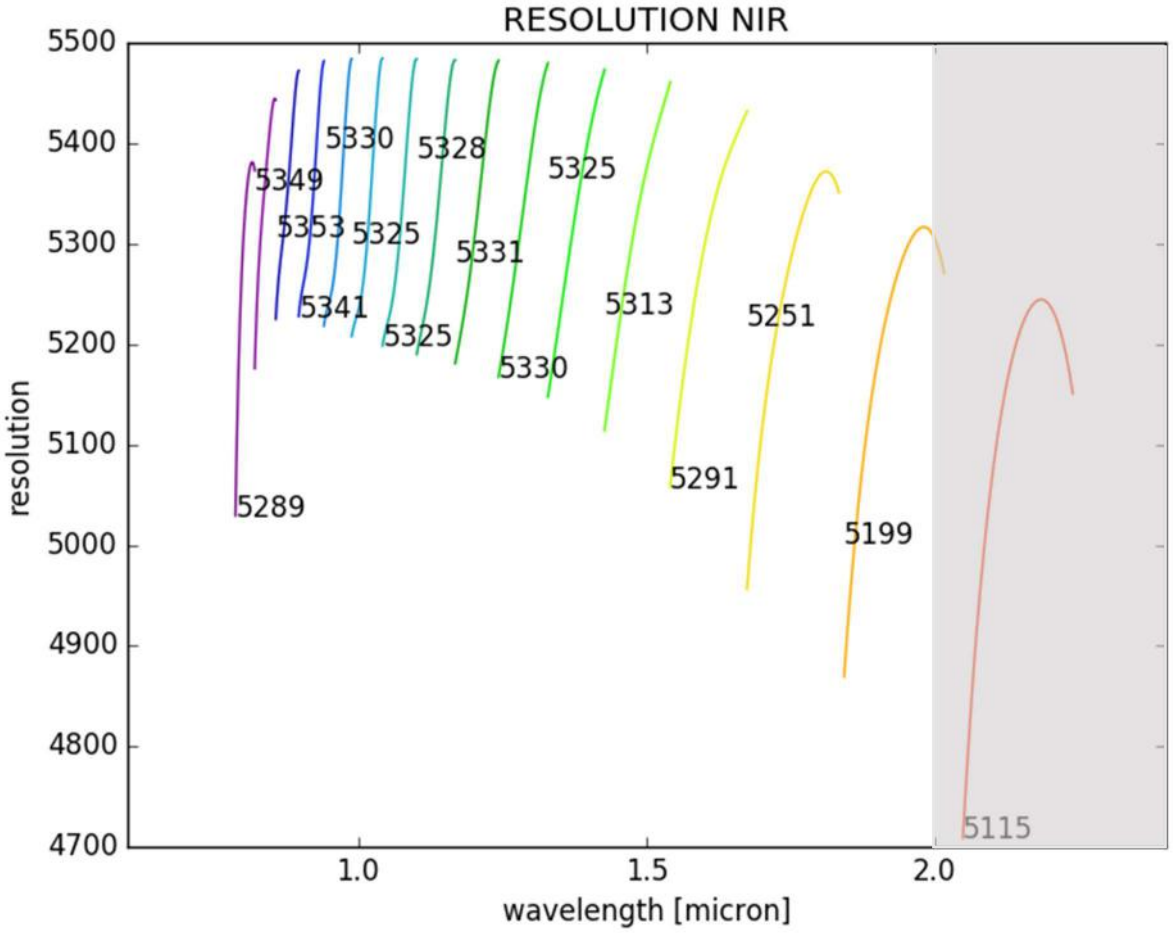

Figure 87: NIR Resolution.

6.2.7 Throughput

Throughput has been estimated using elements thickness-bulk-material-absorption (Zemax data) and estimates of the transmissivity and reflectivity of elements of CP and NIR spectrograph. In Figure 88, efficiencies are reported. Some notes:

- Each of the three telescope mirrors is assumed to have 0.8 flat reflectivity (TELMIR)
- Grating efficiency (DISPIR) is obtained by a preliminary simulation by Fraunhofer Institute (possible manufacturer of the elements)
- Antireflection coatings (ARCOIR) data are obtained by a preliminary optimization of a multilayer (5 layers) custom coating, designed by Andrea Bianco in Brera, giving a T>98% (and almost-always >99%)
- For the dichroic (DIIR), we adopted the transmissivity calculated by a manufacturer (thin films physics).
- The filter total transmissivity is assumed to be 95%, and consequently the transmissivity of each face is considered to be ~97.5%

Using the presented transmissivity/reflectivity, efficiencies for each element of the system are calculated and reported in Figure 90.

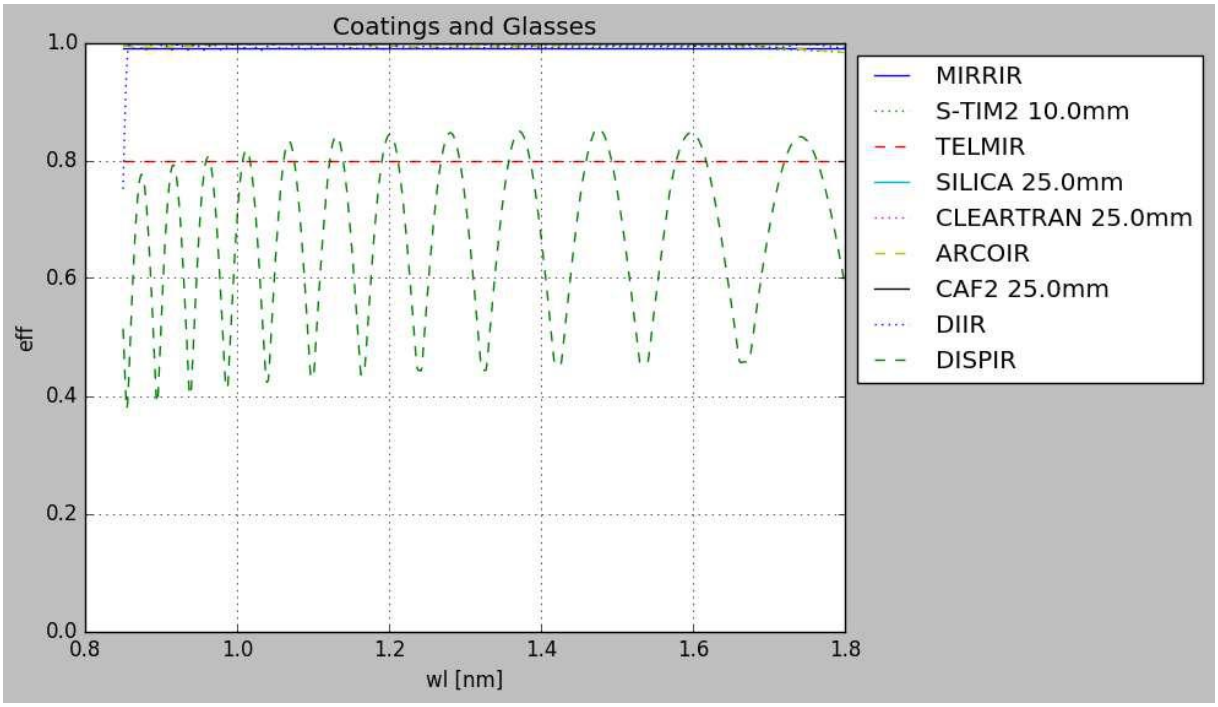

Figure 88: Coatings reflectivity/transmissivity and bulk transmission of materials and surfaces.

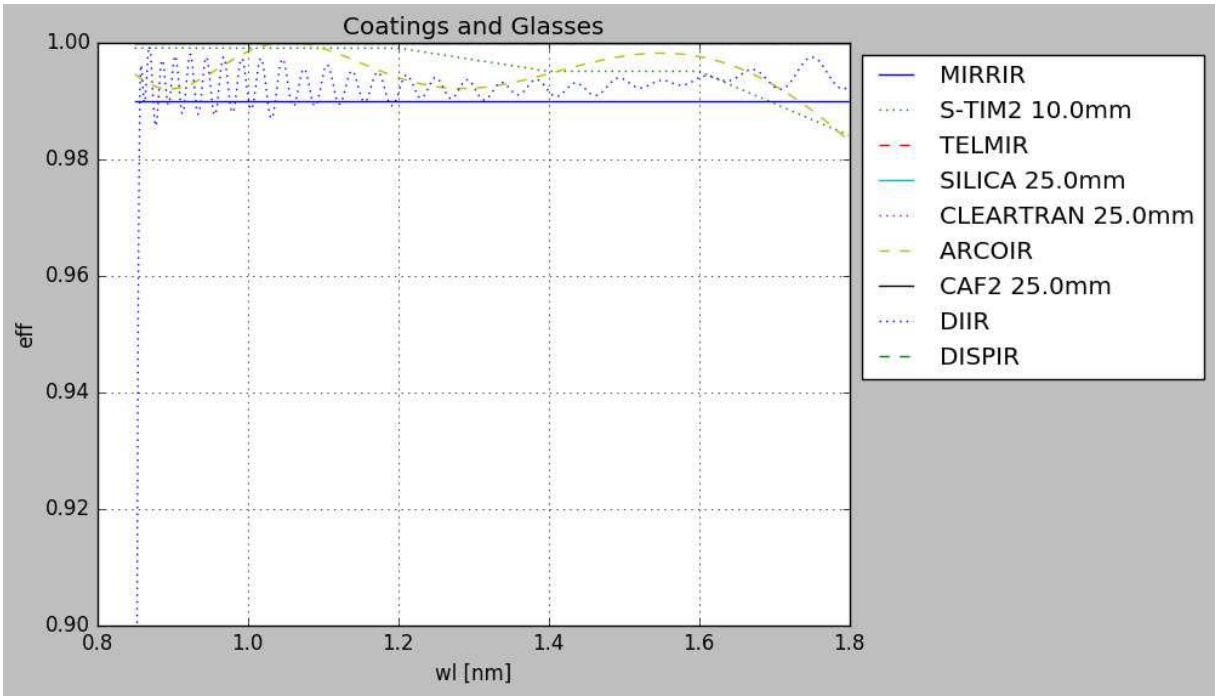

Figure 89: Coatings reflectivity/transmissivity and bulk transmission of materials and surfaces (0.9-1 zoom).

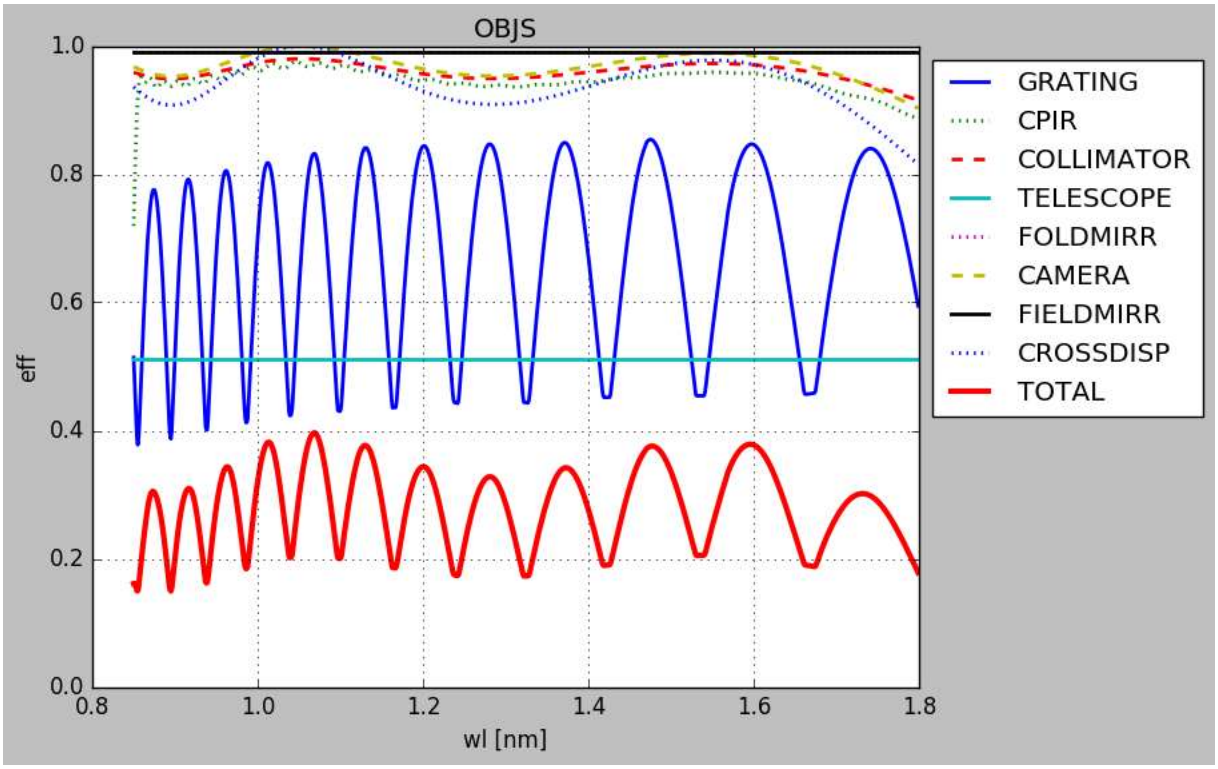

Figure 90: NIR elements efficiencies and total throughput.

We can adopt a contingency strategy similar to what has been done in section 5.4 for the UV-VIS:

- C=0.98 for each element (applied twice for double pass elements)
- C=0.9 for the grating
- C=0.9 for the common path (considered formed by 5 elements, each with a 0.98 contingency factor
- C=1 for the telescope optics

In Table 36, average Total Throughput (Tave), min and max for each element are reported together with same values for the Total Throughput and the contingency factors; last row reports total values using total contingency (71%).

Element	**Tave**	Tmax	Tmin	C
Telescope	0.51	0.51	0.51	1
Common path (IR)	0.94	0.98	0.72	0.9
Folding mirror	0.99	0.99	0.99	0.98
Collimator	0.96	0.98	0.91	0.96
Grating	0.67	0.85	0.37	0.9
Prisms	0.94	1	0.9	0.96
Field Mirror	0.99	0.99	0.99	0.98
Camera	0.97	0.9	1	0.98
TOTAL	**0.28**	**0.37**	**0.15**	0.71
Total With contingency	0.2	0.26	0.1	

Table 36: Elements and total efficiencies.

We do not expect large variations of the throughput along the silt, perhaps something of the order of 0.1%, but this has to be confirmed once the coatings data will be better assessed.

6.3 Sensitivity and Tolerance Analysis

A tolerance analysis has been performed on the system, to assess the optical quality of the system after the introduction of error due to manufacturing and positioning of elements. The adopted merit figure for this analysis was based on the 'X RMS spot size' where X is the main dispersion direction on the detector. The merit function evaluates the X RMS spot radius in 9 point for 15 orders, and has a value of 0.0033 for the nominal design.

The adopted errors on positioning are 50 µm on decentering for the three lenses of the camera and 100 µm for the rest. As for tilts, 0.025 deg for CM, 0.050 deg for CL and FM and Camera L1, L2; 0.1 deg for the remaining elements. Tolerance on the positioning along the optical axis was 100 µm, except for NIR-SM (50 µm) and Camera L3 (25 µm).

Error due to manufacturing:

- Radius of Curvature (or planarity) 0.1% radius, except CM with 0.05%. +/-1 fringes except filter and camera with +/-3 fringes.
- Surface irregularity: +/- 2 fringe except SM, aspheric with +/-0.5 fringes.
- Thickness 25 µm for camera lenses, 100µm otherwise
- Glasses: Index of Refraction +/- 1e-3
- Abbe Number 0.8%.

A first sensitivity analysis showed that all worst offenders (see Table 37) have similar effects on the Merit Function value, and that collimator mirror and camera are the most sensitive elements in terms of both alignment and manufacturing.

Element	Value	Merit F
L2 Y dec	+/- 50 µm	0.0042
L1 Y dec	+/- 50 µm	0.0041
Coll Mirror Radius	+/- 0.05%	0.0039
Grating Planarity	+/- 1 fringe	0.0039
Prism 3 Planarity	+/- 1 fringe	0.0038
Prism 3 Surf Irr	+/-0.5 fringe	0.0038
L2 Tilt X	+/-0.05 deg	0.0038
Prism 2 Planarity	+/- 1 fringe	0.0038
Coll Lens Radius	+/- 0.1%	0.0037
Aspheric Surface Irr	+/- 0.5 fringe	0.0037
Slit Mirror Planarity	+/- 1 fringe	0.0037
Coll Mirror Tilt Y	+/- 0.025 deg	0.0037
Prism 1 Planarity	+/- 1 fringe	0.0036
Prism 2 Surf Irr	+/- 0.5 fringe	0.0036

Table 37: worst offenders list.

A 100 realization MonteCarlo analysis helps us to estimate the combined effect of all errors:

Percentage	MF
90% >	0.0070
80% >	0.0064
50% >	0.0056
20% >	0.0049
10% >	0.0046

In Figure 92, the D80 values for all the 100 realizations are plotted: in colored lines the nominal design, in light gray all the MC realizations. We have marked with green realizations between 45th and 55th percentile. In Figure 92 we mark with yellow realizations below 80th percentile. The plot shows that essentially for all these realization, the enclosed energy diameter D80 is less than 0.4arcsec for wavelengths less than 2.0 µm.

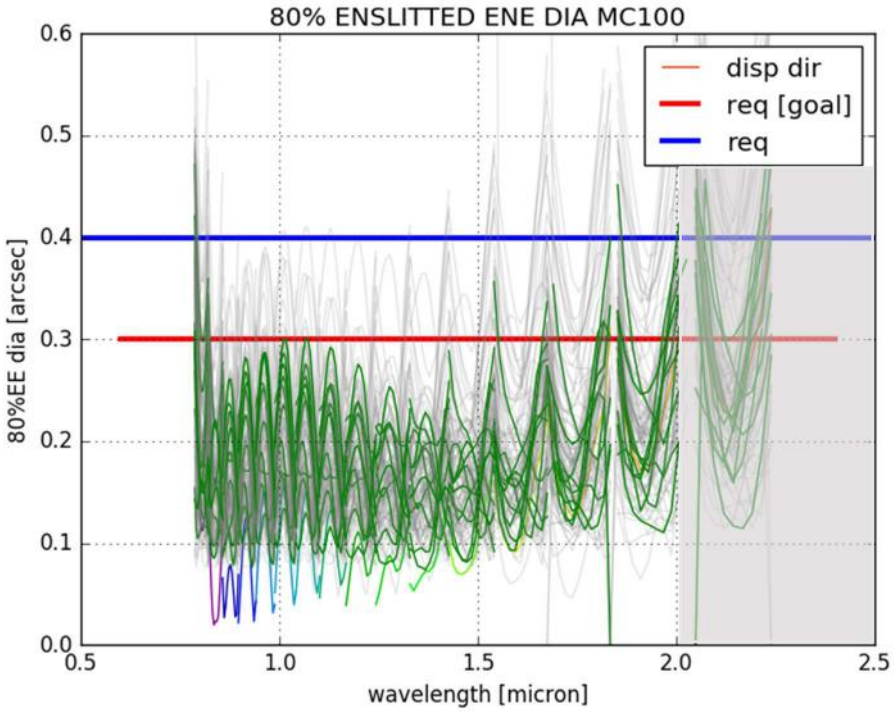

Figure 91: Enslitted energy (along the main dispersion direction) for all 100 MC realizations (gray). In green we mark MC realizations between 45-55 percentile.

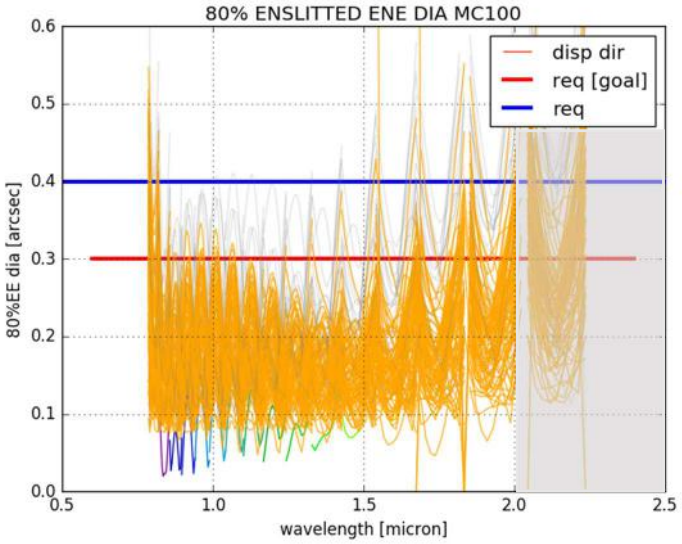

Figure 92: Enslitted energy (along the main dispersion direction) for all 100 MC realizations. In yellow, realizations below the 80th percentile.

6.4 Temperature behaviour

A temperature dependent model in Zemax has been developed, to estimate changes in the optical quality and displacement of the spectrum due to variations of the working temperature of the system. The model assumes the slit to be a fixed point and expands distances (and all other dimensional characteristics of the elements) according to the thermal coefficient of expansion (TCE) of materials.
The same model may be used to estimate performances of the system at ambient temperature.
NIR spectrograph uses two working temperatures: 150K for all the elements, except the filter, the third lens of the camera and the detector, working at 40K.
A more complex model, based on the mechanical simulations, will be derived in the framework of the mechanical analysis for FDR.

6.4.1 TCEs and Index of refraction

When going from ambient temperature to working temperatures, the TCE of materials may not be considered constant; variation of the TCE itself should be considered. For aluminium and glasses, data about the TCE vs Temp may be retrieved (see RD09, RD10, RD11, RD12). Since Zemax may use only a constant TCE, for each material (or two, for those materials used at 150K and at 40K), an average TCE has been derived, to ensure the right dimension variation for the considered temperature variation.
Used values are summarized in Table 38, TCEs plots in Figure 93

Material	AVE TCE 40-290K	AVE TCE 150-290K	TCE @40K	TCE @150K
Aluminum	16.4	20.7	4.7	17.6
CAF2	-	16.3	-	12.8
Cleartran	4.2	5.2	2.1	4.2
Infrasil	0.1	0.17	0	0

Table 38: Average TCEs of used materials, used in the model, and 'instantaneous' TCEs at 40k and 150K

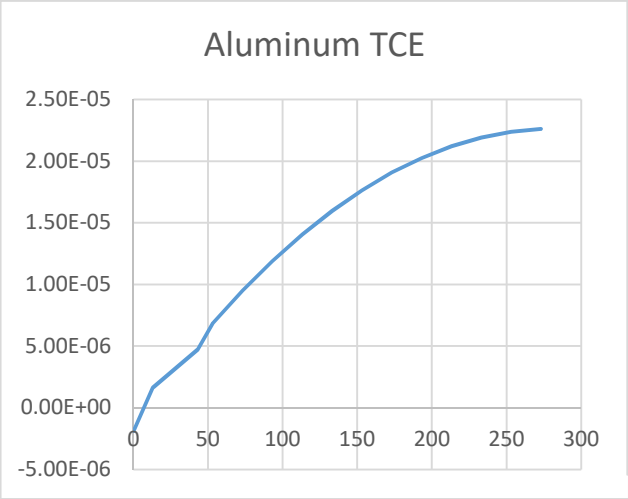

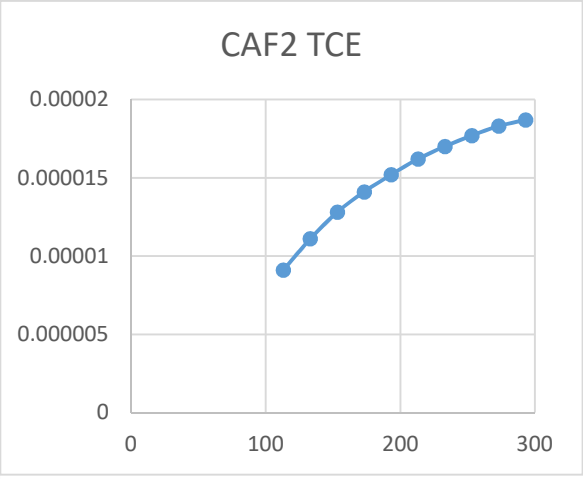

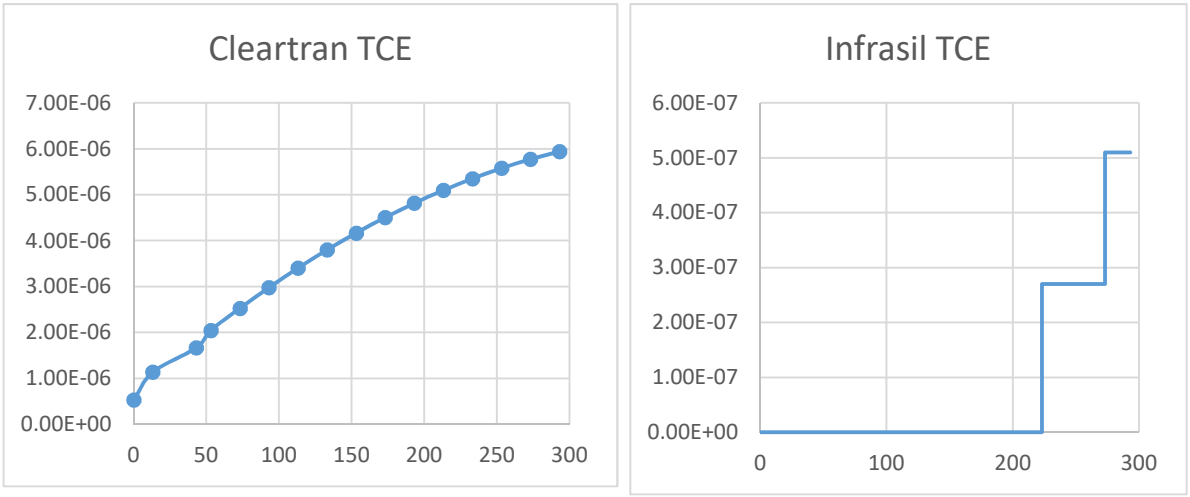

Figure 93: Variation of TCEs of used materials in the considered temperature range.

We used standard glasses Zemax glasses in this model, because optical quality remains similar to nominal one, and developed glass models from CHARM data do not present temperature dependence for the n index.

6.4.2 From Twork to 20°C

Spot diagrams of the system for three orders are illustrated in *Figure 94*, at T=40K and 150K (nominal, upper row) and at T=293.15 (lower row). It can be noted that even when using Zemax standard glasses, the spots are very similar to nominal one for Twork. Going to 20°C (and to atmospheric pressure), a good optical quality can be recovered, moving L1 of about 500 µm (along the camera axis). This should assure the possibility to roughly align the spectrograph at ambient condition.

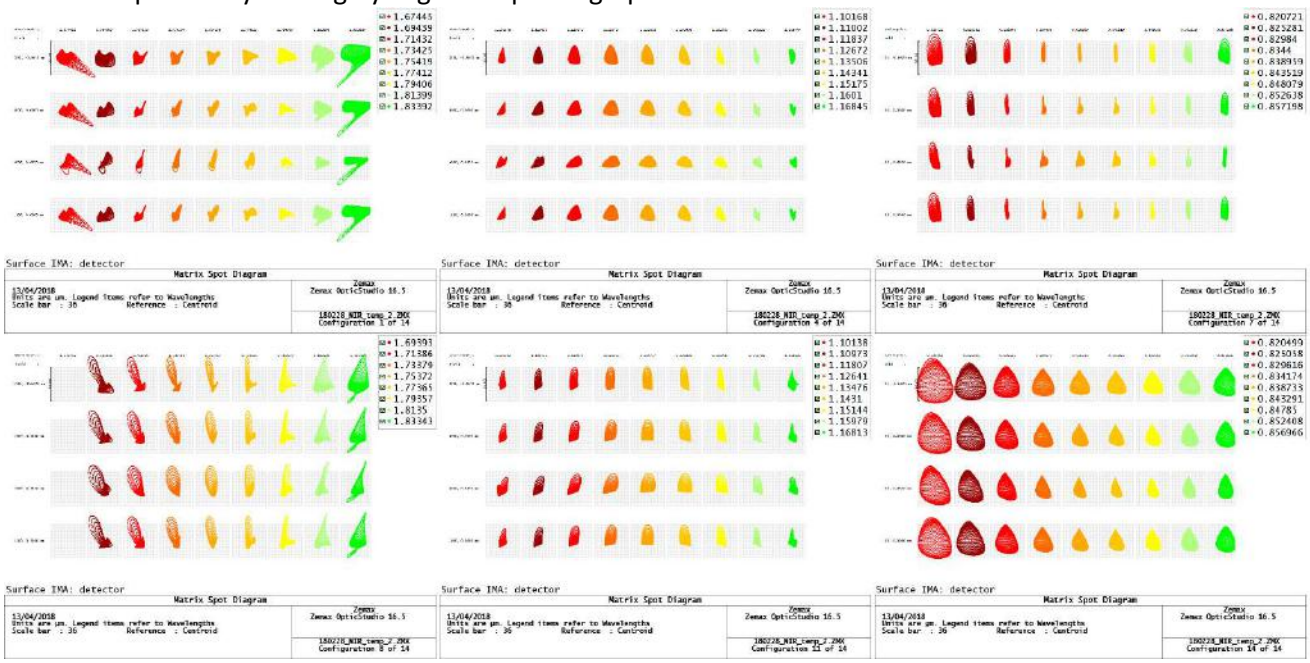

Figure 94. Spots for three orders at Twork (40K/150K, P=0atm, upper panel) and at 293K, 1 atm (lower panel). Boxes are 36x36µm (2x2 pixel)

6.4.3 Stability at 150K

The change of temperature causes a displacement of the spectrum, as can be seen in Figure 95 : for the [150-290]K range, the displacement (calculated as the average displacement on the detector, in 7

orders and 9 wavelenghth) is about 2.4mm, , i.e. 20 µm/K. An analysis performed using 'instantaneous' TCEs gives a value of 40 µm/K. Consequently, assuming that a stability of about 1/10 of pixel is the goal stability during an exposure, temperature of the NIR spectrograph should be kept constant in the order of 1/20 K. For this variation of temperature, optical quality itself remains essentially unchanged (see *Figure 96*).

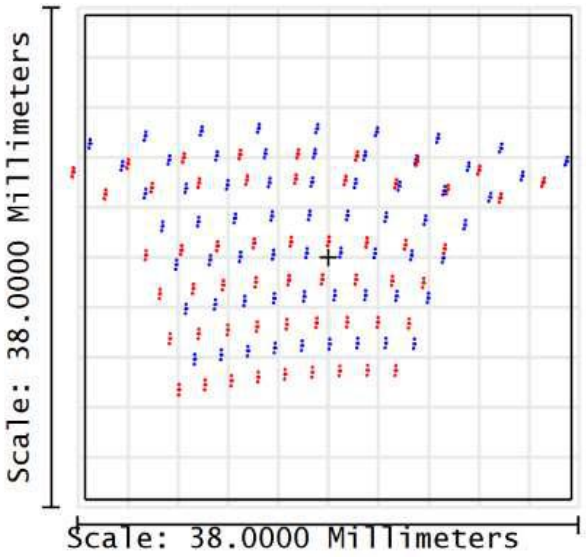

Figure 95: spectrum displacement from 150 (40)K (BLUE) to 293K (RED).

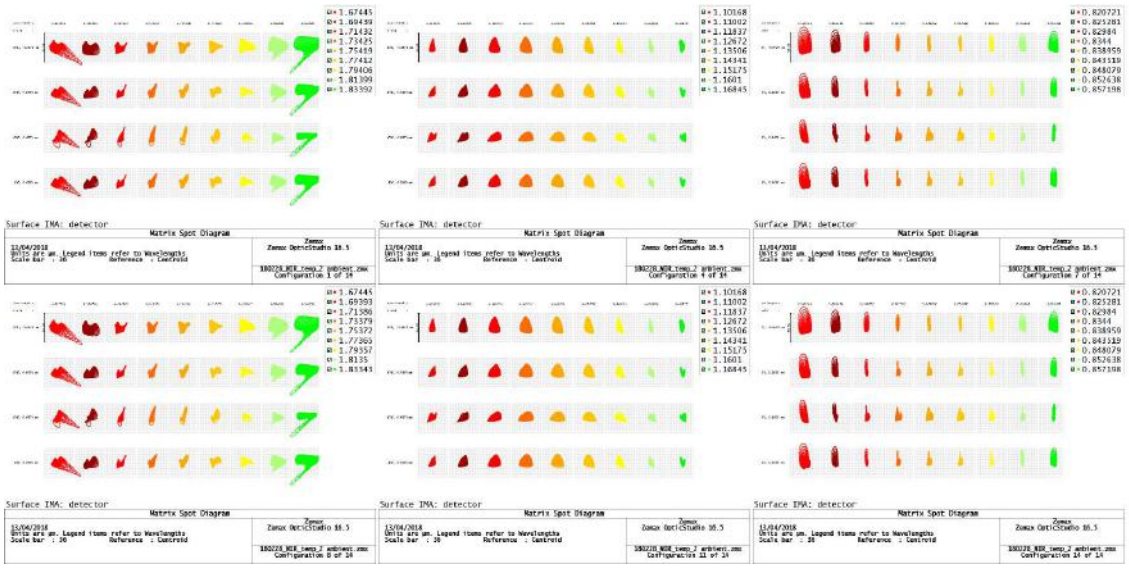

Figure 96: spot diagrams for variation of 1K around Twork; no variation is visible.

6.5 Ghosts and Straylight

To study Ghosts and straylight for the NIR spectrograph, we have followed a 'mixed' approach:

- For the double bounce camera ghosts (ghosts due to double reflections among camera elements) we used the sequential capabilities of Zemax
- For one bounce ghosts due to corrector lens and prisms, we have verified graphically that no ray may reach the detector, using a non-sequential Zemax model
- We used the same model to study the complete behavior of the system, thus allowing ghosts

due to double bounce on Prism and Corrector lens, and to their interaction with the camera elements.

6.5.1 Camera Ghosts

Given the axial symmetry of the camera, it was possible to study the ghosts created by the camera, in a sequential Zemax model. The goal is to estimate the 'pollution' due to the camera ghosts on the nominal spectrum, i.e. given a nominal photon count per pixel due to the source on the detector (N), we estimate how many photons in the same pixels will be caused by all the ghosts (NG).
We adopted:

- For each surface of lenses R=0.02
- For thermal filter surfaces R=0.05
- For the detector R=0.2

Having 9 surfaces (1 detector, 3x2 lenses surfaces and 2 filter surfaces), we expect to have 9x8/2 ghosts due to the camera; to each ghost we associate 2 parameters: the Area A of the ghost and the Percentage P of rays reaching the detector. We used a Zemax model that includes all orders (10-24) and 9 wavelengths per order.
Both A and P parameters are estimated by the 'footprint' feature in Zemax, estimating A (in pixels) as the area of a rectangle inscribing the ghost footprint (this may be an overestimate of the area).
In the following table, all the ghosts footprint and layout are reported.

NIR_L1_S2-NIR_L1_S1

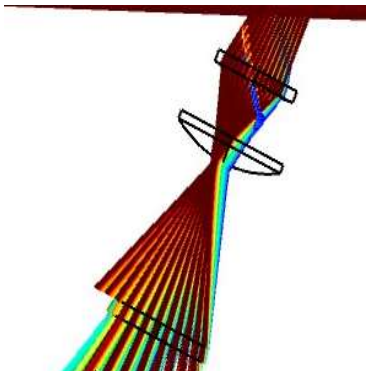

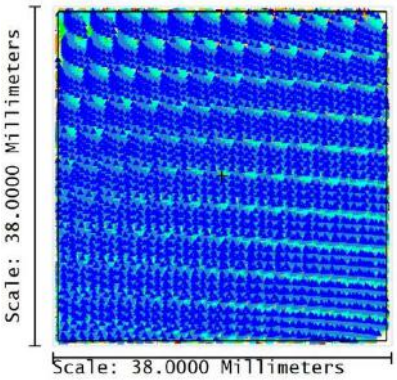

NIR_L2_S1-NIR_L1_S1

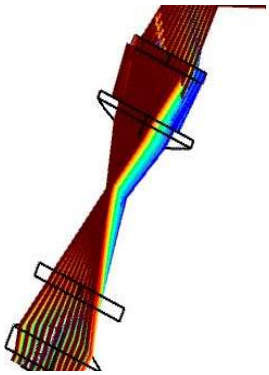

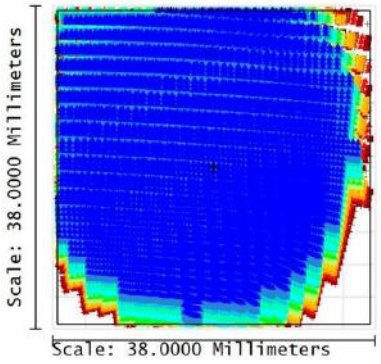

NIR_L2_S1-NIR_L1_S2

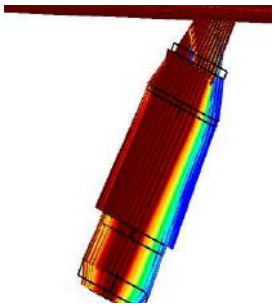

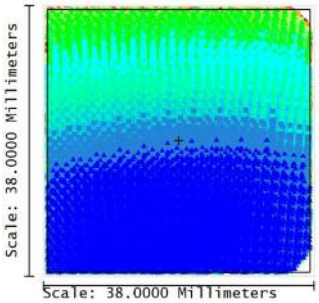

NIR_L2_S2-NIR_L1_S1

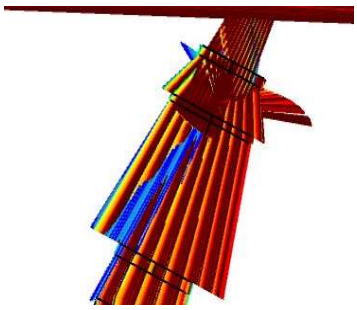

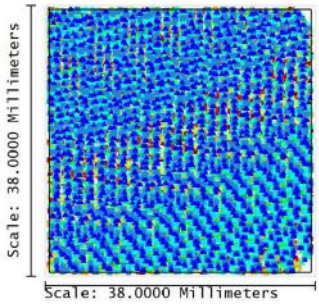

NIR_L2_S2-NIR_L1_S2

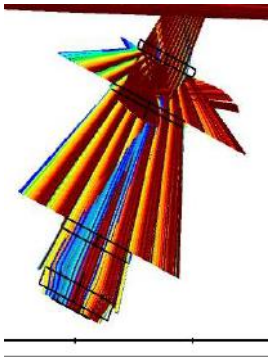

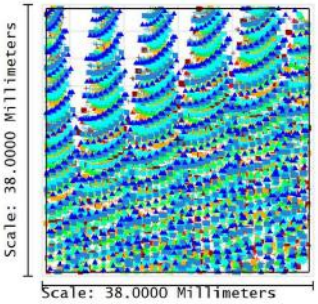

NIR_L2_S2-NIR_L2_S1

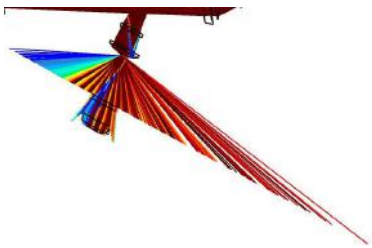

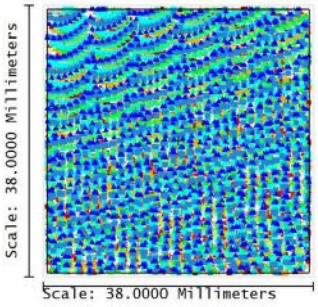

NIR_F_S1-NIR_L1_S1

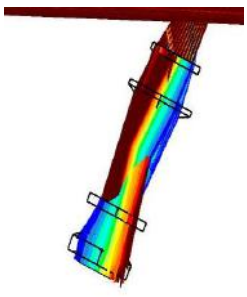

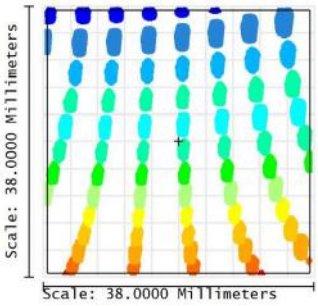

NIR_F_S1-NIR_L1_S2

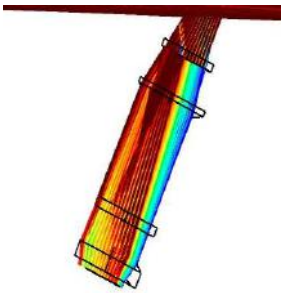

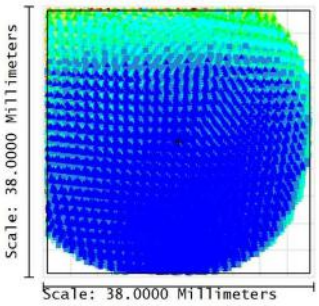

NIR_F_S1-NIR_L2_S1

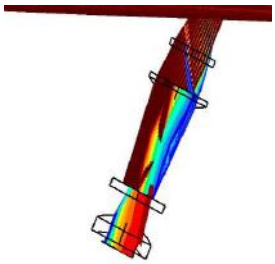

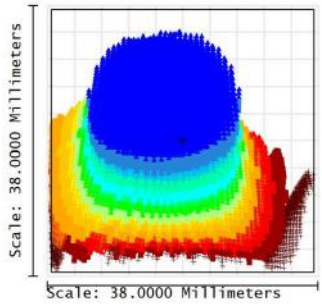

NIR_F_S1-NIR_L2_S2

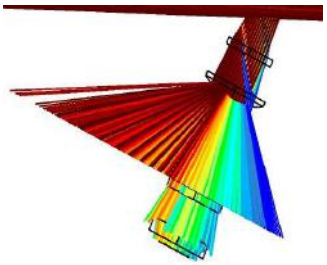

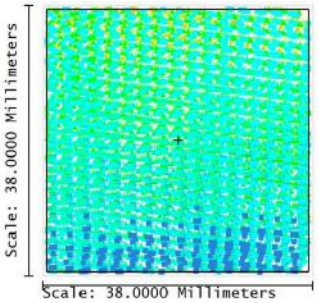

NIR_F_S2-NIR_L1_S1

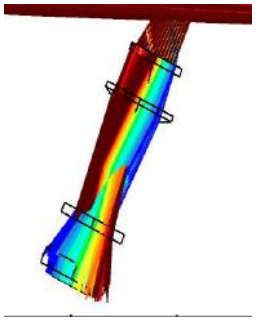

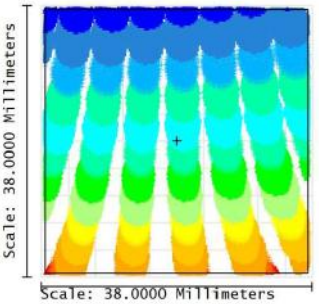

NIR_F_S2-NIR_L1_S2

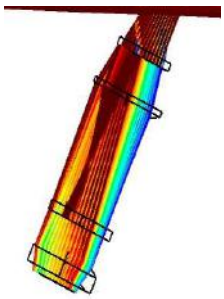

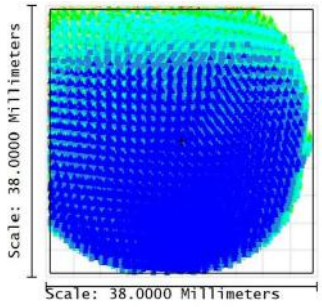

NIR_F_S2-NIR_L2_S1

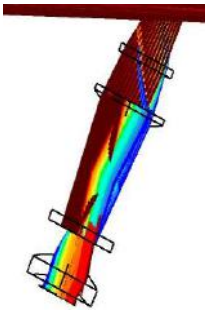

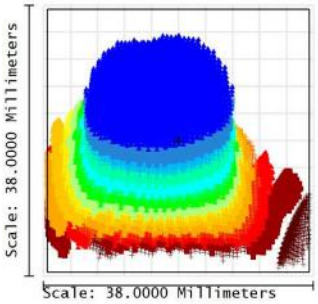

NIR_F_S2-NIR_L2_S2

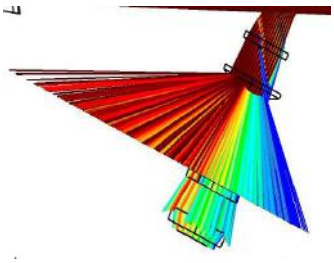

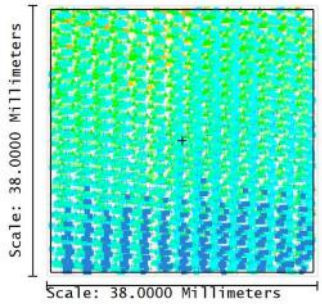

NIR_F_S2-NIR_F_S1

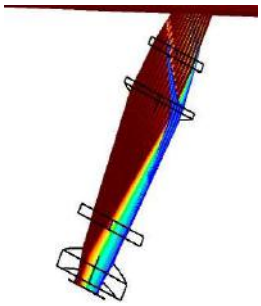

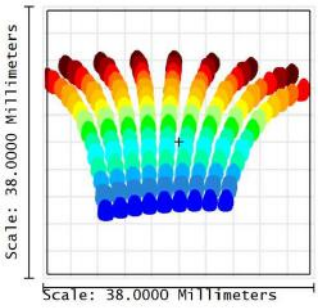

NIR_L3_S1-NIR_L1_S2

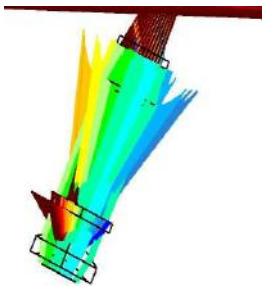

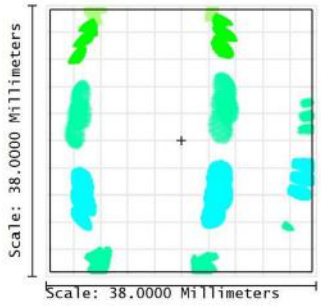

NIR_L3_S1-NIR_L2_S1

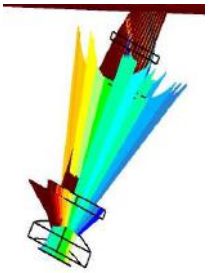

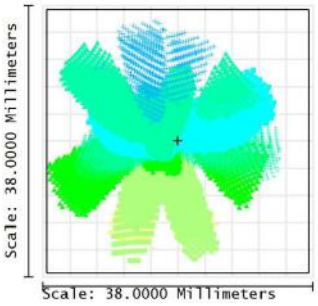

NIR_L3_S1-NIR_F_S1

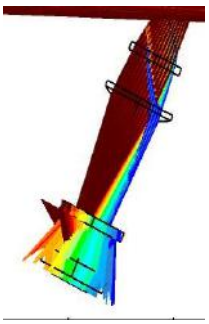

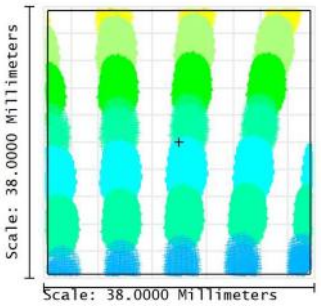

NIR_L3_S1-NIR_F_S2

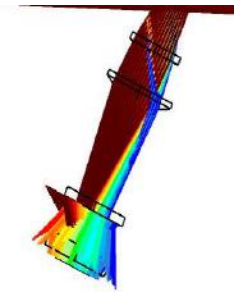

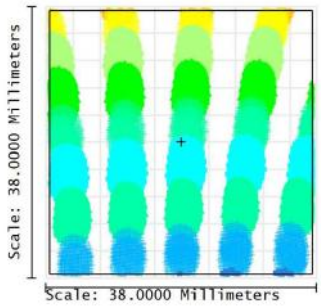

NIR_L3_S2-NIR_L1_S1

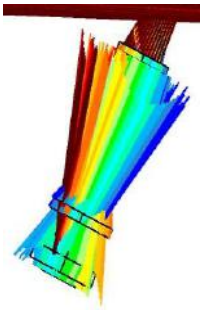

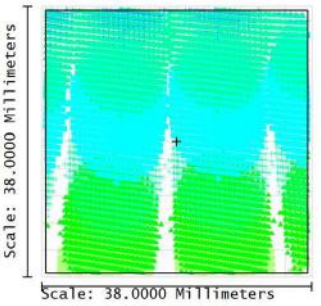

NIR_L3_S2-NIR_L1_S2

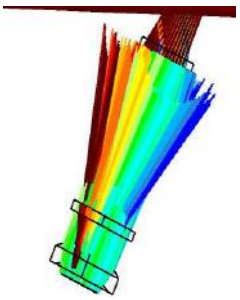

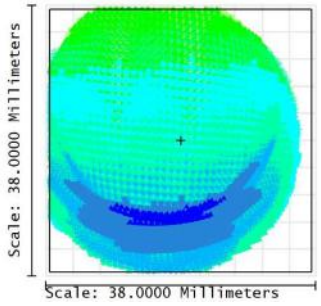

NIR_L3_S2-NIR_L2_S1

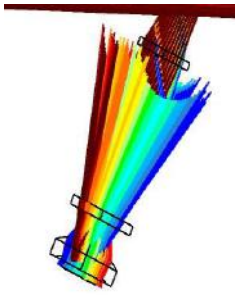

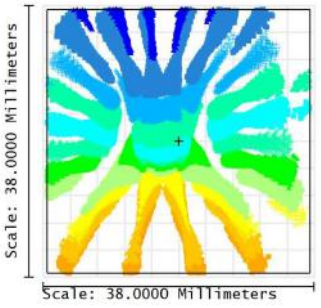

NIR_L3_S2-NIR_F_S1

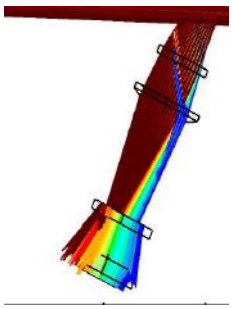

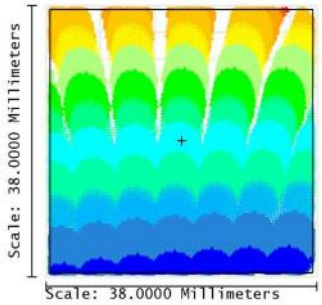

NIR_L3_S2-NIR_F_S2

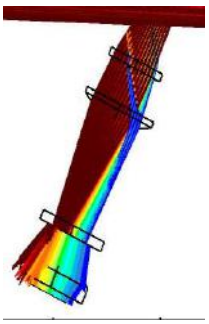

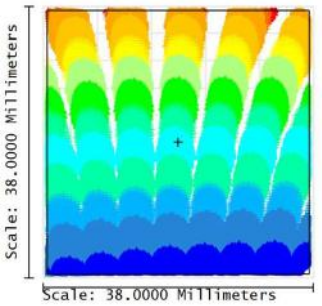

NIR_L3_S2-NIR_L3_S1

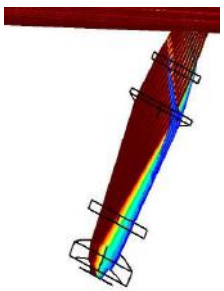

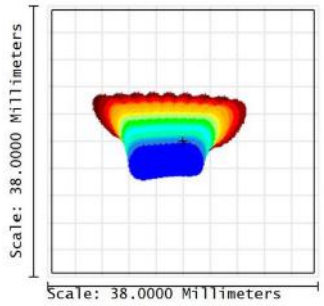

NIR_Detector-NIR_L1_S1

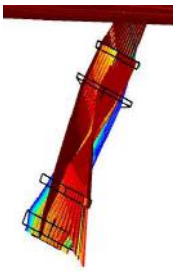

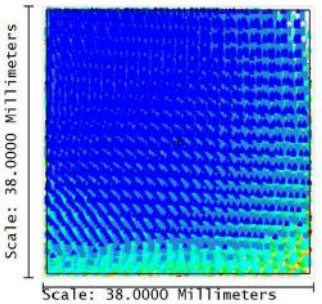

NIR_Detector-NIR_L1_S2

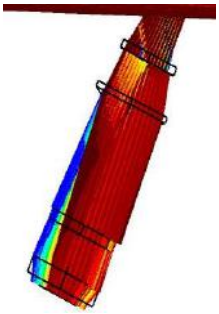

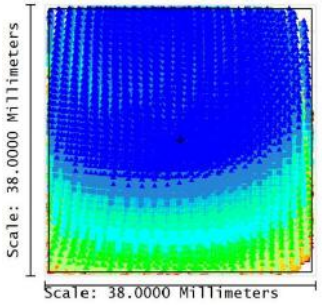

NIR_Detector-NIR_L2_S1

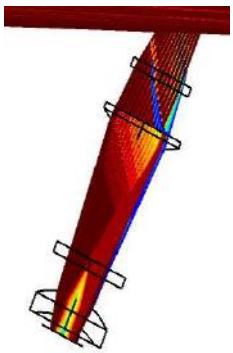

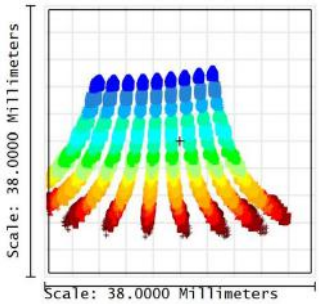

NIR_Detector-NIR_L2_S2

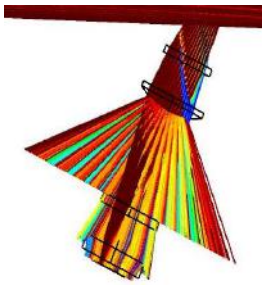

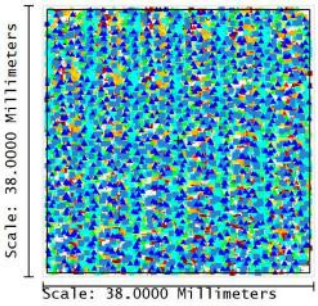

NIR_Detector-NIR_F_S1

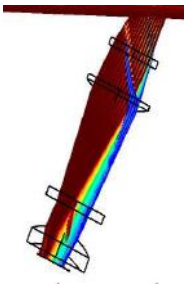

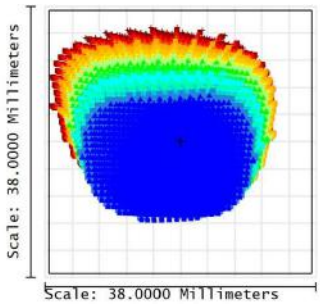

NIR_Detector-NIR_F_S2

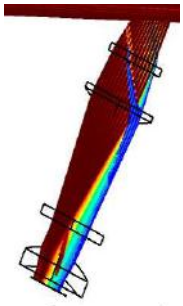

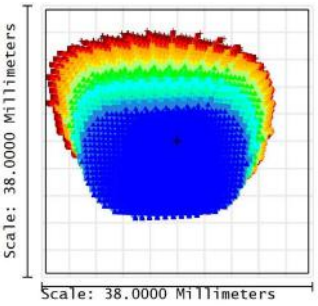

NIR_Detector-NIR_L3_S1

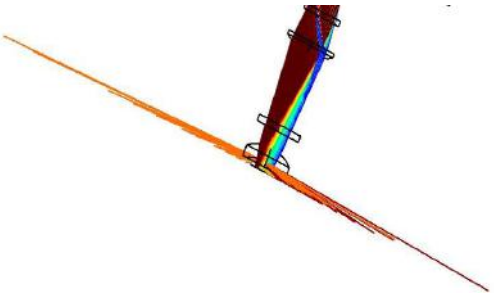

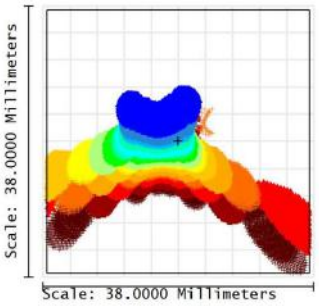

Table 39: layout and Footprint of Camera ghosts.

With values for R, A and P we can calculate PP(S1,S2), fraction of photons per pixel due to the ghost generated by surfaces S1 and S2.

PP(S1,S2)=P*R(S1)*R(S2)/A

Data of ghosts are summarized in Table 40; the SWA column reports the diameter of the ghost due to a monochromatic source (central wavelength of central order), the SWR column is the ratio of irradiance of the monochromatic ghost and of nominal image (calculated as R1 x R2 /SWA).

S1	S2	A (pixels^2)	P	PP	R1	R2	SWA(pixels^2)	SWA Dia (pixels)	SWR
NIR_Detector	NIR_L3_S2	2.6E+06	9.8E-01	3.8E-09	20%	5%	7.0E+05	8.4E+02	3.6E-08
NIR_Detector	NIR_L3_S1	2.6E+06	9.8E-01	3.8E-09	20%	5%	8.6E+05	9.3E+02	3.0E-08
NIR_Detector	NIR_F_S2	1.4E+06	9.8E-01	2.7E-09	20%	2%	8.3E+04	2.9E+02	1.2E-07
NIR_Detector	NIR_L2_S1	2.5E+06	9.4E-01	1.5E-09	20%	2%	9.0E+03	9.5E+01	1.1E-06
NIR_Detector	NIR_F_S1	2.9E+06	9.2E-01	1.2E-09	20%	2%	5.1E+04	2.2E+02	2.0E-07
NIR_F_S2	NIR_L3_S1	2.6E+06	9.7E-01	9.2E-10	5%	5%	1.2E+04	1.1E+02	5.2E-07
NIR_Detector	NIR_L1_S2	4.2E+06	8.3E-01	7.9E-10	20%	2%	2.8E+06	1.7E+03	3.6E-09
NIR_Detector	NIR_L1_S1	4.2E+06	6.6E-01	6.3E-10	20%	2%	3.1E+06	1.8E+03	3.3E-09
NIR_L3_S2	NIR_F_S1	7.8E+05	9.9E-01	5.1E-10	2%	2%	3.7E+04	1.9E+02	2.8E-08
NIR_F_S2	NIR_L2_S1	3.7E+06	9.5E-01	2.6E-10	5%	2%	7.7E+05	8.8E+02	3.3E-09
NIR_F_S1	NIR_L2_S1	3.8E+06	9.6E-01	2.5E-10	5%	2%	9.3E+05	9.7E+02	2.7E-09
NIR_F_S2	NIR_L1_S2	4.2E+06	8.6E-01	2.1E-10	5%	2%	2.8E+06	1.7E+03	9.0E-10
NIR_F_S1	NIR_L1_S2	4.2E+06	8.6E-01	2.0E-10	5%	2%	2.8E+06	1.7E+03	9.1E-10
NIR_F_S1	NIR_L1_S1	4.2E+06	4.9E-01	1.2E-10	5%	2%	9.2E+03	9.6E+01	2.8E-07
NIR_L3_S2	NIR_L3_S2	4.2E+06	4.7E-01	1.1E-10	2%	5%	1.2E+05	3.5E+02	2.1E-08
NIR_F_S2	NIR_L1_S1	4.2E+06	4.6E-01	1.1E-10	5%	2%	9.2E+04	3.0E+02	2.8E-08
NIR_L3_S2	NIR_L3_S1	4.2E+06	4.0E-01	9.6E-11	2%	5%	1.7E+05	4.2E+02	1.5E-08
NIR_L2_S1	NIR_L1_S1	4.2E+06	8.8E-01	8.4E-11	2%	2%	3.6E+06	1.9E+03	2.8E-10
NIR_Detector	NIR_L2_S2	4.2E+06	8.4E-02	8.0E-11	20%	2%	3.5E+06	1.9E+03	2.9E-09
NIR_L2_S1	NIR_L1_S2	4.2E+06	6.1E-01	5.8E-11	2%	2%	2.6E+06	1.6E+03	3.9E-10
NIR_L3_S1	NIR_L3_S2	4.2E+06	2.2E-01	5.2E-11	2%	5%	1.3E+05	3.6E+02	1.9E-08
NIR_L3_S1	NIR_L3_S1	4.2E+06	1.7E-01	4.0E-11	2%	5%	1.4E+05	3.8E+02	1.8E-08
NIR_L1_S2	NIR_L1_S1	4.2E+06	3.4E-01	3.2E-11	2%	2%	3.9E+06	2.0E+03	2.6E-10
NIR_L3_S2	NIR_L2_S1	4.2E+06	3.3E-01	3.2E-11	2%	2%	5.4E+04	2.3E+02	1.9E-08
NIR_L3_S2	NIR_L1_S2	4.0E+06	2.3E-01	2.3E-11	2%	2%	1.1E+06	1.0E+03	9.6E-10
NIR_L3_S1	NIR_L2_S1	3.4E+06	1.3E-01	1.5E-11	2%	2%	4.5E+05	6.7E+02	2.3E-09
NIR_L2_S2	NIR_L1_S1	4.2E+06	1.5E-01	1.4E-11	2%	2%	3.8E+06	2.0E+03	2.7E-10
NIR_F_S1	NIR_L2_S2	4.2E+06	5.5E-02	1.3E-11	5%	2%	2.4E+06	1.6E+03	1.1E-09
NIR_F_S2	NIR_L2_S2	4.2E+06	5.1E-02	1.2E-11	5%	2%	3.1E+06	1.8E+03	8.3E-10
NIR_L2_S2	NIR_L2_S1	4.2E+06	8.7E-02	8.3E-12	2%	2%	3.5E+06	1.9E+03	2.9E-10
NIR_L3_S2	NIR_L1_S1	4.2E+06	7.3E-02	7.0E-12	2%	2%	3.7E+05	6.1E+02	2.8E-09
NIR_L3_S1	NIR_L1_S2	3.9E+06	6.4E-02	6.5E-12	2%	2%	5.6E+03	7.5E+01	1.8E-07
NIR_L2_S2	NIR_L1_S2	4.2E+06	6.2E-02	5.9E-12	2%	2%	3.3E+06	1.8E+03	3.1E-10
TOTAL				**1.7E-8**					

Table 40: Ghost Camera Data: S1 and S2 are the two surfaces involved in the generation of the ghost, R1 and R2 reflectance of S1 and S2. A is the estimated area in pixel^2 of the whole ghost, P the percentage of rays able to arrive to the detector after the ghost, PP fraction of the photons in a pixel due to the ghost, SWA the area of the ghost in monochromatic light (for the central wavelength of the central order), SWA Dia the diameter of the single wavelength ghost, SWR the intensity ratio of the SWA wrt to the feature causing the ghost. Ghosts are listed in decreasing order of values of PP.

To estimate the ratio NG/N of photons due to ghost and due to nominal spectrum in a pixel, we estimate the number of pixels 'interested' by the nominal spectrum as PXs ~1500*15*6=135000pxls (15 orders, on average each order 1500 pixel long, and the image being 6 pixels long on the slit). We assume the nominal spectrum is in total due to Nph photons; from the ghost data we calculate NG=ΣPP(s1,S2)*Nph and compare that with N=Nph/PXs, obtaining
NG/N=ΣPP(S1,S2)*PXs=1.7e-8*1.35e5=2.3e-3.
Therefore we can estimate that the percentage of photons in each pixel of the nominal spectrum due to camera ghosts would be of the order of 0.23%.
Looking at the single ghosts, some considerations may be done:

- The most important ghosts typically involve detector and/or filter
- There are not point-like ghosts: the smallest ghost may have for a given single wavelength a diameter of 95 pixels (detector-l1s2), causing a ghost of intensity of the order of SWR=1E-6 of the feature causing the ghost itself
- There are some quasi-pupil ghosts (e.g. detector F-s1), but they seems not to create particular sky concentration
- Three ghosts are not present, because no ray arrives to the detector

6.5.2 Single bounce

To check if a single reflection on the Collimator lens or on the prisms could arrive directly on the detector, we realized a Zemax Non-sequential Model of the NIR spectrograph (Figure 97). In the model some 'raw' baffles have been added, only to ensure that no 'trivial' path may arrive directly on the detector.

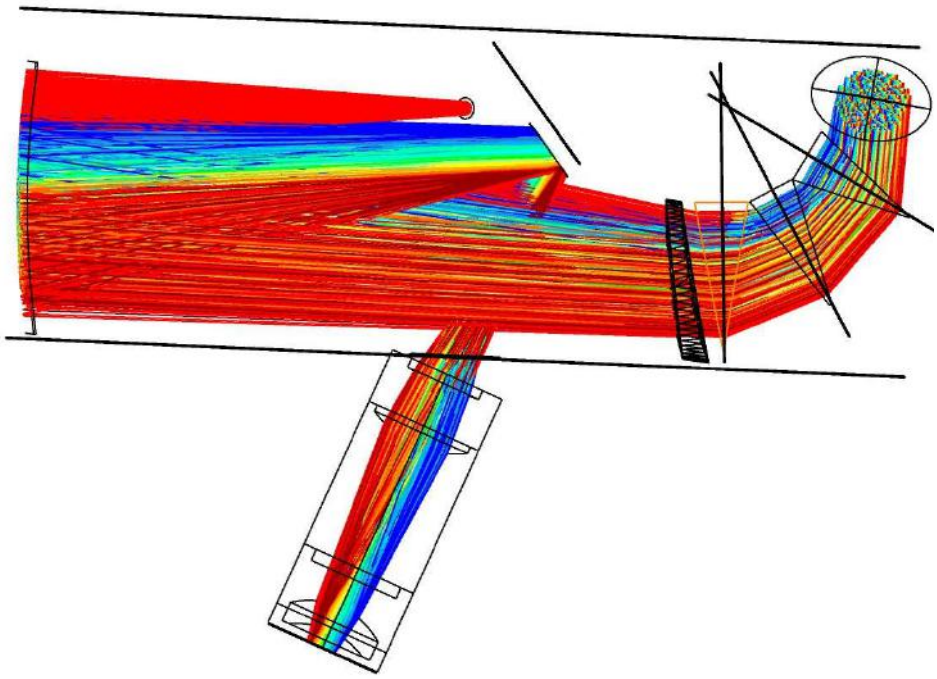

Figure 97: layout of the Non Sequential Model (only nominal path is shown).

Figure 98 shows that no ray due to single reflection on Prisms and Corrector Lens surfaces is able to

get directly to the detector.

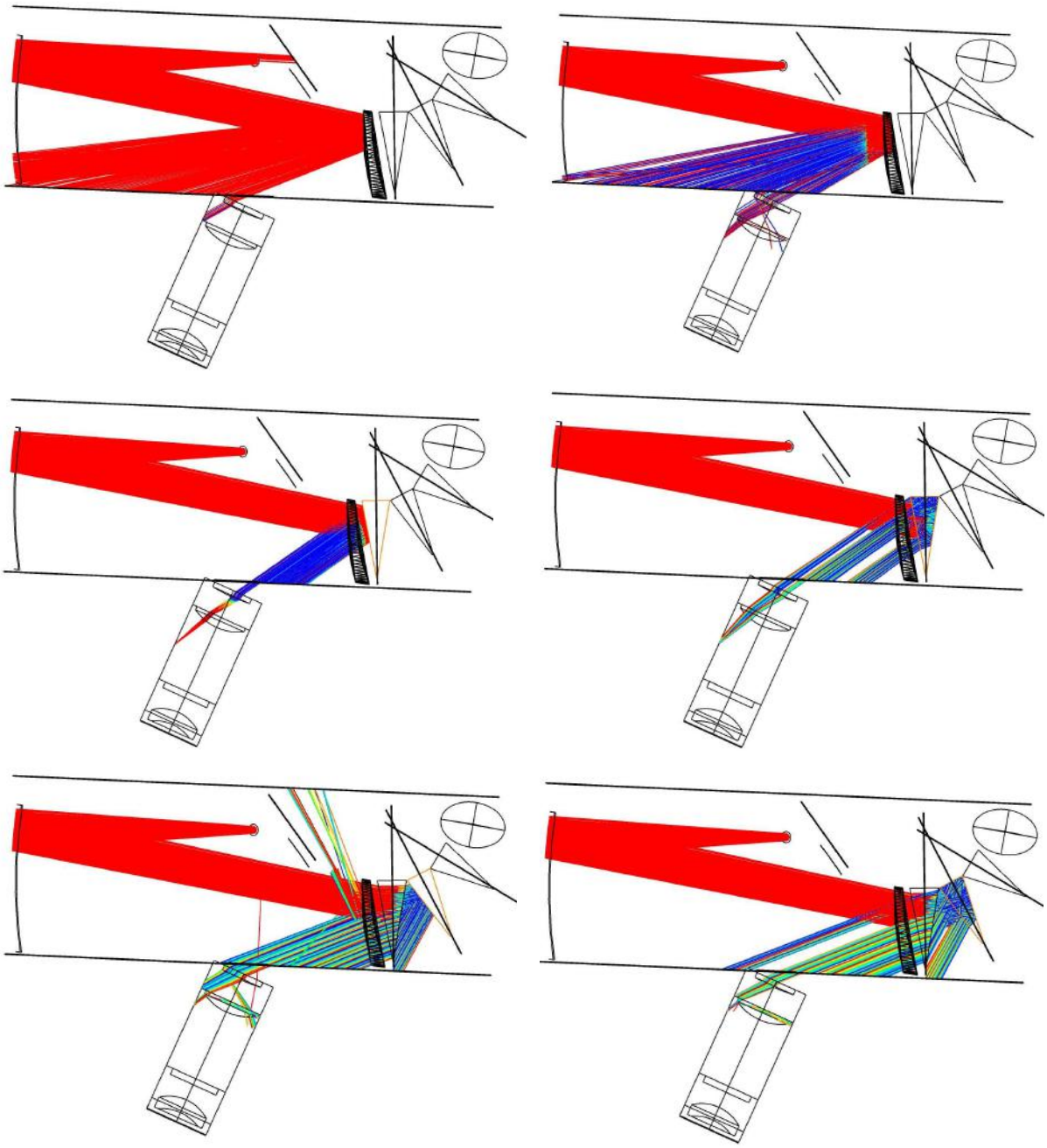

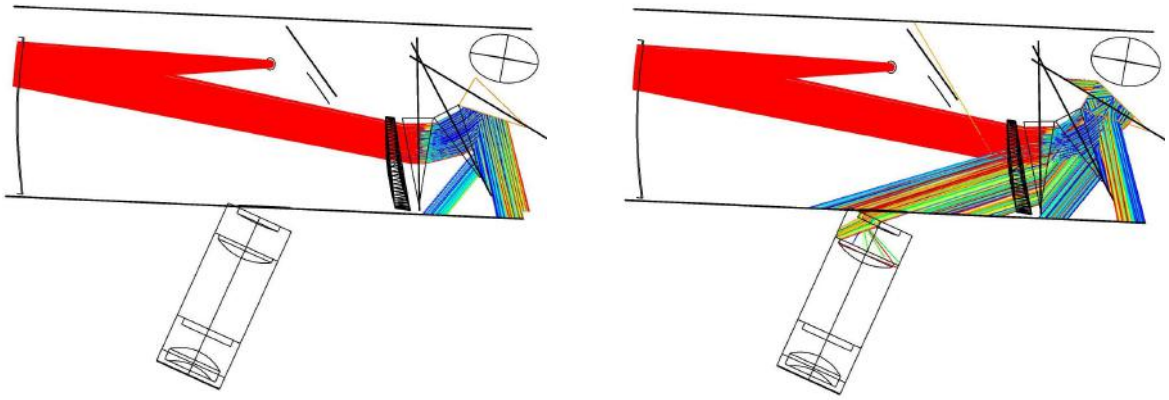

Figure 98: single reflections on Corrector Lens (first row panels) and Prisms surfaces (2nd,3rd and 4th rows panels).

6.5.3 Prism and Collimator Lens Ghosts

As previously mentioned, the complete Non Sequential (NS) model was used to perform an evaluation of all ghosts of the system.

The model has been fed with a source of 1W of power, monochromatic @1.0 µm (the wavelength that will more or less be imaged at the center of the detector) Reflectivity and transmissivity properties adopted are R=0.02 for all surfaces, R=0.15 for the detector, mirrors are perfectly reflective. The source had 1e5 rays, and they were allowed to split on every transmissive surface, dividing energy among child rays consistently with values of R and T. A ray was terminated when reaching an energy less than 1e-4 times the initial, essentially permitting double bounces on surfaces with R=0.02. The used detector is 10% oversized with respect to the nominal one, and has 2000x2000 pixels (each model detector pixel corresponds roughly to a real pixel).

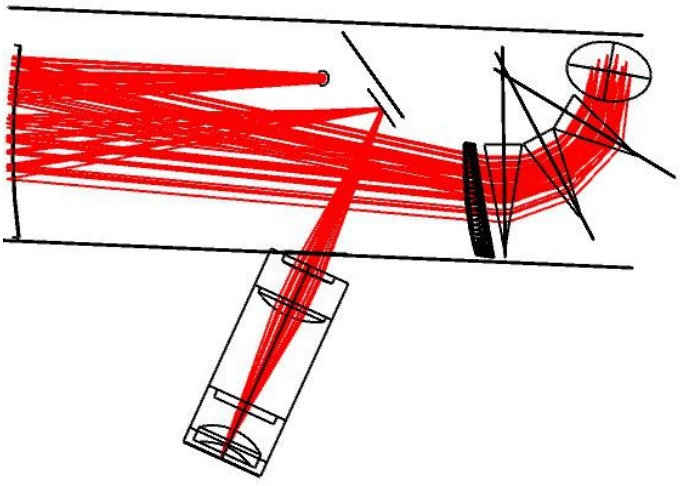

Figure 99: Nominal system fed with monochromatic source.

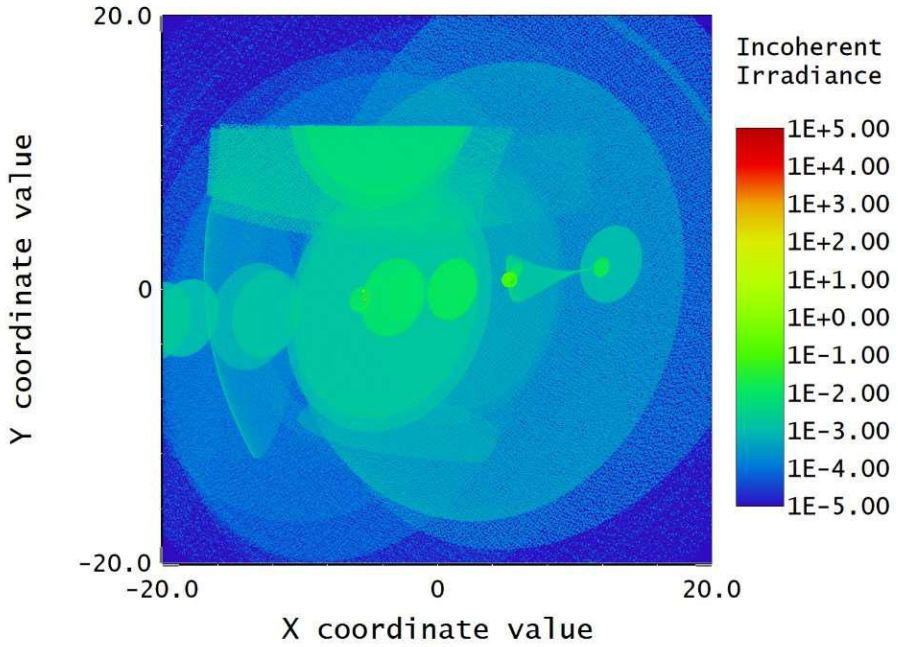

Detector Image: Incoherent Irradiance	
02/04/2018 Detector 63, NSCG Surface 1: Full Field Size 40.000 W X 40.000 H Millimeters, Pixels 2000 W X 2000 H, Total Hits = 2881793 Peak Irradiance : 1.0363E+04 Watts/cm^2 Total Power : 4.3200E-01 Watts Database:t1e5.ZRD	Zemax Zemax OpticStudio 16.5 180228_NIR_perns-NONSEQ2.zmx Configuration 10 of 15

Figure 100: Irradiance in logarithmic scale of nominal image and ghosts.

In Figure 100, the irradiance in W/cm^2 on the image plane is presented in logarithmic scale. Given the T and R values used, the total power obtained -(0.43W) is compatible with what is expected (0.85*0.98^24=0.52).

The peak irradiance (I=3.62e4W/cm^2) is due to the nominal image, and the nominal image is barely visible at the center of the detector, due to the small size of the pixel.

In Figure 101 and in Figure 102 the irradiance due to ghosts only is shown, both on the complete detector as zoomed on a zone where some point-like ghosts are present. These ghosts are due to reflective polished borders of the prisms: if we change the parameters of these surfaces in the simulation, using an absorbing coating, these ghosts disappear as shown in Figure 103 and Figure 104. Obviously, a completely absorbing coating is not possible, but good results may be obtained blackening ground surfaces (to diminish the intensity and spread out the area of the ghost).

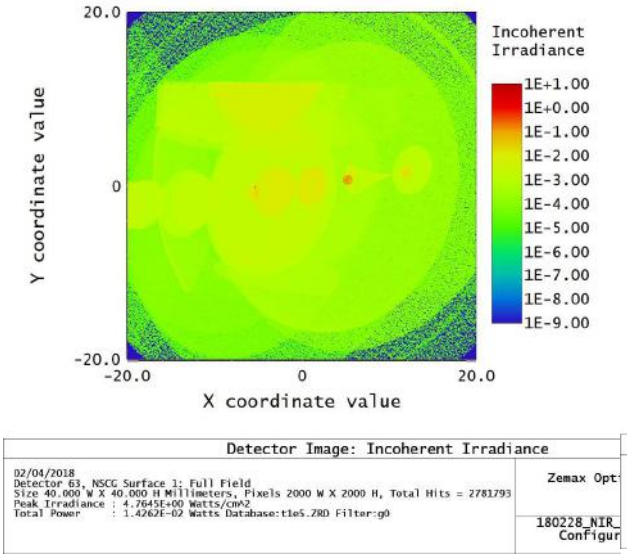

Figure 101: Irradiance due to ghosts only.

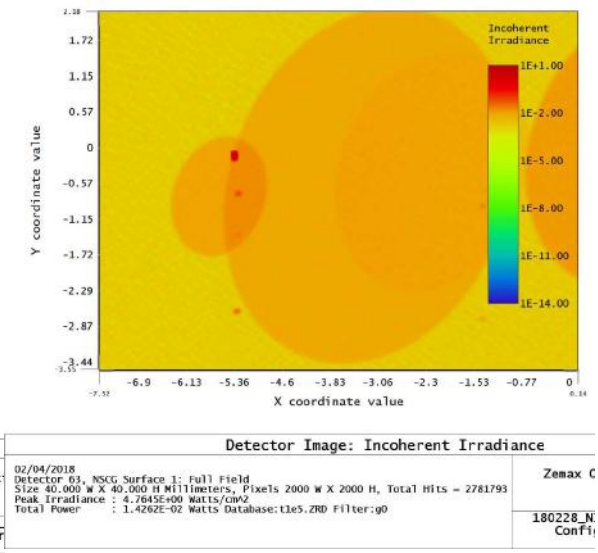

Figure 102: Zoom on pointlike ghosts.

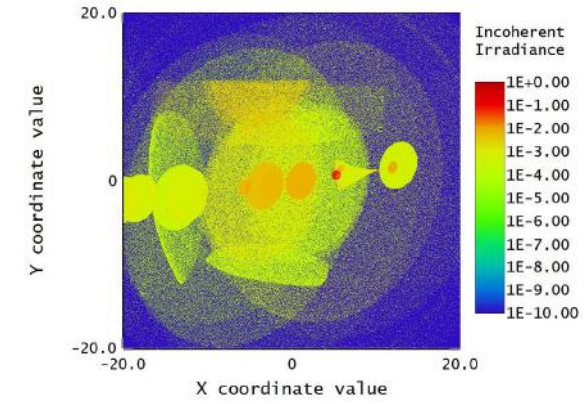

Figure 103: Irradiance due to ghosts using absorbing borders of prisms.

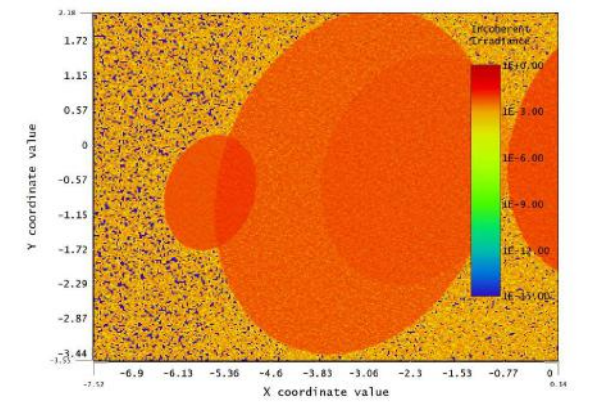

Figure 104: Zoom showing the absence of pointlike ghosts when prisms borders are blackened

6.5.4 Baffling

A complete baffle system is foreseen for the NIR spectrograph.

The geometrical shape of the Common Path suggest that no direct path (zero order) may reach the NIR window.

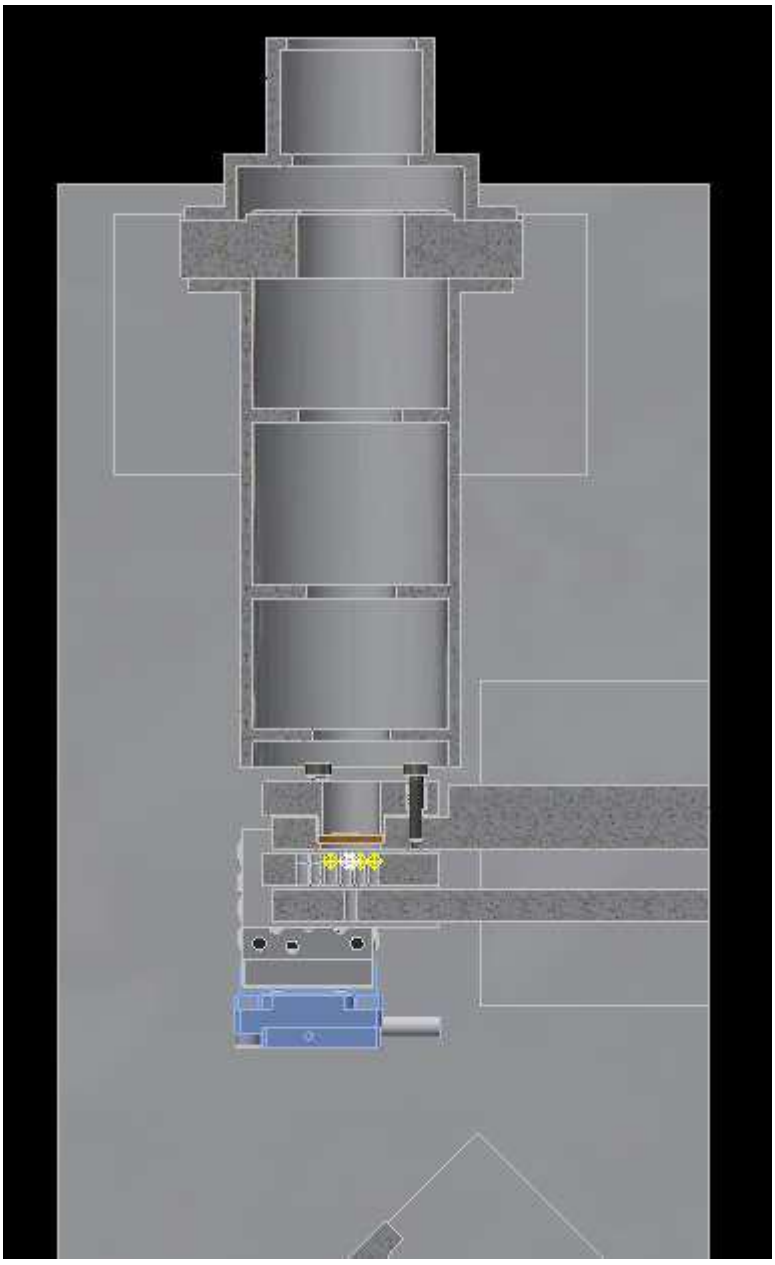

Figure 105: Baffle at the entrance of the NIR spectrograph, surrounding last part of the NIR CP, down to the slit assembly.

Nevertheless, a cold baffle with vanes, comprising the last part of the NIR CP, down to the NIR spectrograph slit, is foreseen.
The rest of the spectrograph will be similarly 'boxed' in cold baffle assemblies that will accommodate walls to separate the collimator from the prisms and the grating, and from camera (see Figure 106).

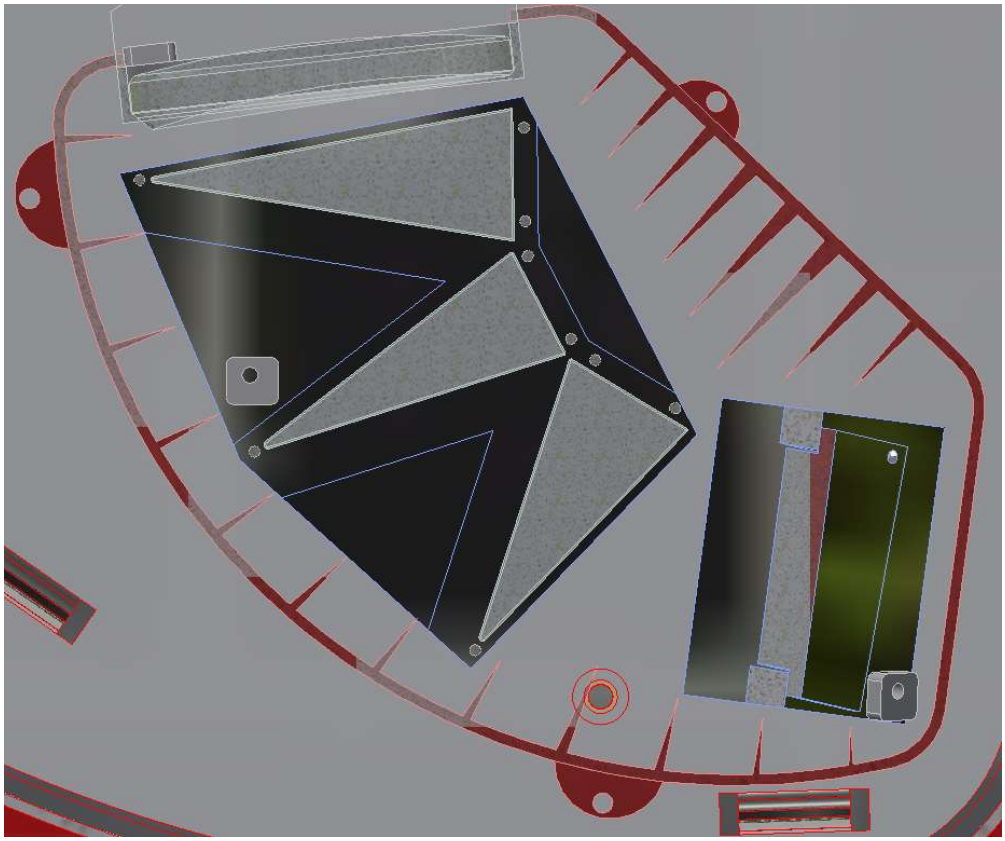

Figure 106: 'Baffle box' including the collimator lens, the prisms and the grating.

The camera itself will be baffled by a two-stage tube, Figure 107. Part one, approximately from the first lens to the filter, kept at 150K, part two, from the filter to the detector, at the same temperature as the detector (40K).
All baffling elements will be painted black with materials suitable for IR use.

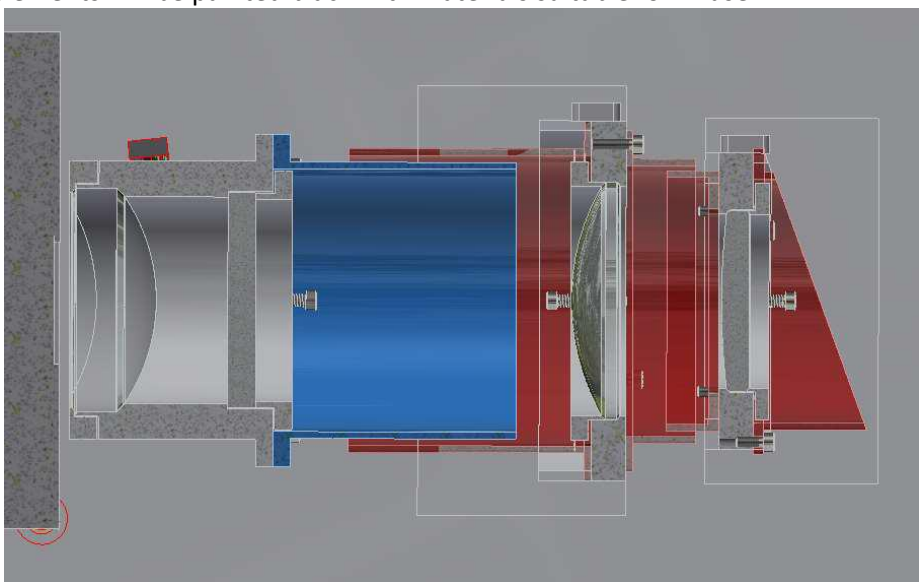

Figure 107: Camera baffle: a colder (blue, 40K) part shields the last elements of the camera (Filter and last lens) and is inserted (without thermal contact) inside the hot baffle (red, 150K), shielding the remaining elements of the Camera.

7 Acquisition Camera

7.1 Overall description

The Acquisition Camera (AC) system is an essential tool with different functions, e.g. light imaging, acquisition of the target for the spectrographs, monitoring of spectrographs co-alignment, etc.
It consists of a CCD camera, focal reducer optics, filter wheel, folding mirror and a mirror carriage.
At the level of the Nasmyth focal plane, a linear stage (see Figure 108) carries a single mirror with three positions for different functions and a pellicle beam splitter. The mirror and the pellicle are tilted at 45deg and direct light from the sky or from the slits, respectively, to the camera optics.
A refocuser linear stage is foreseen at the level of the first collimator lens.

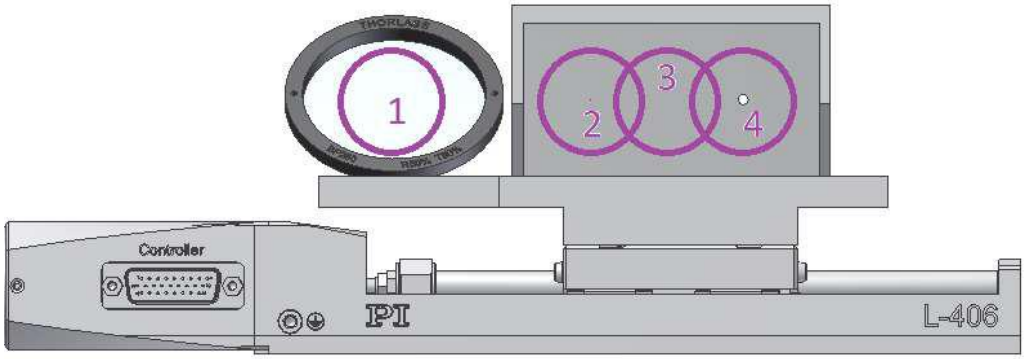

Figure 108: AC selector system. A PI DC motor stage with 102mm stroke (PI L-406.40DD10).

The main components of the AC system are described below, along with the corresponding functions:

- **Slit viewing pellicle beamsplitter star (Pos. 1 in** Figure 108**):**
  A semitransparent pellicle beamsplitter inclined towards the spectrographs allows using the AC system as a slit viewing camera (with calibration lamp on).
  Selecting different filters, one is able to use the AC system as a selective on-slit viewer.
  During daytime, visual co-alignment of the slits could be possible by illuminating them with the calibration lamp through the pellicle beamsplitter.
- **A flat 45° mirror with 3 positions:**
  a. **Artificial star (Pos. 2 in** Figure 108**):**
  The position is only used during daytime maintenance.
  A 0.5" reference pinhole acts as an artificial star by switching on the calibration lamp. Its proper centering in the spectrograph slits is verified with the science detectors. The pinhole is also visible on the AC and its position is recorded by the software as the reference for object centering.
  b. **Acquisition and Imaging (Pos .3 in** Figure 108**):**
  The full field is reflected towards the AC. A complete broad-band filter set is available to aid during object acquisition and identification.
  c. **Monitoring-Spectroscopy (Pos. 4 in** Figure 108**):**
  During the science exposure, the 45deg mirror is shifted to place a hole on the optical axis. This passes an unvignetted field of 15arcsec (corresponding to 2.805mm) to the spectrograph slits.
  On the AC it is possible to recover the peripheral field, but with a hole in the center.
  Off-axis secondary guiding on an object in the periphery would be possible during science exposure.

7.2 Detector System

A survey among manufacturers indicates the Andor iKon m934 as a possible detector for the AC. The model using the CCD sensor BEX2-DD assures a broadband coverage and a high NIR QE.

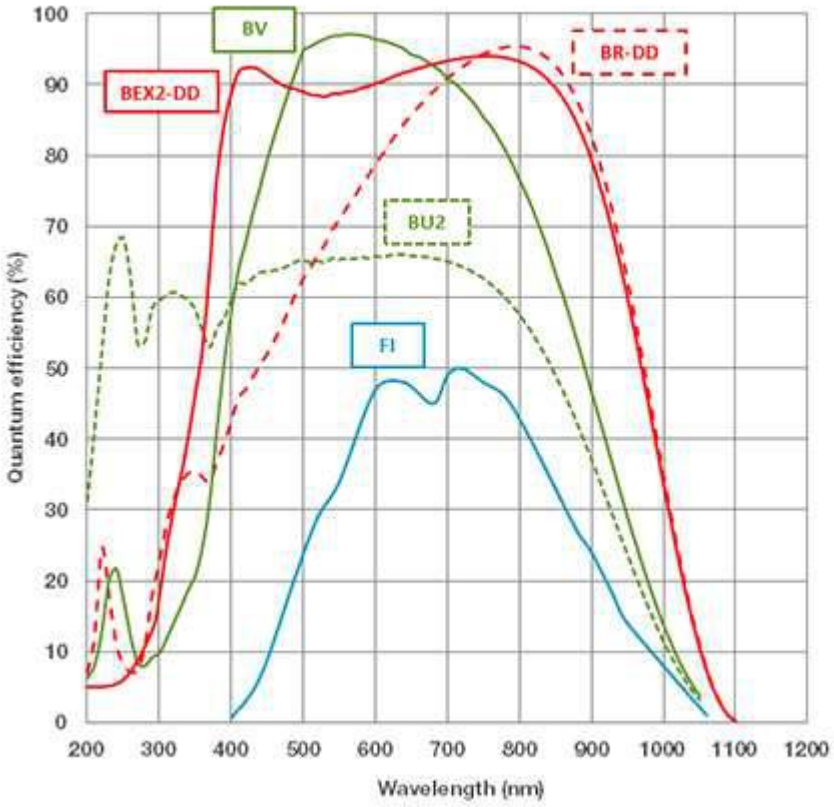

Figure 109: Quantum Efficiency for different models of the Andor iKon-M934 taken from the Andor website.

The following table reports the main characteristic taken from the the Andor iKon-M 934 datasheet:

Feature	Value
Active Pixels	1024 x 1024
Pixel Size	13.0 µm
Sensor Size	13.3 x 13.3 mm
Sensor Option	BEX2-DD: Back Illuminated, Deep Depletion with fringe suppression, extended range dual AR coating
Active area pixel well depth	130000 e
Pixel readout rates (MHz)	5, 3, 1, 0.05
Read out noise	2.9 e
Dark current	0.00012 e/pixel/sec at -100deg
Frame rate	4.4 fps (full frame)
Maximum cooling	-100 deg

Table 41: Andor iKon-M 934 main characteristics.

7.3 Optical Design

The following general requirements concerning the design and the performance of the AG system have been specified. The AC system shall:

- Ensure a Field of View of at least 2 arcmin x 2 arcmin (up to 4 arcmin x 4 arcmin)
- Detector wavelength range shall extend up to 1.0-1.1 µm with acceptable QE (>20%)
- Allow to visually detect and to obtain centroid position of object in u, g, r, i, z (Sloan) band and Y, V (VIMOS) band.
- Have a good image quality (with a scale smaller than 1 arcsec /1 pixel)
- Use a 13.0 µm, 1024x1024 pixel detector CCD optimized for NIR QE.

Given these requirements, the obtained design is illustrated in Figure 110 and Table 42.
The largest Field of View that does not compromise the image quality was found to be 3.5x3.5 arcmin (linear), resulting in a pixel scale of 0.205 arcsec.
After the 45deg mirror, a lens of 60 mm diameter reimages the pupil onto a compact camera. In front of the camera there is a filter wheel, illustrated by a single plane glass in Figure 110.
The subsequent camera, formed by 2 doublets and two singlets of max diameter 28 mm, relays the Nasmyth focus on the detector, with an F/#=3.6.
The total length from focus to focus is 434.15 mm. The glasses are selected to provide color correction over a wide wavelength range.

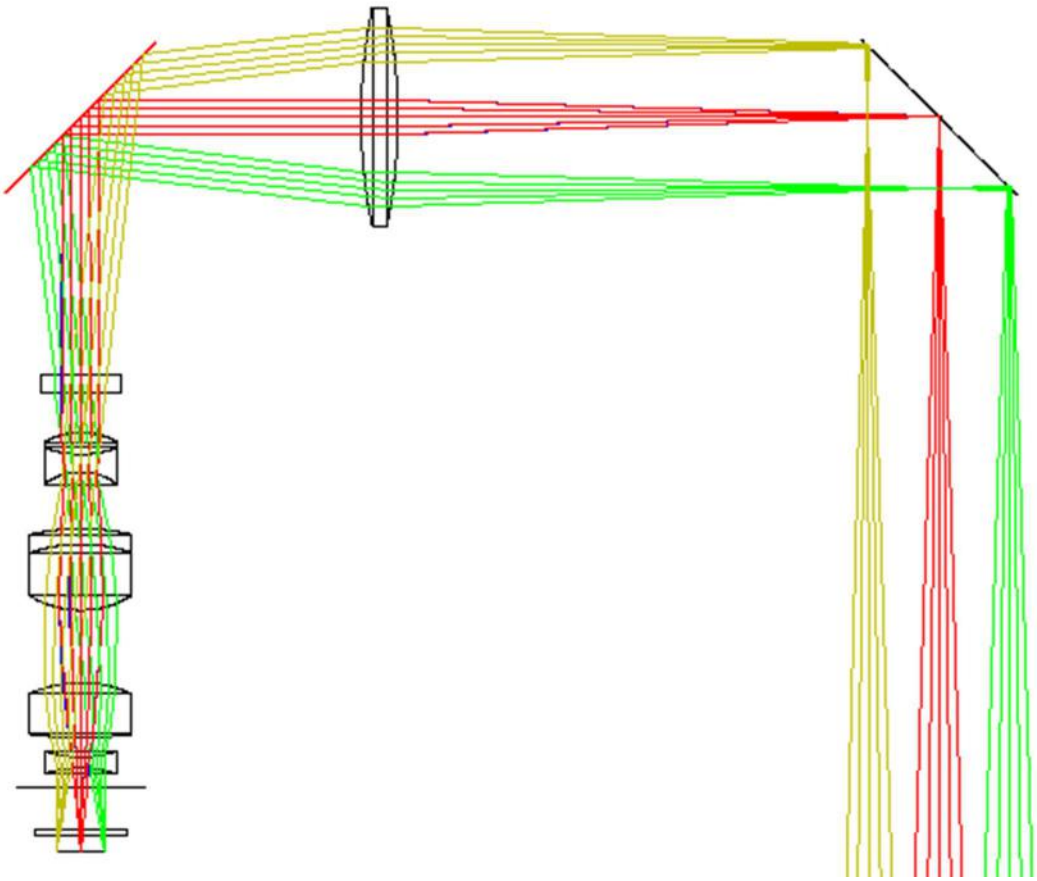

Figure 110: AC camera design.

Description	Radius [mm]	Distance[mm]	Material	Diameter [mm]
Telescope Focus	-	147.66		60.00
L1	150.902	10.00	CAF2	60.00
	-147.935	76.50		60.00
Mirror	-	0.000		58.00
		-70.00		
Filter	-	-5.00	N-BK7	22.00
		-10.97		
D1	-20.115	-6.00	CAF2	20.00
	26.793	-4.82	BAL15Y	20.00
	-16.688	-15.42		20.00
D2	-61.274	-4.22	PBL25Y	28.00
	-42.574	-18.00	CAF2	28.00
	26.406	-19.74		28.00
S1	-32.969	-15.01	BAL35Y	28.00
	105.709	-5.31		28.00
S2	29.584	-3.00	BSL7Y	20.00
	-31.441	-5.00		20.00
		-11.85		
S3		-1.50	SILICA	25.40
		-4.15		
Focal Plane	0.00000	0.00		13.00

Table 42: AC elements data.

7.3.1 Image Quality

Spot diagrams are reported in Figure 111 and encircled energy in Figure 112, showing that the spot is contained in a box of 2x2 pixels (26.0 µm). Plotted field positions correspond to center of the field, center of the sides of the 3.5 arcmin and the position along the diagonal corresponding to a 3.75 arcmin diameter, for which the quality is still good.

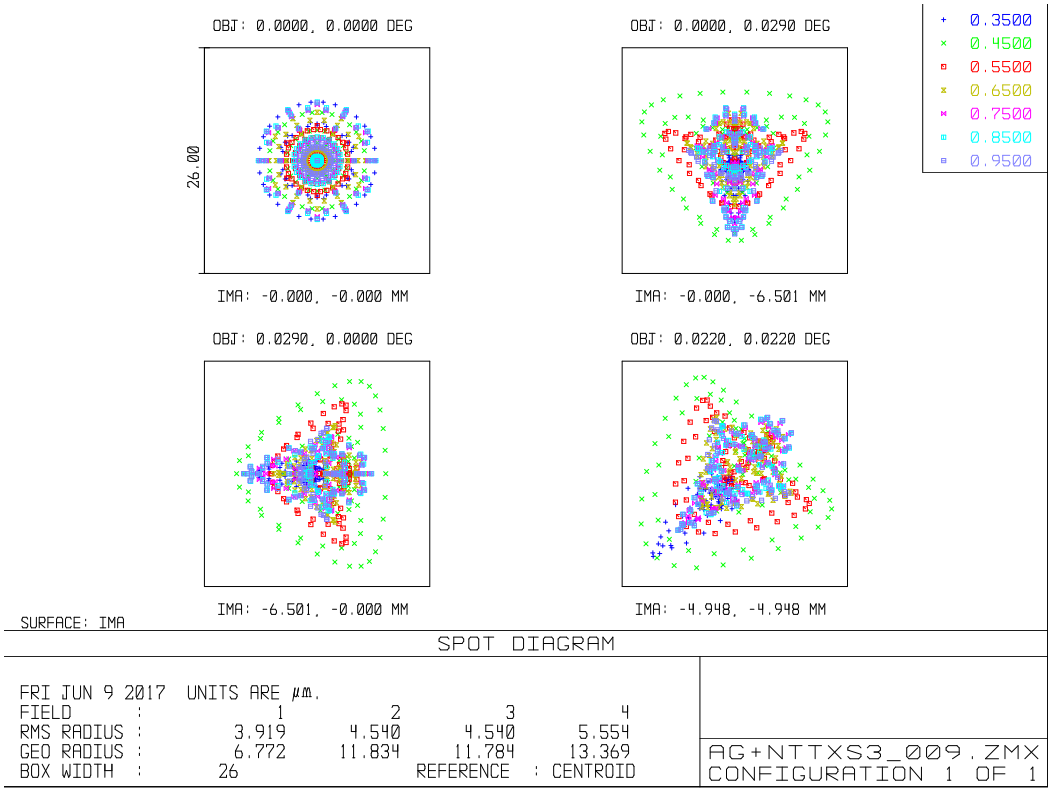

Figure 111: AC spot diagrams.

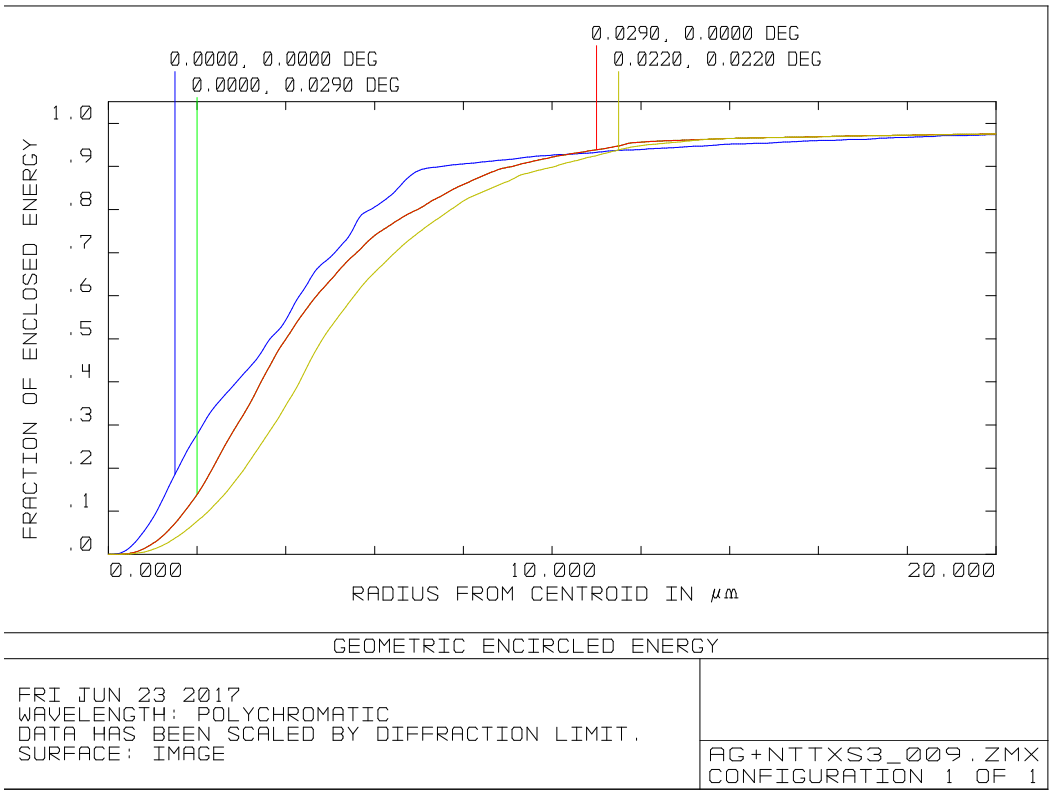

Figure 112: AC Encircled Energy.

7.4 Footprints

In the following images, the footprints on the AC system elements are plotted. Different colors represent different positions in the field. (center, upper and lower edges).

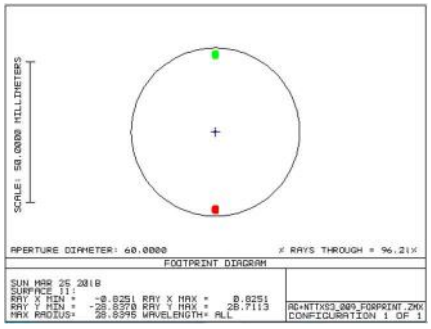

Footprint on Selector Mirror

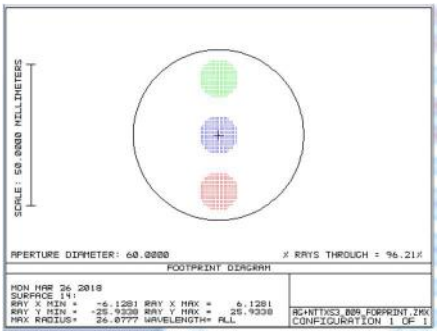

Footprint on Collimator Lens

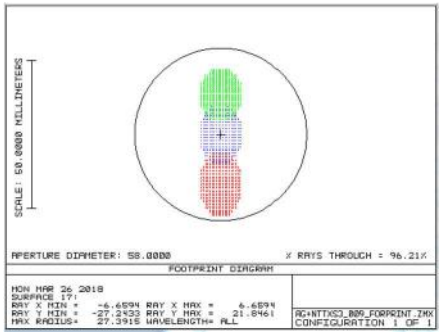

Footprint on Folding Mirror

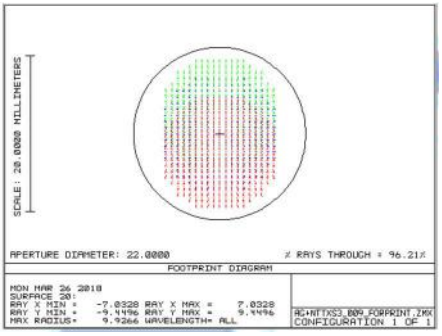

Footprint on Filter

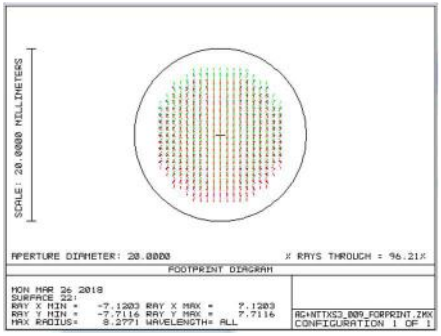

Footprint on Doublet1

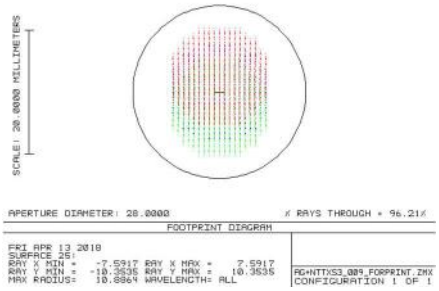

Footprint on Doublet2

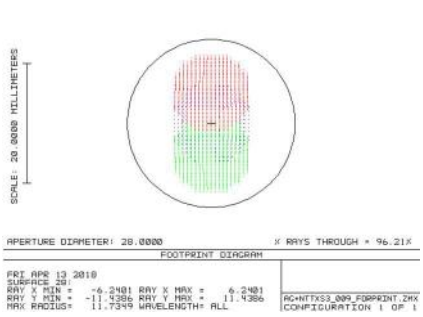

Footprint on Singlet1

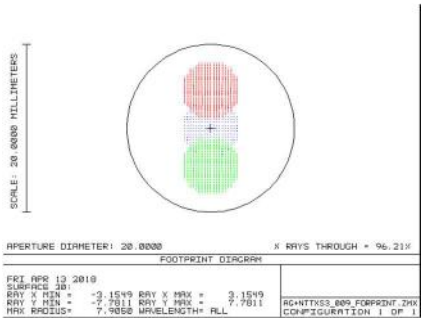

Footprint on Singlet2

Figure 113: Footprint on the different optical elements of the AC System.

7.5 Tolerance analysis

A tolerance analysis has been performed on the AC system.
As merit figure, we have adopted the spot RMS radius with a value of 5.0 µm for the nominal design.
The position of the focus has been adopted as compensator.
Adopted errors on positioning:

- 50 µm on decentering (40 µm for the 2 doublets)
- 0.05 degrees tilt for all the elements

Error due to manufacturing:

- Radius of Curvature (or planarity) 1 fringe
- Surface irregularity: +/- 1 fringe (@633nm)
- Thickness 50 µm
- Glasses: Index of Refraction +/- 0.5e-4, Abbe Number 1%
- Elements surface mutual positioning 50 µm on decentering
  (40 µm for the 2 doublets)
  0.05 degrees tilt for all the elements

A first sensitivity analysis showed that the worst offenders (see Table 43) are the element and surface decentering of the 2 doublets, both in terms of alignment and manufacturing.

Element	Value	Merit F
Doublet 1 Surface x-dec	+/- 40 µm	0.0034
Doublet 1 Surface y-dec	+/- 40 µm	0.0034
Doublet 2 Element x-dec	+/- 40 µm	0.0025
Doublet 2 Element y-dec	+/- 40 µm	0.0025
Doublet 2 Surface x-dec	+/- 40 µm	0.0020

Table 43: worst offenders list.

To better estimate the combined effect of all errors, 100 Montecarlo (MC) realizations have been run and statistical results are shown in Table 44.
The MC analysis shows that at 90% of the realizations, RMS spot radius is around 0.2 arcsec.
Max compensator displacement is +/-0.3mm.

Percentage	MF (mm)
90%<	0.0133
50%<	0.0100
10%<	0.0072

Table 44: 100 MC realization statistics for AC system.

Assigning looser tolerances for the element and surface centering of the two doublets (50 µm on decentering) and keeping unchanged the other parameters, the Montecarlo analysis results in:

Percentage	MF (mm)
90%<	0.0152
50%<	0.0111
10%<	0.0072

Table 45: 100 MC realization statistics for AC system with looser tolerances.

7.6 Thermal analysis

The system has been designed at 10 °C. A change of +/-10°C causes a deterioration of the image (see Figure 114), anyway always with a geometrical dimension of about 2 pixel (26.0 µm). The optical quality may be completly recovered focusing the camera or moving the collimator lens (S1).

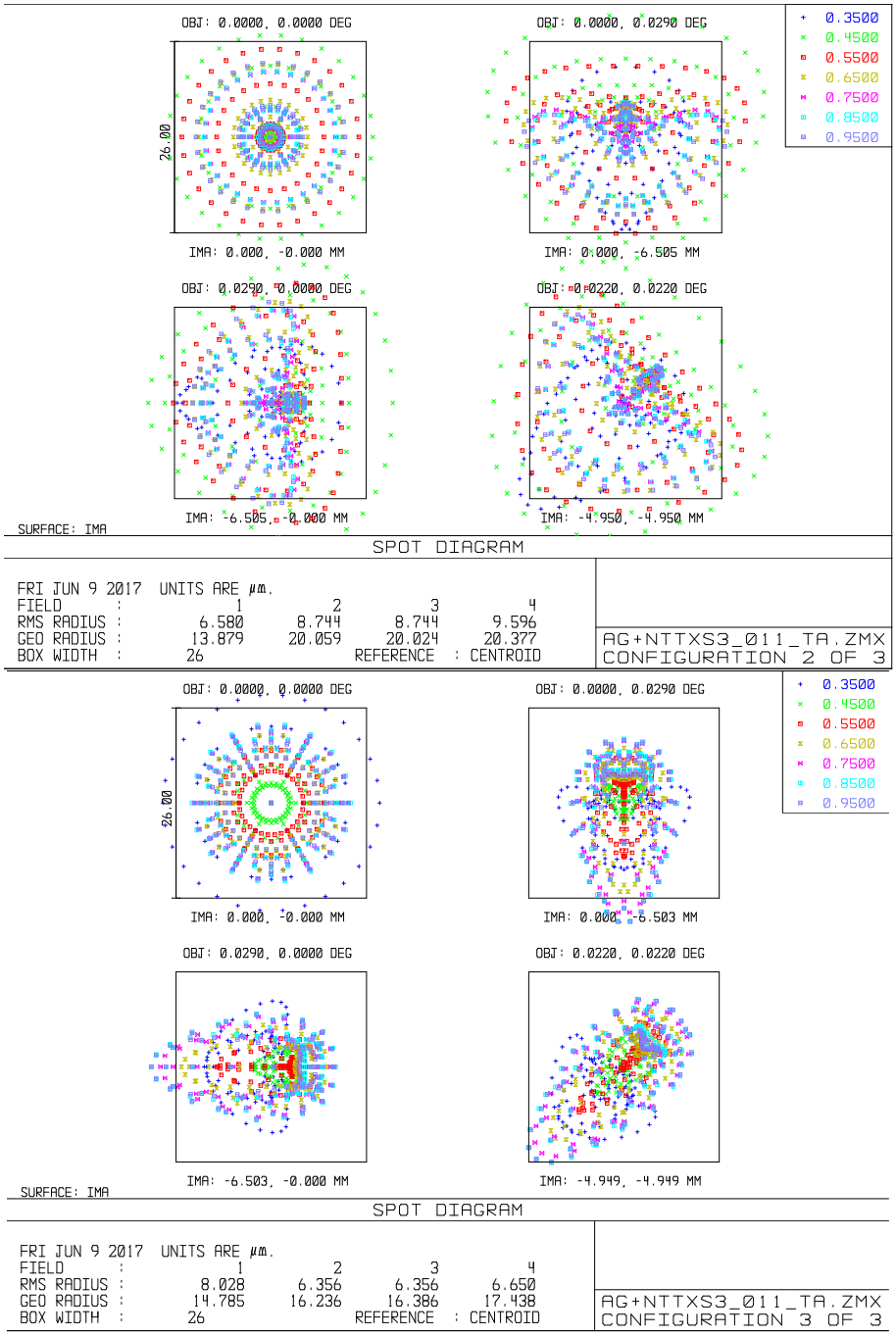

Figure 114: Spot diagrams for temperatures of 0° and 20°.

7.7 Throughput

In this section we give an estimate of the AC system throughput (Table 46) from the 45deg mirror down

to the detector. Optics efficiency is estimated using elements bulk material absorption (Zemax) and following the general indications reported in paragraph 6.2.7.
In Figure 115, transmissivity of AC glasses is reported.

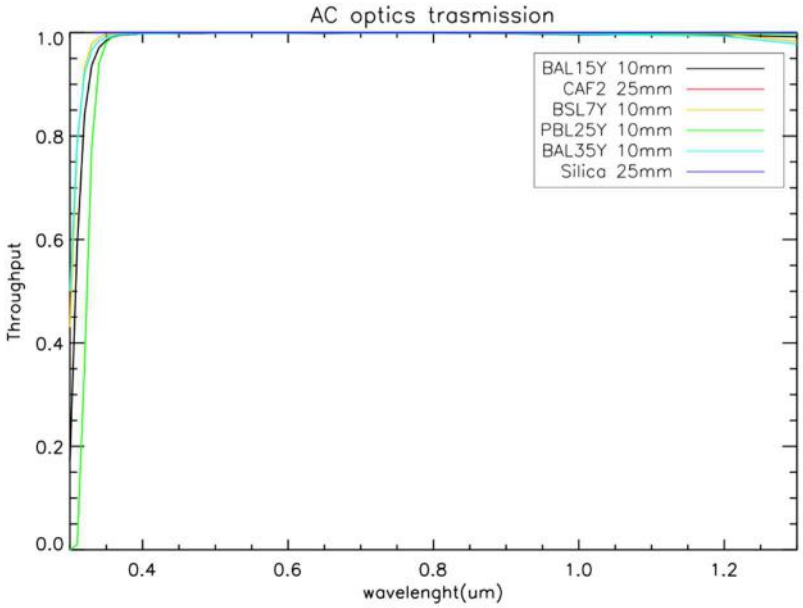

Figure 115: AC Glasses transmissivity.

Element	T
Telescope	**0.51**
45deg Selector Mirror	**0.99**
Collimator Lens	**0.98**
Transmission	1.00
AR Coating	0.98
Folding mirror	**0.99**
Filter Wheel	**0.98**
Camera	**0.57**
1st Doublet	0.89
AR Coating	0.98
2nd Doublet	0.85
AR Coating	0.98
1st Singlet	0.89
AR Coating	0.98
2nd Singlet	0.90
AR Coating	0.98
Detector Window	**0.98**
Transmission	1.00
AR Coating	0.98
TOTAL	**0.27**

Table 46: AC total throughput.

7.8 Sensitivity Prediction

The analysis of the expected performances for the AC has been done using a set of VIMOS and SDSS filters in the computations. The calculation has been made using an adapted version of the algorithm from[RD14], using the parameters summarized in Table 47.

Parameter	Value	Unit
Telescope Aperture	350	cm
Diameter of Secondary Mirror	87.5	cm
Number of Mirror surfaces	5	
Number of lenses in light path	5	
Pixel scale	0.20	arcsec/pixel
RON	2.9	electron
Number of exposures	1	
Airmass	1.15	
FWHM seeing disk diameter at zenith	0.8	arcsec
Temperature	10	C
Relative Humidity	10	%
Observatory	La Silla	
Phase of the Moon	New	

Table 47: General Parameters for Sensitivity Prediction.

The filter peak transmission has been considered to be 80.0% for all the photometric bands, while the quantum efficiency of the detector is taken from the Andor I-Kon M934 datasheet (see Table 47).

The computation of the limiting magnitude as function of the exposure time has been done for SNR=10. The results are reported in the following tables.

VIMOS Band (Wav)	1 sec	2 sec	3 sec	5 sec	10 sec	15 sec	20 sec
U (365nm)	16.9	17.7	18.5	18.7	19.4	19.7	20.1
B (440nm)	19.2	19.9	20.4	20.8	21.5	21.8	22.0
V (550nm)	19.5	20.1	20.5	21.0	21.5	21.8	21.9
R (660nm)	18.9	19.6	20.05	20.4	20.9	21.1	21.3
I (810nm)	17.8	18.4	18.7	19.0	19.4	19.7	19.9

SDSS Band (Wav)	1 sec	2 sec	3 sec	5 sec	10 sec	15 sec	20 sec
u' (355.7nm)	15.9	16.7	17.5	17.7	18.4	18.7	19.1
g' (482.5nm)	18.2	18.9	19.4	19.8	20.5	20.8	21.0
r' (626.1nm)	18.0	18.6	19.0	19.5	20.0	20.3	20.4
i' (767.2nm)	16.4	17.1	17.5	17.9	18.4	18.6	18.8
z' (909.7nm)	15.3	15.9	16.2	16.5	16.9	17.2	17.4

Table 48: Limiting Magnitude for a SNR=10 in VIMOS and SDSS band.

8 Calibration Unit

8.1 Overall description

The calibration unit (CU) is used to provide calibration spectra for the SOXS spectrographs, which are necessary to remove instrument signatures and convert the observed spectrum into one with physical units (in wavelength and flux). Calibration spectra are generated using a synthetic light source, whose light is directed so to enter and to be dispersed by the spectrographs in the same manner, as light from a celestial object would be.

The light source takes form in an integrating sphere, equipped with lamps suitable for wavelength and flux calibrations across the full wavelength range of the instrument (350-2000 nm). The following lamps are used:

- Quartz-tungsten-halogen (QTH) lamp, for flux calibration 500-2000 nm (see Figure 104).
- Deuterium (D2) lamp, for flux calibration 350-500 nm (used simultaneously with QTH lamp for UV-VIS arm flux calibration) (see Figure 118).
- NeArHgXe penray lamps bundled together, for IR wavelength calibration. The individual lamps are controlled to operate together as one lamp (see Figure 119). (Note: can also function as UV-VIS wavelength calibrator.)
- ThAr hollow cathode lamp, for UVIS wavelength calibration. (Note: can also function as IR wavelength calibrator.)

These kinds of lamps are the same as the ones used in the XSHOOTER instrument. They occupy four ports of the calibration sphere, and at the exit port of the sphere, light is diffused in order to achieve uniform illumination at the slit plane. Lamps are placed around the integrating sphere's "equator", in a way that none of them is directly visible from the exit port at the "south pole" (see [RD1]).

Relay optics will be placed between the light source and telescope focal plane. In addition, a fold mirror will be placed in the light path to accommodate the optical design to the space and mechanical constraints. This relay system reimages the exit pupil of the integrating sphere to the focal plane, maintaining uniform illumination at the slit.

A stage-controlled calibration pick-up mirror is placed in the light path before the telescope focus, which enables the observer to switch the spectrograph input light between telescope and CU.

The CU is equipped with a pinhole mask mounted on a linear motor stage, located near the exit port of the integrating sphere. This enables the selection of output light between diffuse illumination and pinhole (star simulator).

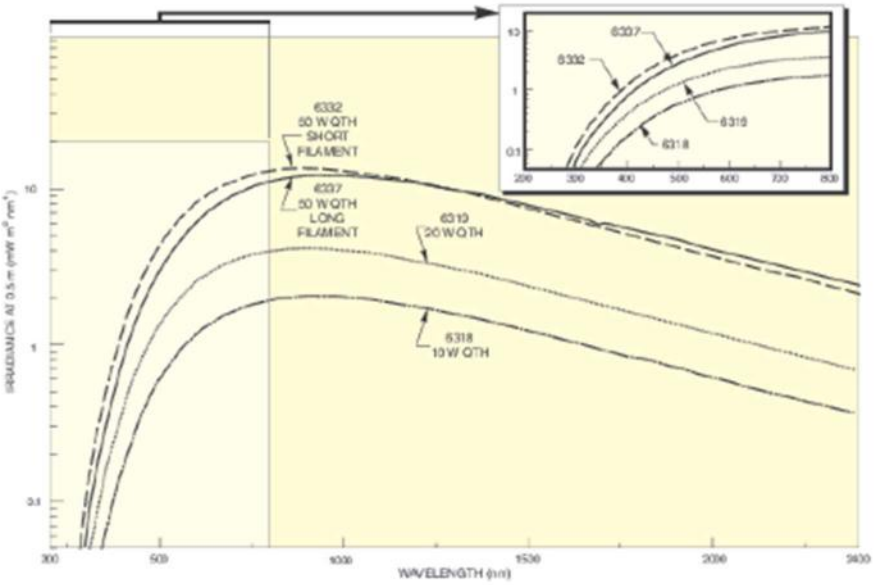

Figure 116: Typical QTH lamp spectral output. Note that the lamp still has flux at 350 nm, but a factor 10 fainter compared to the peak (Source: Newport).

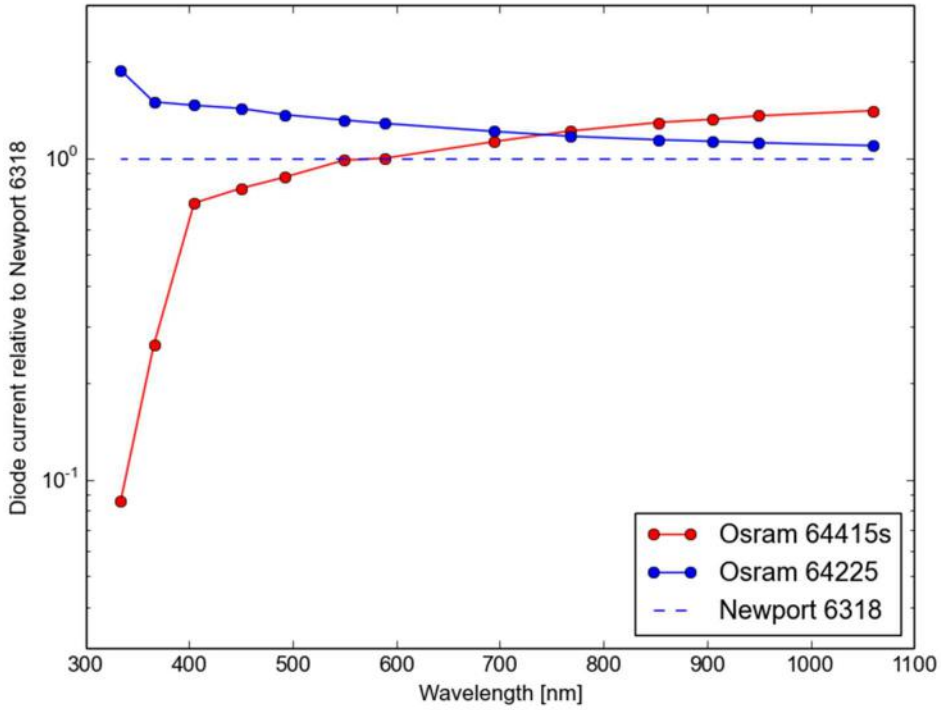

Figure 117: Relative comparison of spectral output of Newport 6318 QTH lamp (used in XSHOOTER, production discontinued), and suggested replacement Osram 64225 (Source: A. Sorensen, XSHOOTER).

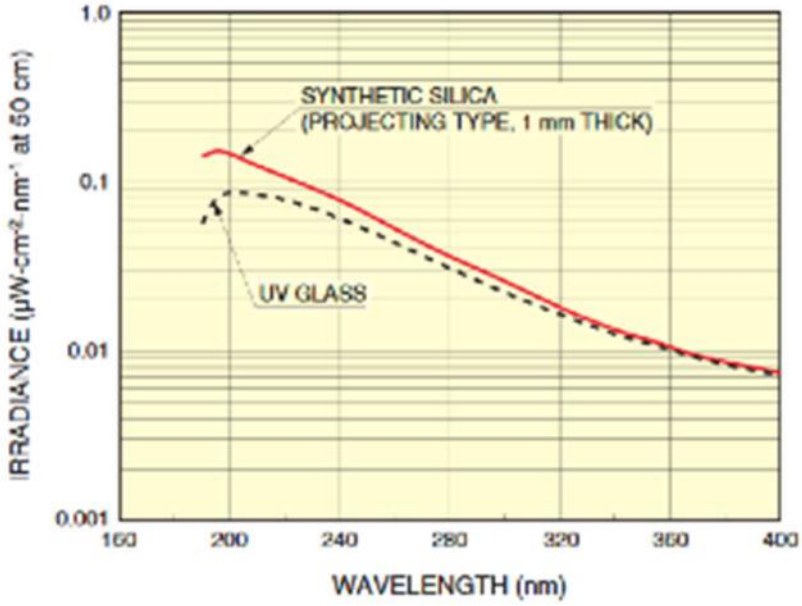

Figure 118: D2 lamp spectral output (Source: Hamamatsu).

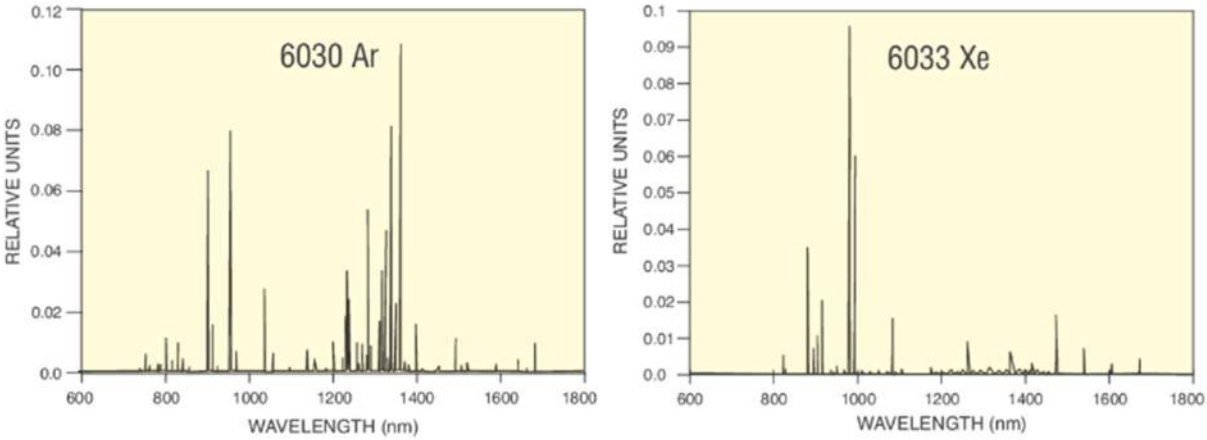

Figure 119: Penray lamp spectral output (only ArXe; source: LOT).

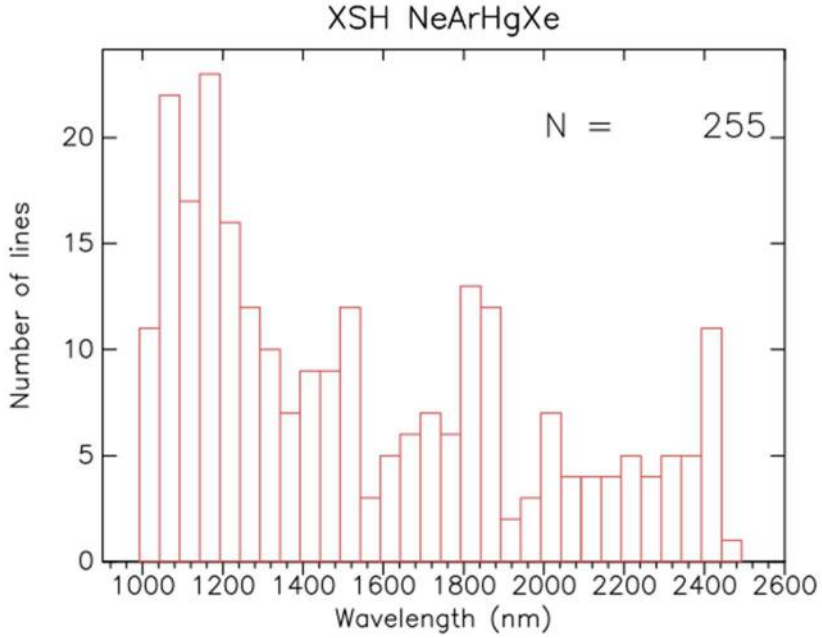

Figure 120: Histogram of XSHOOTER penray line density in the IR.

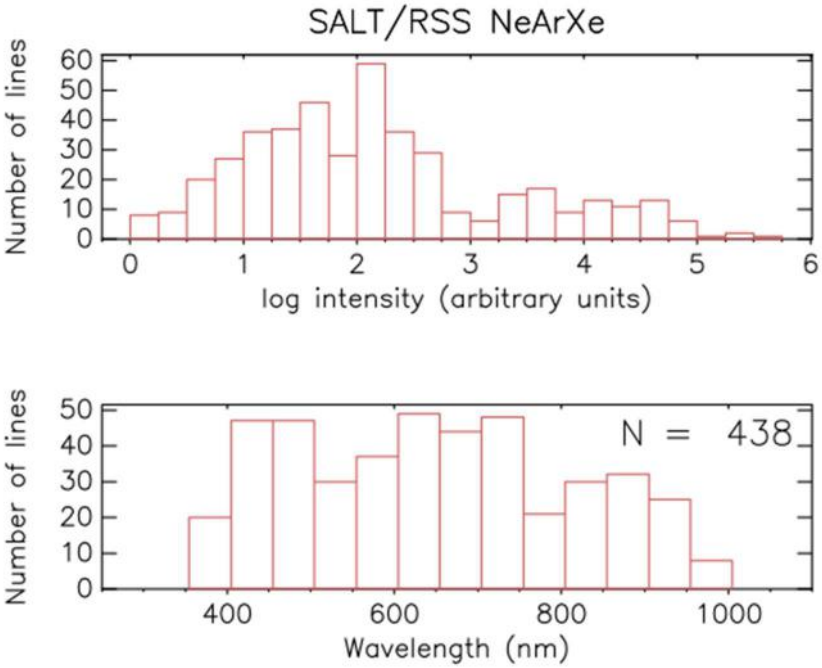

Figure 121: Histogram of penray line density and intensity in UVIS range (SALT/RSS penray).

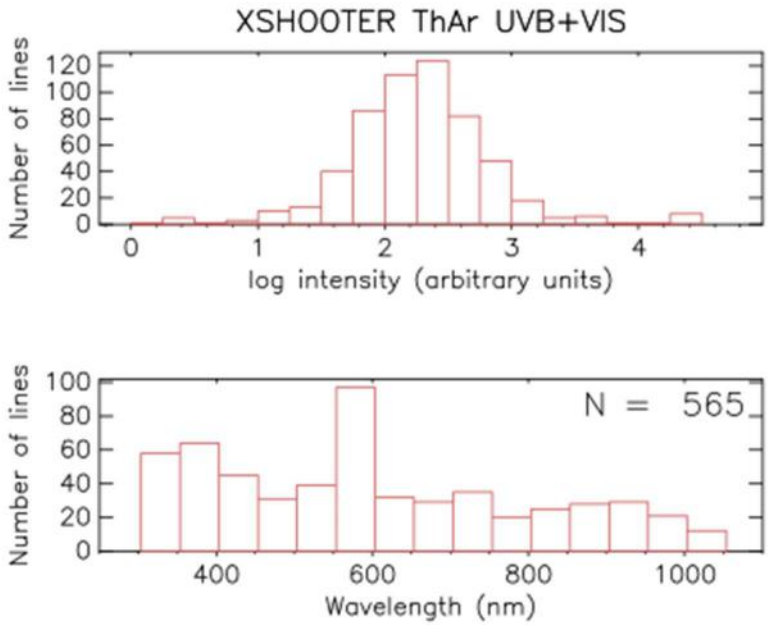

Figure 122: Histogram of line density and intensity in the UVIS, XSH ThAr lamp.

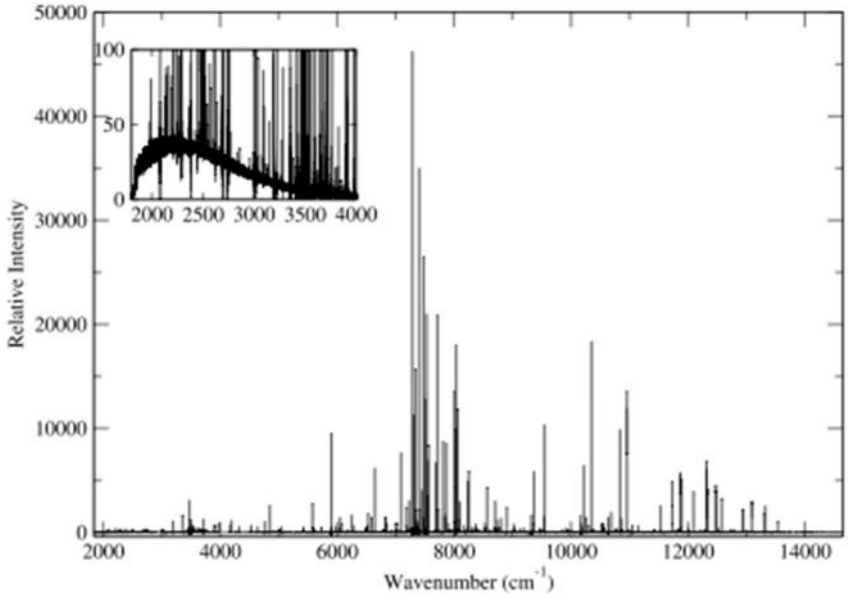

Figure 123: ThAr lamp spectrum in the wavelength range corresponding to 700-5000 nm (Kerber et al. 2008, ApJS, 178, 374).

8.1.1 CU Optical design

The optics relay the diffused exit pupil of the integrating sphere onto the telescope focal plane, while at the same time keeping the beam with the same f-number of the telescope (f/11 in the case of NTT). The whole slit length (12”, or 2.2 mm projected at the focus) must be illuminated uniformly.
Two custom-made CaF2 and fused silica singlets are used to relay the light from the diffuser to cover the slit length at the focal plane. The system fits inside a 150 mm x 150 mm box attached to the side of the common path (yellow rectangle in Figure 124).

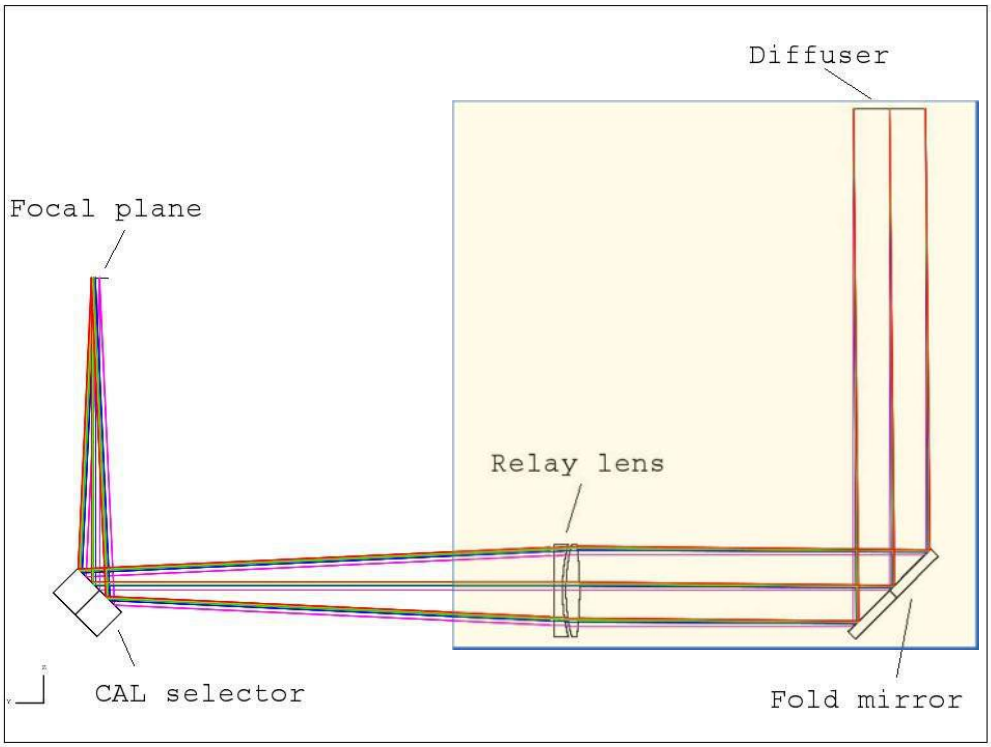

Figure 124: design of the CU optical system.

Relative illumination produced by the system at the focal plane show very little inhomogeneity (at the level of < 1%) across the slit, for both ends of the spectrograph wavelength range at 350 and1750 nm. The oversized 4.8 mm focal plane ensures that the slit (d = 2.2 mm) is completely covered, and provides more room for tolerancing and easier alignment.

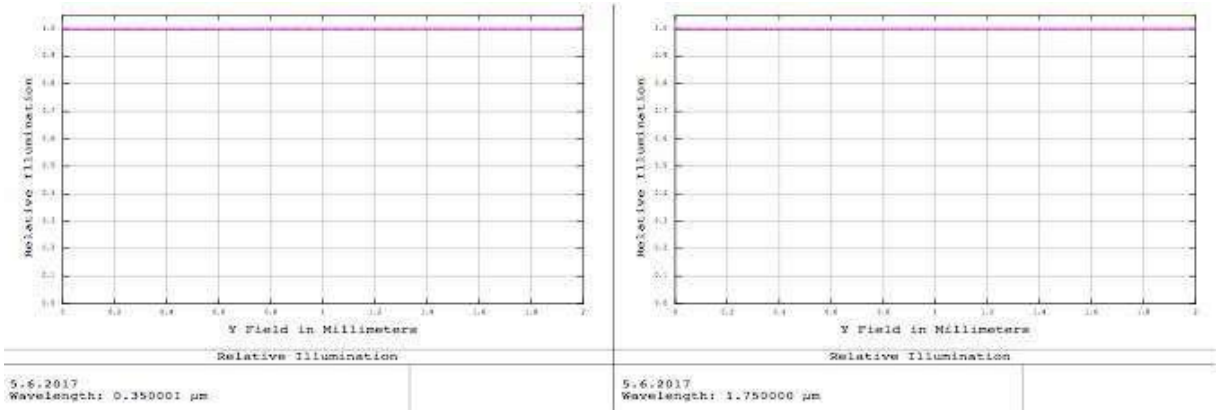

Figure 125: Relative illumination profile at the focal plane, for 350 and 1750 nm.

The design is also optimized in such a way that the axial image quality is kept high. This accommodates possible usage of pinhole mask for a synthetic point source inside the spectrograph. This pinhole can be inserted into the optical path before the first fold mirror.

Surf	Type	Radius[mm]	Thickness[mm]	Glass	Diameter [mm]	Comment
OBJ	STANDARD	Infinity	Infinity		0	
STO	STANDARD	Infinity	140		20.9	Diffuser
3	STANDARD	Infinity	0	MIRROR	34	Fold Mirror
4	COORDBRK	-	-90		-	
5	STANDARD	-111	-4	CAF2	28	
6	STANDARD	54.4	-1.027922		28	
7	STANDARD	53.3	-2.5	F_SILICA	28	
8	STANDARD	475	-1.15		28	
9	STANDARD	Infinity	-27		25.02019	Common Path
10	STANDARD	Infinity	-104		22.55693	
12	STANDARD	Infinity	0	MIRROR	18	CAL selector
13	COORDBRK	-	91		-	
IMA	STANDARD	Infinity			4.803526	Focal plane

Table 49: CU surfaces data.

8.1.2 Tolerancing

A preliminary tolerance analysis was performed on the calibration subsystem. The analysis considered positioning error of each component in the subsystem (entrance aperture, two lenses and aperture stop) and optical tolerances. The tilt mirror decenters were not considered as they translate to thickness tolerance. The full list of tolerance dimensions are listed below with their respective values. A merit function was used for compensation, as achromatic (560nm and 1250nm) axial RMS spot size was used as a criterion.

Prior element	Air Thickness [mm]	Axial decenter [mm]	Axial tilt [']
Diffuser	± 0.1	± 2	
Tilt Mirror	± 0.1	N/A	± 1
Lens 1 (positive)	± 0.05	± 0.03	± 1
Lens 2 (negative)	± 0.1	± 0.03	± 1
CAL selector	± 0.1	N/A	± 1
Focal plane	± 0.1	± 2	

Table 50: Element position tolerances.

The two optical components are customized, positive power best form lens from CaF2 and a negative meniscus from fused silica. The tolerances used for the optical properties are listed in Table 51. The tolerances provided by the glass supplier were taken into account in total tolerance analysis.

Component	Diameter [mm]	Thickness [mm]	Index of refraction	Abbe number	Irregularity
Lens 1	+0.00/-0.10	±0.1	$\pm 5e^{-4}$	±8%	l/4
Lens 2	+0.00/-0.10	±0.1	$\pm 5e^{-4}$	±8%	l/4

Table 51: Optical tolerances for the components.

Table 53 shows the statistical data from 1225 Monte Carlo trials. The diffraction-limited RMS spot size is 0.00750 mm, which is realized in all of the cases. Compensator displacement is +2.09 /- 2.27 mm.

Diffraction-limit	0.00750 mm
Nominal	0.00181 mm
Best	0.00114 mm
Worst	0.00714 mm

Table 52: System performance.

98% >	0.00569
90% >	0.00449
80% >	0.00380
50% >	0.00282
20% >	0.00222
10% >	0.00196
2% >	0.00154

Table 53: Monte Carlo statistics.

9 Conclusions

In this document a description of the optical design of SOXS has been given.
Composed of five sub-systems (CP, UVVIS, NIR, AC and CU), SOXS will be a spectrograph of resolution of about 4000-5000 (for a 1 arcsec slit), covering the [350-2000]nm wavelength range 'in one shot' to be mounted at the Nasmyth focus of the New Technology Telescope. The description of the optical design and of the performances of the sub-systems has been reported, showing the feasibility of the instrument and the compliance with requirements.

<END OF DOCUMENT>